POLITECNICO DI MILANO
Corso di Laurea Magistrale in Ingegneria Aeronautica
Scuola di Ingegneria Industriale e dell'Informazione
Dipartimento di Scienze e Tecnologie Aerospaziali

Stall control by pulsed plasma actuators

Advisor: Prof. Marco Belan
Co-advisor: Ing. Federico Messanelli

Master Thesis of:
Francesco Bernardoni, ID 835898
Edoardo Frigerio, ID 836262

Academic year 2016-2017

Contents

List of Figures

List of Tables

Sommario

Lo scopo di questo lavoro di tesi è la caratterizzazione sperimentale di attuatori al plasma, di tipo corona e DBD (Dielectric Barrier Discharge), al fine di valutare le loro prestazioni nell'ambito del controllo della separazione su profili aerodinamici ad alto angolo di incidenza. In particolare, viene svolto uno studio parametrico per valutare l'efficacia dell'attuazione instazionaria su elettrodi attivi dotati di punte triangolari. Ciò non è reperibile nell'attuale letteratura. È stato inoltre misurato il consumo energetico. Tale ricerca è volta al fine di aumentare l'efficacia degli attuatori nella posticipazione dello stallo e nella riduzione della resistenza aerodinamica. Per far ciò, sono state effettuate prove di pesate aerodinamiche in galleria del vento su un profilo NACA0015 a due diversi numeri di Reynolds ($Re \approx 170000$ e $Re \approx 340000$). I risultati ottenuti indicano un incremento di prestazioni rispetto al caso di attuazione stazionaria, in particolare per numeri di Reynolds superiori ($Re \approx 340000$). Il dispendio energetico è inoltre ridotto con questo tipo di attuazione.

Parole chiave: Attuatori al plasma, Corona, DBD, Controllo attivo del flusso, Ritardo dello stallo, Elettrodi a punte.

Abstract

The aim of this thesis work is to experimentally characterize plasma actuators, both corona and DBD (Dielectric Barrier Discharge) types, in order to evaluate their performances as flow control devices on aerodynamic airfoils at high angles of attack. In particular, a parametric analysis on the effectiveness of unsteady actuation is performed on active electrodes with triangular tips. There is not a similar work in the present literature. Electrical characterization is carried out as well. This study is performed with the aim of improving actuator effectiveness, with particular focus on stall delay and drag reduction. To this purpose, lift and drag measurements have been performed on a NACA0015 airfoil in the wind tunnel for two different Reynolds numbers ($Re \approx 170000$ and $Re \approx 340000$). The results show an increased effectiveness with respect to steady actuation, especially for higher Reynolds number ($Re \approx 340000$). A lower energy consumption is found with this type of actuation.

Keywords: Plasma actuators, Corona, DBD, Active flow control, Stall delay, Serrated electrodes.

Ringraziamenti

I nostri ringraziamenti sono rivolti innanzitutto al nostro relatore, Prof. Marco Belan. La sua esperienza e la sua passione sono state fondamentali in questi mesi.
Ringraziamo anche l'Ing. Federico Messanelli per il suo prezioso aiuto e la sua disponibilità.
Un ringraziamento speciale va alle nostre famiglie che ci hanno sostenuto durante questi anni di studi universitari.
La nostra riconoscenza va ai nostri compagni di laboratorio Francesco, Sebastian, Marco e Lorenzo con cui abbiamo condiviso questa esperienza. Infine, ringraziamo l'Ing. Paolo Rubini e Roberto per la loro disponibilità.

Chapter 1

Introduction

The aim of the following thesis is to continue the experimental investigation on plasma actuators, to get a deep insight on this relatively new flow control strategy. These actuators, which fall into the category of "Electrohydrodynamic" devices, employ electrical fields and ionized molecules to manipulate the surrounding flow field. They represent a promising alternative to classic control devices employed in aeronautics, since they are simple to manufacture and lack moving mechanical parts which add weight and complexity to the structure. The short response time makes them suitable to control high speed and high frequency phenomena. The aim of this thesis work is to improve the actuator performances by investigating both geometrical shape and electrical parameters, mainly focusing on the effect of unsteady actuation.

In this first chapter a brief introduction to flow control is presented. The various techniques and the role of plasma actuators as flow control devices are introduced. In Chapter 2 the physics of plasma actuators is described. Both DBD and corona actuators are presented, along with their peculiarities and a short review on the state of art from literature, in particular focusing on their geometrical and electrical optimizations. In Chapter 3 the experimental setup adopted in our measurements is described. In Chapter 4 all results are reported and analyzed. In Chapter 5 conclusions of the research are presented and possible future developments and applications are suggested.

1.1 Flow control

The ability to manipulate a flow field to effect a desired change is of immense technological importance. This is why flow control has always been a major issue for fluid dynamicists. The benefits of developing efficient flow control systems range from saving billions of dollars in fuel cost for land, air, and sea vehicles, to realizing more efficient gas and oil distribution systems, as well as bio-medical devices and any other competitive industrial process involving fluid flows. Flow control is possible by acting on three main phenomena:

- Transition delay
- Separation prevention
- Turbulence control

1.1.1 Transition

Delaying or avoiding transition to turbulent boundary layer is very effective at reducing skin friction drag. Aeronautics in particular is the main field of interest for such technique: almost 50% of an aircraft's resistance is due to viscous forces. Furthermore, transition delay effectively reduces noise and improves passengers comfort.

It's easy to see why this issue is very important today since fuel efficiency and noise reduction play a major role in the aircraft business. Additionally, transition may be anticipated on purpose, in order to increase maximum lift coefficient and delay flow separation.

1.1.2 Separation

Boundary layer separation is a major issue that limits the design and performances of most devices involving fluid flow. Several efforts have been made to develop control techniques able to reduce or eliminate separation [1], [2], [3]. Briefly, separation control may be mainly achieved in four different ways:

- tangential blowing: low-momentum region at the wall is directly energized by means of different devices such as leading-edge slats, slotted flaps, and moving wall.
- wall suction: the low-momentum region of the flow is removed.
- vortex generators: the convective transport of freestream momentum to the wall is enhanced.
- forced excitation upstream of separation [4],[5], [6].

The first two approaches are extremely effective at eliminating the separation. The drawback is the necessity of realizing a complex system of internal pipes linked to a vacuum or pressure source or a mechanical system for slat actuation. On the other hand, vortex generators have been frequently applied due to their simplicity. However, like other passive devices, their effectiveness is limited by parasitic drag formation, which is always present even when the device is not necessary, i.e. at low angles of attack. The last approach consists of periodically exciting a leading-edge airfoil separation with a small vibrating flap. Phase-locked coherent vortex structures start forming over the downstream surface and a large increase in flow turning can be observed.

1.1.3 Turbulence control

It may be useful to increase or decrease turbulence level depending on the application. For instance, in combustion processes a high turbulence level is desirable to facilitate mixing. On the other hand, noise reduction requires low turbulence level.

1.1.4 Passive and active flow control

There are three main classification schemes for flow control methods [7]. The first one is to consider whether the technique is applied at the wall or away from it. Surface parameters that can influence the flow include roughness, shape, curvature, rigid-wall motion, compliance, temperature and porosity. For instance, heating and cooling the surface can modify fluid viscosity and density gradients. The injection of additives can significantly affect the boundary layer structure, modifying the velocity profile near the wall and influencing transition and separation. The second scheme considers energy expenditure and the control loop involved: a control device can be passive, requiring no auxiliary power, or active, requiring external energy. The third classification scheme considers whether the control technique directly modifies the shape of the instantaneous/mean velocity profile or selectively influences the small dissipative eddies. Here we adopted the second type of classification.

Passive control

Passive control is quite simple to implement, as it does not require energy to work, but it cannot sustain big changes in the working condition, especially in off-design conditions. It's even possible that the overall effect of the system is detrimental. Here is a list of the main passive flow control devices:

- Vortex generators: these devices are made to energize the lower region of the boundary layer by mixing it with the outer region. Usually they are small triangular shapes placed near the leading edge (see Fig. 1.1). Their height must be around 80% of the boundary layer thickness. The overall effect is a maximum lift increase, a stall delay and a drag increase. If the flow is attached, the only effect of the device is a drag increase.

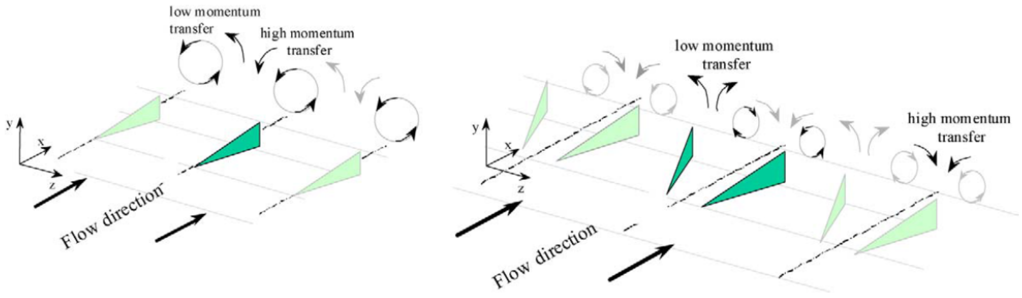

a) **b)**

Figure 1.1: Vortex generators working principle:(a) co-rotating configuration, (b) counter rotating configuration [8].

- Riblets: micro-grooves carved into the body surface that interact with and stabilize quasi-streamwise vortices. Generally aligned to the freestream direction, as shown in Fig. 1.2, their goal is to reduce viscous resistance. The common cross-sectional shapes are triangular, with sharp tips. However, they have been extensively studied [9],[10],[11], [12] and different geometries have been tried. Recently a streamwise sinusoidal shape has been proposed [13] leading to a 10% of drag reduction. Although their promising performances, riblets are very sensitive to external contamination (e.g. dust) and deformation. These factors can heavily alter the performances.

- Polymer injection: Reynolds stresses production in the buffer region can be suppressed by adding long-chain molecules or micro bubbles to liquid flows. These polymer chains are stretched by velocity fluctuations and provides a local increase of viscosity which consequently inhibits wall vortices production. Frictional drag reduction up to 80% was experimented [15].

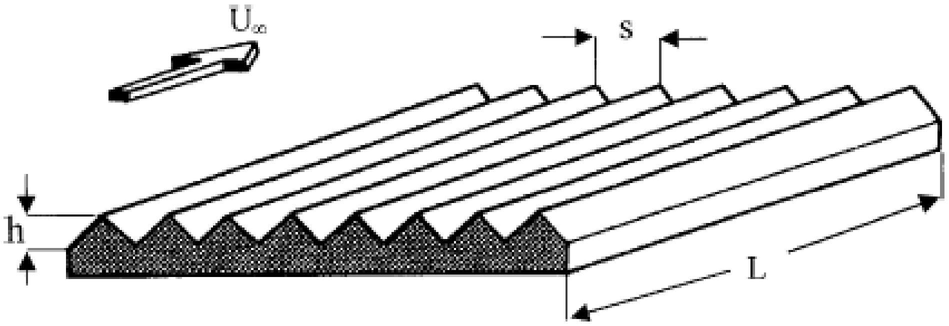

Figure 1.2: Riblets geometry [14].

- Compliant coatings form an adaptive surface that interacts with the wall structures. This can delay laminar-to-turbulent transition due to Tollmien-Schlichting instability [16].

Active control

Active control always requires actuators and can be divided into predetermined or reactive (see Fig. 1.3). In predetermined control the control loop is open and no sensors are required. A steady or unsteady energy input is applied without knowing the particular state of the flow. Reactive control consists of continuously adjusting the control input according to some measured variable. The control loop can either be an open (feedforward) or a closed (feedback) loop. In feedforward control, the measured variable differs from the controlled variable, while in feedback control the controlled variable must be measured, fed back and compared with a reference input. Reactive feedback control is further classified into four categories: adaptive, physical model-based, dynamical systems-based and optimal control [17]. Among the main active control techniques, we recall:

- Boundary layer blowing is a technique that increases energy and momentum of the boundary layer through injection of a streamwise high speed jet near the wall. This allows to increase maximum angle of attack before stall.
- Boundary layer suction achieves the same goal with the opposite principle of the previous technique. In this case the low speed region near the wall is drawn into slots or micro-porous wall.
- Spanwise wall oscillation is an effective method of drag reduction since the motion interacts with wall structures. Researchers showed that a sinusoidal waveform is very efficient, leading to a drag reduction of 34% [13].
- Travelling waves: in the same fashion as the spanwise oscillation, waves of spanwise velocity are modulated in the flow direction, as shown in Fig. 1.4. Numerical results in [13] showed a 48% drag reduction, partially confirmed by a 33% reduction during an experimental test performed in our laboratory.
- MEMS: Micro-Electro-Mechanical Systems are different types of miniaturized devices that can perform several functions with minimal disturbance to the flow field.

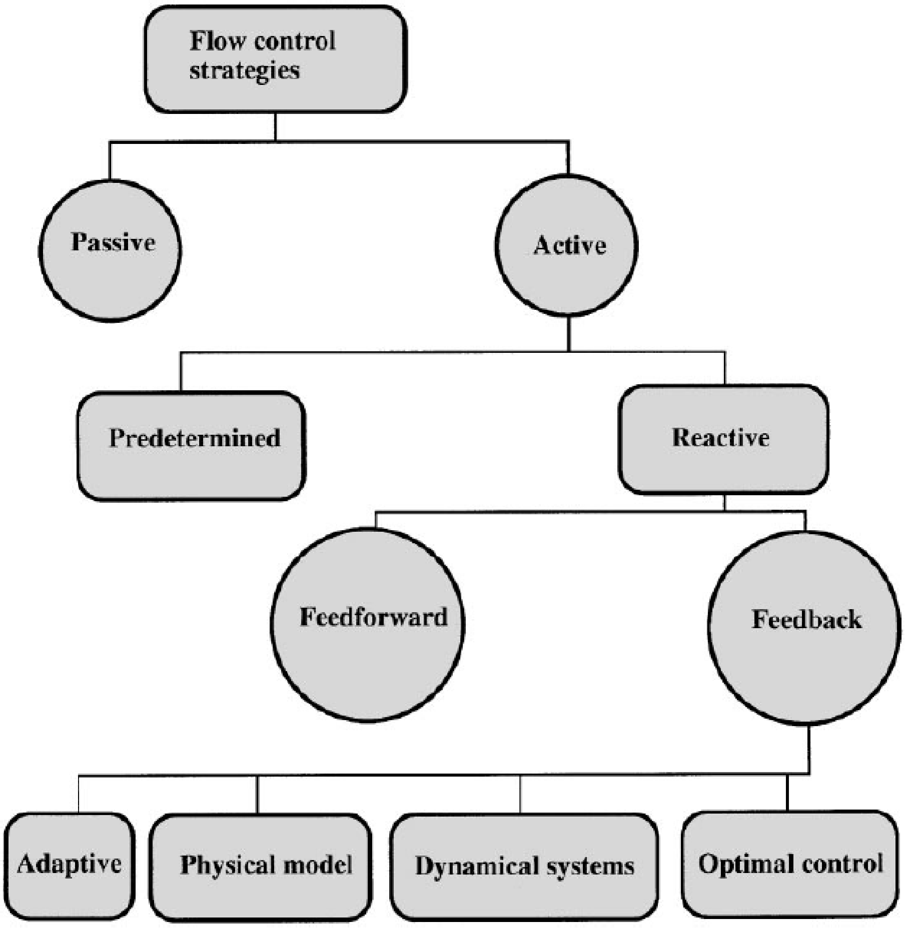

Figure 1.3: Flow control strategies [7].

Their small size, fast response, low unit-cost and energy consumption make them suitable for reactive control of turbulent flows where distributed arrays of sensing and actuation elements are required. Made of semi-conductors, they apply oscillatory motion promoting flow reattachment or delaying separation, for instance. By integrating electronics and mechanical components they are able to effectively manipulate coherent structures in a nonintrusive way. To achieve proper targeted control, temporal phasing as well as spatial selectivity are required. For example Fig. 1.5 shows a MEMS used in velocity profile measurements. In a turbulent flow, length and time scales are really small due to the high-Reynolds number. Therefore, a small sensor is required to effectively measure instantaneous quantities. Although hot wires are able in this sense, they are usually very fragile, expensive and handmade. On the other hand, MEMS can be easily employed in large numbers with a moderate cost and are not characterized by these drawbacks.

- EMHD (Electro-Magneto-Hydro-Dynamic): These devices consist of magnets and electrodes which control ionized flow through Lorentz force. The usual configuration

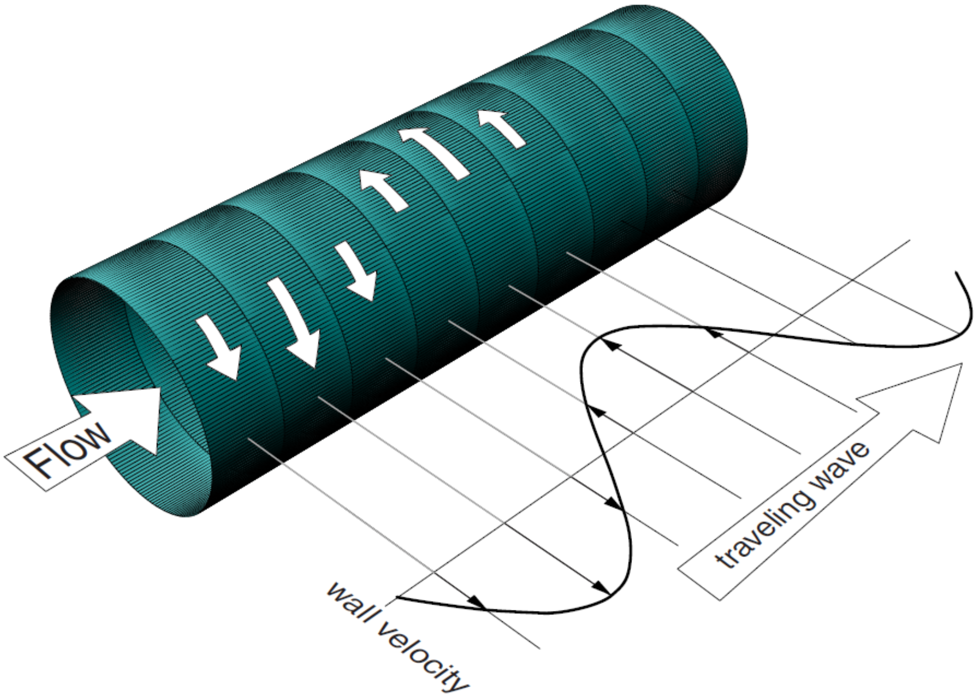

Figure 1.4: Traveling wave [13].

is the one shown in figure 1.6 . Different designs have been studied in [17].

1.1.5 Plasma actuators

Among the various active flow control techniques, in this thesis we focus on the EHD (electro-hydro-dynamic) flow control and in particular on plasma actuators. Those are simple devices which exploit plasma formation to impart the desired changes into a fluid flow, by manipulating the boundary layer. The first plasma actuators were called ”corona” actuators and have been studied extensively only from the 1990s. However, their tendency to generate sparks has pushed the researchers to find an alternative actuator. Roth’s group in the middle of the 1990s developed the DBD (Dielectric barrier discharge) actuator which is now the most common type of plasma device for flow control.

Both types of actuators generate ionic wind near the wall which can control flow separation, leading to lift augmentation, stall delay and drag reduction.

The main advantages of this technology are:

- The lack of mechanical moving parts which add weight and complexity to the structure.
- Simple manufacturing and small size ensure reliability and little flow disturbances.
- Short response time makes them suitable to control high speed and high frequency phenomena.

The main disadvantages of plasma actuators are:

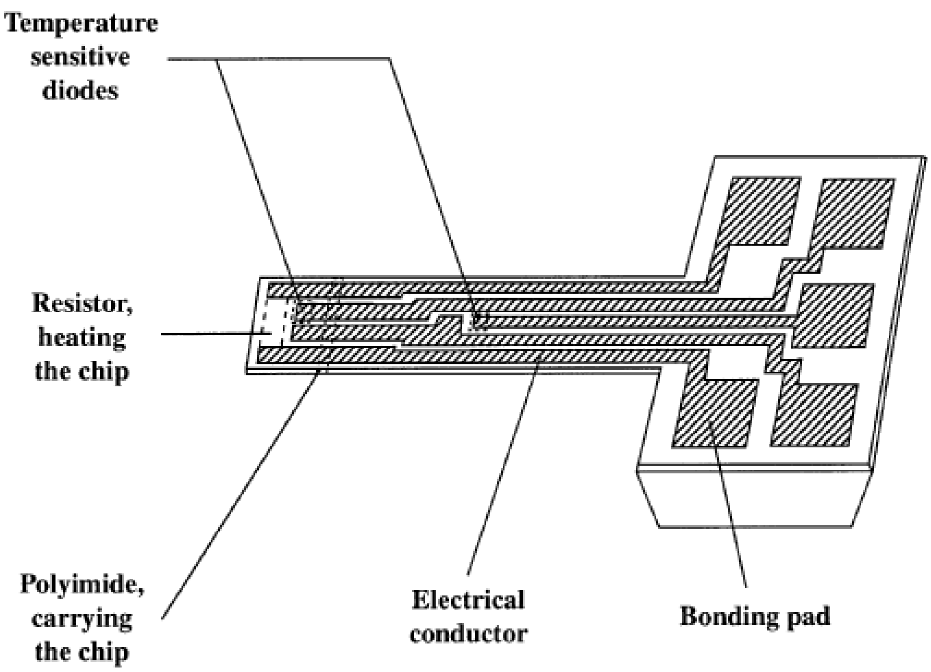

Figure 1.5: Single-wire MEMS sensor [7].

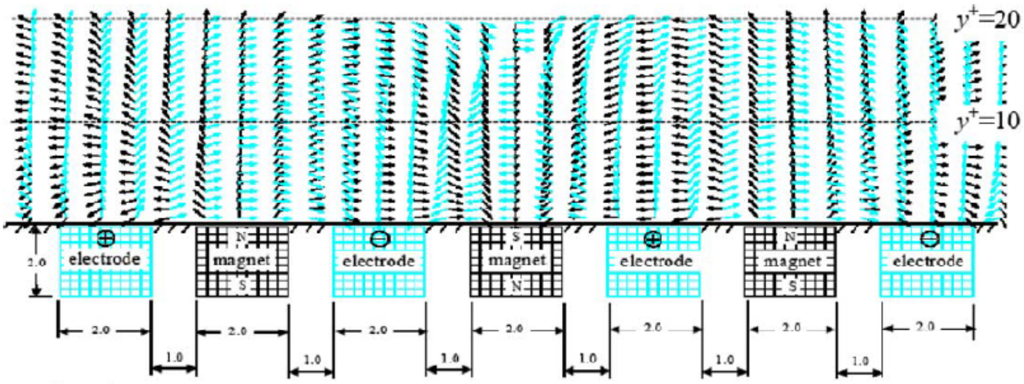

Figure 1.6: EMHD device [17].

- Energy conversion is not very efficient due to the intrinsic nature of the actuator. Moreover, low concentration of oxygen (high altitude) reduces the effectiveness of the device.

- Corona actuators are very sensitive to ambient humidity and their stability is strongly compromised by it.

- Above all, the main limitation of this type of actuators is that their performance decreases with high free stream velocity.

Plasma actuators find application in several fields. For instance, the group of Y. Sung in [18] investigated the alteration of the flow field in the wake of a cylinder by means of particle image velocimetry and smoke visualization. They demonstrated that vortex shedding as well as the wake size of bluff bodies are strongly reduced through proper plasma actuation.

The effect of plasma on bluff bodies is also studied for noise reduction. In particular, landing gear struts and wheel wells of civil aircrafts give a great contribution to noise, especially in landing phase when engines are almost idling. There are a few studies about this argument, where plasma actuators have proven effective for noise reduction ([18],[19]).

Plasma actuators are being tested also in the power production sector. Wind turbines can be equipped with DBD actuators to enhance aerodynamic properties. Both horizontal and vertical axis turbines have been tested (see [20] and [21]). Gas turbines efficiency can be improved with plasma actuators since they reduce the separated region between blades. Results of such an application are shown in [22].

Another application for plasma actuators is the flight control, particularly suitable for UAV since the effect of the actuation decreases with free stream speed. Longitudinal control without the use of hinged control surfaces was investigated by Patel et al [23]. The effectiveness of plasma-wing concept was demonstrated, in particular for aircraft with highly swept wings at high angles of attack where conventional flap and ailerons are ineffective (see [24]).

Several studies are found in literature regarding separation control by means of plasma actuation [25–30]. A plasma actuator was used to control leading-edge flow separation and dynamic stall vortex on a periodically oscillated NACA 0015 airfoil [26]. Jolibois et al. performed a test campaign in order to better understand where one has to act along the profile chord (as a function of the angle of attack) to be the most effective [27]. The experiments showed that the plasma actuator is more effective when it acts close to the natural separation location, and that the power consumption can be highly reduced in using a non-stationary actuation. Finally, plasma actuators are also employed in manipulating the laminar-to-turbulent transition of the boundary layer [31]. Grundmann and Tropea [16] cancelled artificially excited Tollmien–Schlichting waves using plasma actuators operated both in continuous and pulsed modes. A transition delay of approximately 20% for a free stream velocity of 10 m/s was found by Boucinha et al. [32]. Due to their unstable nature, corona actuators took second place with respect to DBD actuators. All recent studies are indeed focused on the latter type of plasma actuators, which are definitely more suitable for practical applications.

Chapter 2

Plasma actuators

Among all the active flow control methods, non-thermal surface plasmas are nowadays in full expansion [33]. This is due to the fact that they do not exhibit all the drawbacks of classic flow control devices. Indeed, mechanical devices, though effective, not only add weight, volume and are sources of noise and vibration but they may also break down due to the various mechanical parts involved. On the contrary, plasma actuators directly convert electric energy into kinetic energy without involving moving mechanical parts. Moreover, their short response time allows flow control at high frequency. However, this kind of energy conversion has a low efficiency.

In the past, nonthermal atmospheric pressure plasmas have been studied for several industrial applications such as ozone generation, pollutant removal and surface treatment. The discharge plasmas used for airflow control are usually atmospheric pressure corona discharges and most of all dielectric barrier discharges.

Plasma actuators actively control the airflow by inducing an electric field within the boundary layer. In its simplest form the actuator consists of two electrodes flush-mounted on the surface of the profile. When a high voltage is applied, electrons are formed by photo ionization and then accelerated towards the anode by the electric field. In their path they collide with neutral molecules and ionize the gas in an avalanche process. Equation 2 describes this phenomenon:

$$A + e^- \to A^+ + 2e^- \tag{2.1}$$

A thorough explanation may be found in [34],[35],[36],[37],[38]. Voltages range from a few kV to several tens of kV, with a frequency from 50 Hz to 50 kHz in the case of ac excitation. Electrical current ranges from a few μA to a few mA.

2.1 Corona actuators

Historically, dc coronas were the first actuators to be used to control the airflow by electrical discharges.

2.1.1 DC corona discharge

Corona discharge is formed where the electric field is sufficiently large. This usually takes place near sharp points or thin wires. Corona discharge may be considered as positive or negative depending on field and potential distribution. The electrical power of the continuous coronas is very low due to the formation of a corona-to-arc transition above a given threshold of voltage and current.

Positive corona

In the case of a positive corona, the strong electric field is located at the anode. Here the electrons are produced by photo ionization in the electrode gap and accelerated towards the anode. An ionization zone a few tenths of a millimeter is created around the point, where the number of positive ions and electrons is equal. Then ions are repulsed towards the cathode by Coulombian forces, and constitute the drift region since the electric field is not sufficiently large to allow recombination.

The discharge current of positive corona is characterized by two components: an alternative streamer current due to the streamer propagation, and a continuous unipolar current due to the ion drift that are collected by the grounded electrode. Streamers are plasma streaks through which the discharge is more likely to propagate. They have a frequency of about 10 kHz, a diameter of 100 μm and a displacement velocity ten times greater the typical electron drift velocity in an avalanche [39].

Negative corona

In the case of a negative corona, the high electric field is located at the cathode. Positive ions are created by detachment in the ionization zone and go rapidly towards the cathode, while negative ions created by attachment drift towards the grounded plane electrode.

2.1.2 Electric wind

Electric wind, first investigated by Hauksbee and then by Faraday, ”refers to the movement of gas induced by the repulsion of ions from the vicinity of a high voltage electrode” [40].

The first expression of the electric wind velocity was given in 1961 by Robinson [40]:

$$v_G = k\sqrt{\frac{i}{\rho\mu}} \tag{2.2}$$

where k is a constant that depends on the electrode geometry, i the time-averaged discharge current, ρ the gas density and μ the ion mobility.

In 1993, the expression of Robinson was completed by Sigmond and Lagstadt [41]:

$$v_G = \sqrt{\frac{id}{\rho\mu A_G}} \tag{2.3}$$

where d is the electrode gap and A_G the discharge cross-section.

Actually, what really induces the electric wind is still a matter of discussion among plasma researchers. Indeed, it is not completely clear if it is only due to ion drift or to the streamer propagation. However, recent discovers pointed out that electric wind is generated by both phenomena.

2.1.3 Electrical properties

Fig. 2.1 shows the most common geometrical configurations used for dc plasma actuators.

Among them the surface wire to wire is the easiest to analyze. Two wire electrodes are placed inside a groove at the wall surface. To intensify the electric field at the anode, the cathode diameter should be greater than the anode one.

When a high voltage is applied to the actuator the discharge is established.

A substantial difference can be observed between the surface corona and the volume corona. Indeed, above 7kV/cm, the former manifest a sudden increase in current due to the gas–solid interface. In particular, in the case of surface coronas, five corona discharge regimes may be observed when the voltage between both electrodes is increased, according to the classification proposed by Moreau ([33]):

- Spot regime: just above the corona starting voltage, the discharge is concentrated within some visible spots on the smaller diameter wire. Electric wind is negligible and current density is smaller than 0.2mA /m.

- Streamer discharge: if the electric field is increased, a thin sheet of blue ionized air starts to form between the electrodes. Current density values vary from 0.2 to 0.5 mA/m.

- Glow discharge: as voltage or gap ratios are increased, the thin sheet is replaced by two luminous regions near the electrodes, while the gap is dark (see Fig. 2.3). This regime allows to reach higher currents and is more stable compared to the streamer discharge.

- Filamentary regime: as the voltage or gap ratio are further increased, current starts to concentrate within a few filaments.

- Spark regime: beyond the filamentary regime, sparks appear and the discharge process becomes difficult to control. Furthermore, the high current during spark formation heats the electrodes and may damage them.

The current-voltage behaviour of corona actuators in different regimes is shown in Fig. 2.4.

2.1.4 Influence of external parameters

Corona actuators are very sensitive to atmospheric as well as to geometric parameters. In particular, the discharge presents fewer glow-to-arc transition if the anode diameter is chosen much smaller than the cathode one. Secondly, temperature effects are negligible up to 60°C, while pressure and relative humidity strongly influence the discharge process. Indeed, high values of humidity have a destabilizing effect for the discharge. The effect of air humidity is shown in Fig. 2.6. The discharge electrical properties are also highly dependent on the dielectric wall surface. The presence of a free air stream strongly affects the discharge process and limits the glow-to-arc transition (see Fig. 2.5). The free air stream also influences the current behavior, when voltage is kept constant. A thorough investigation on these topics has been conducted by [43].

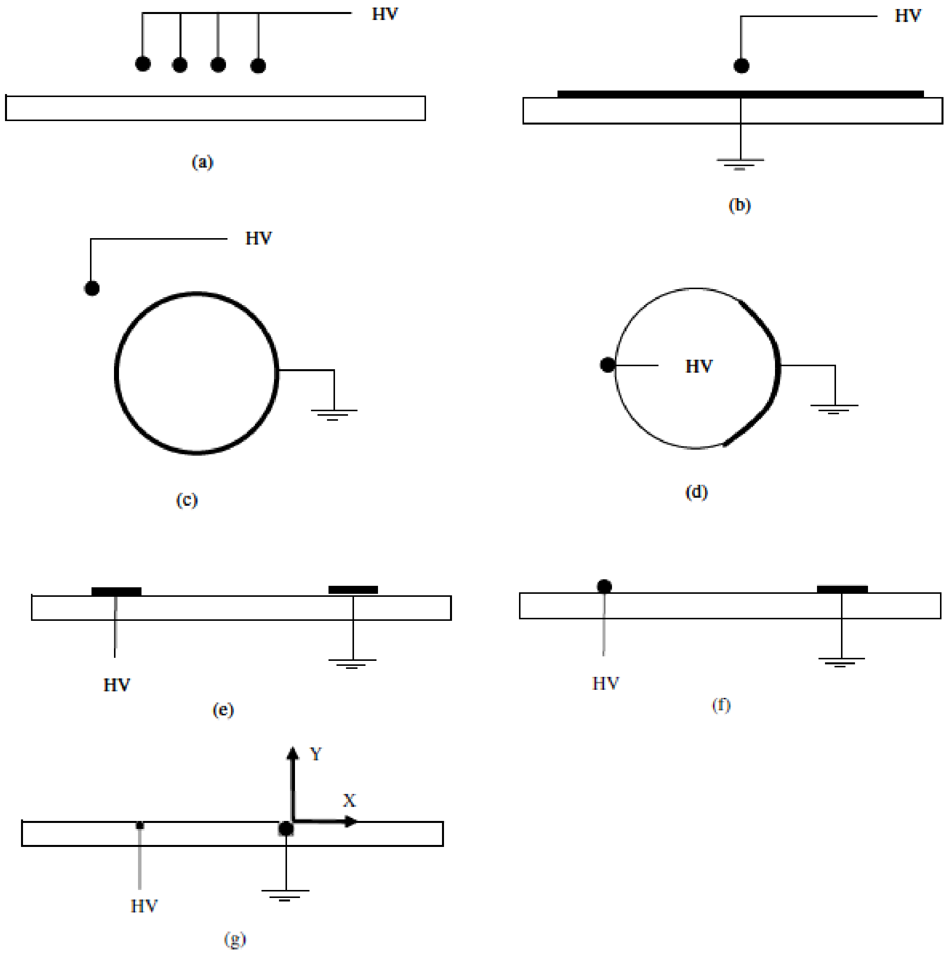

Figure 2.1: Geometrical configurations of DC plasma actuators: (a) volume multiple wire, (b) volume wire-to-plate in plane configuration, (c) volume wire-to-plate in cylindrical configuration, (d) surface wire-to-plate or point-to-plate in cylindrical configuration, (e) surface plate-to-plate, (f) surface wire-to-plate, (g) surface wire-to-wire [33].

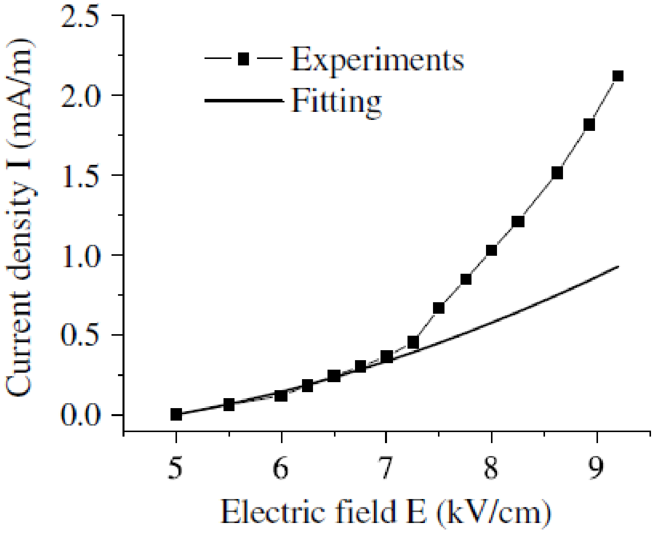

Figure 2.2: Current density I versus reduced electric field E [33].

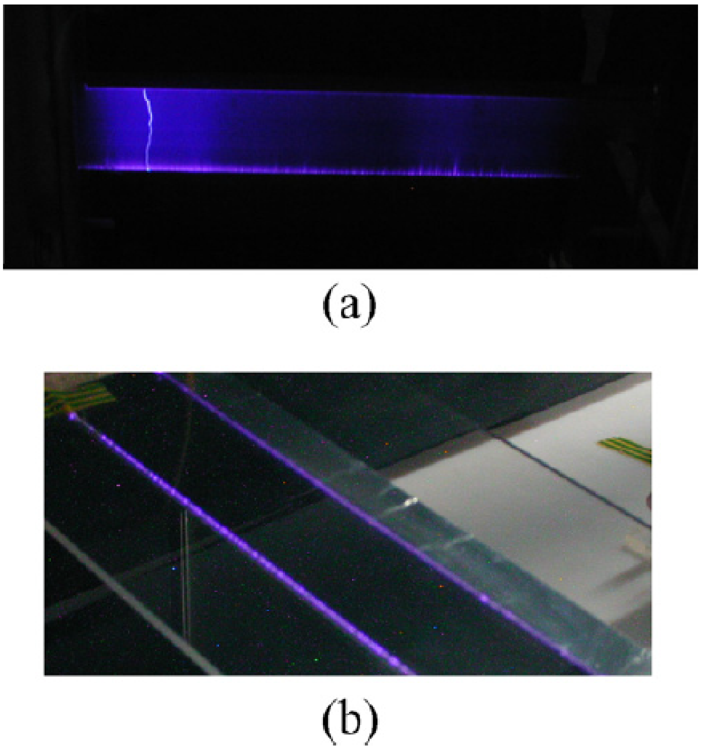

Figure 2.3: Behaviour of corona actuators in glow (a) and streamer regime (b) [42].

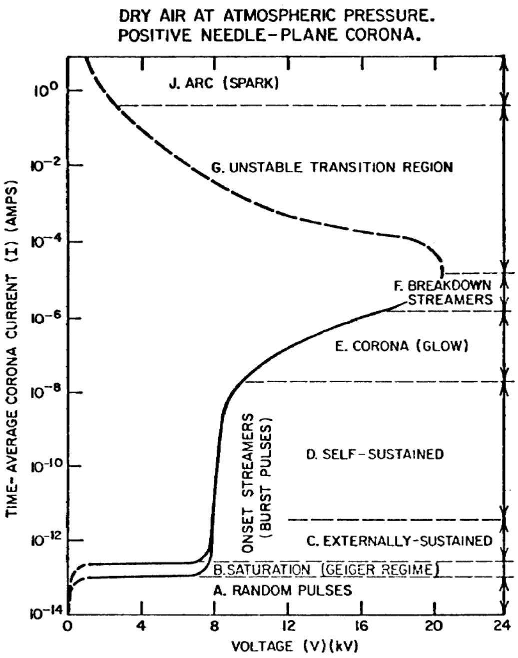

Figure 2.4: Current and voltage behaviour in different regimes [42].

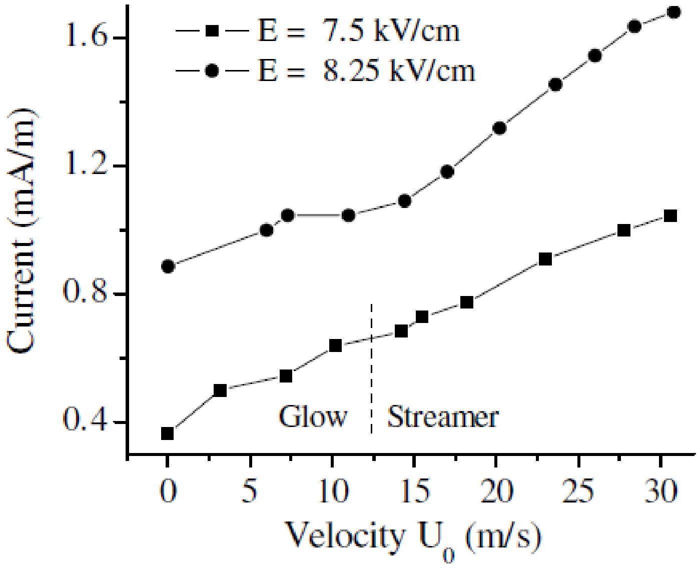

Figure 2.5: Effect of air stream velocity [33].

2.1.5 Induced electric wind

In several works the electric wind velocity profiles have been studied. The velocity profile is directly measured from the dynamic pressure. A standard Pitot probe measures

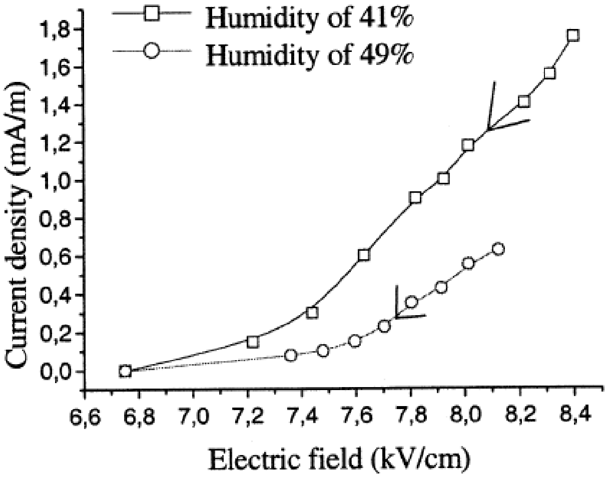

Figure 2.6: Influence of air humidity [44].

the static pressure, while a glass capillary connected to a micro-manometer measures the total pressure from the profile wall (y = 0) to y = 20 mm.

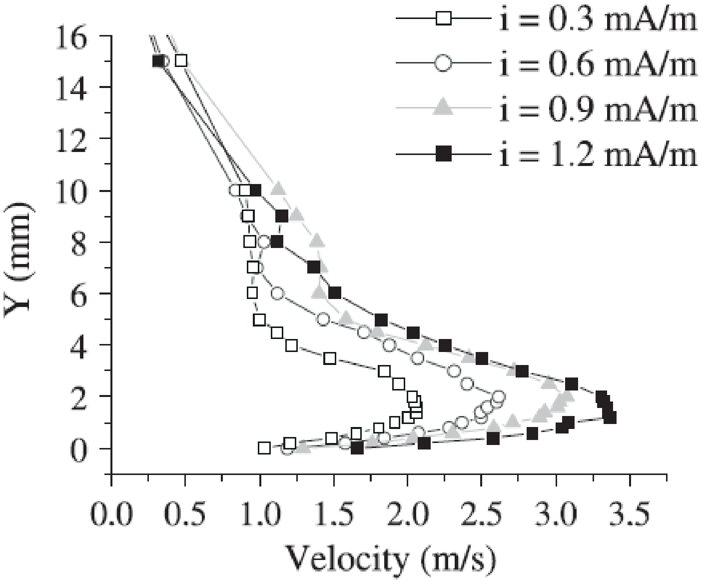

Figure 2.7: Velocity profiles versus time-averaged current values [33].

As Fig. 2.7 shows, the electric wind velocity increases with the current and the maximum velocity is usually obtained at a distance of about 1 mm from the wall (y = 1 mm). Moreover, the maximum velocity ever measured to date was about 5 m/s. Its behaviour with the discharge current is shown in Fig. 2.8.

Once the velocity profile is known, the electro-mechanical efficiency of the plasma actuator (in the absence of a free air stream) can be calculated as:

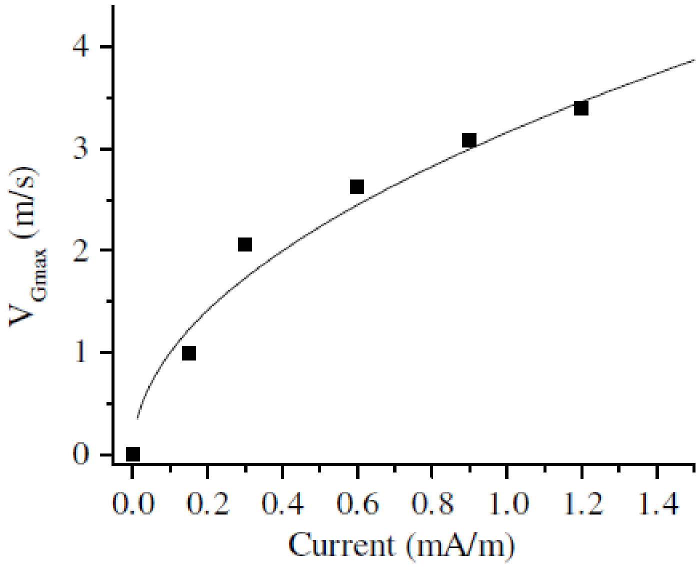

Figure 2.8: Maximum velocity versus time-averaged discharge current [33].

$$\eta = \frac{P_{mec}}{P_{elec}} \tag{2.4}$$

Albeit the instability of the discharge is surely the main drawback of corona actuators, their efficiency is in the order of a few tenths of a percent and decreases nearly linearly with current, as shown in Fig. 2.9. One of the reasons for this behaviour is that skin-friction at the wall reduces significantly the electric wind velocity.

2.2 DBD actuators

In the middle of the 1990s, Roth's group perfected and developed a new atmospheric surface pressure DBD. Actually they called it 'One Atmosphere Uniform Glow Discharge Plasma' (OAUGDP). Fig. 2.10 shows the three basic configurations tested by Roth et al [45],[46]. Nowadays DBD actuators are widely studied, while Corona actuators play a minor role. This is due to the fact that DBD actuators are more stable and do not exhibit the glow-to-arc transitions, thanks to the self-limiting effect of the dielectric material between the two electrodes. The configuration of DBD plasma actuators consists of two electrodes: one is exposed to the air, while the other is covered by dielectric material in order to stabilize the discharge. Typically, the air exposed electrode is fed with the high voltage, while the lower one is grounded. When an AC voltage is applied between the electrodes, the air over the encapsulated electrode is weakly ionized and accelerated away from the actuator, thus creating the so called ionic wind (see Fig. 2.11).

Plasma is produced only when the voltage applied to the electrodes is high enough to generate an electric field greater than the breakdown electric field. Above this breakdown threshold it is possible to sustain electric ion pairs in the gas. Once the actuator has been activated, it is possible to lower the AC voltage to below the threshold value without turning the actuator off.

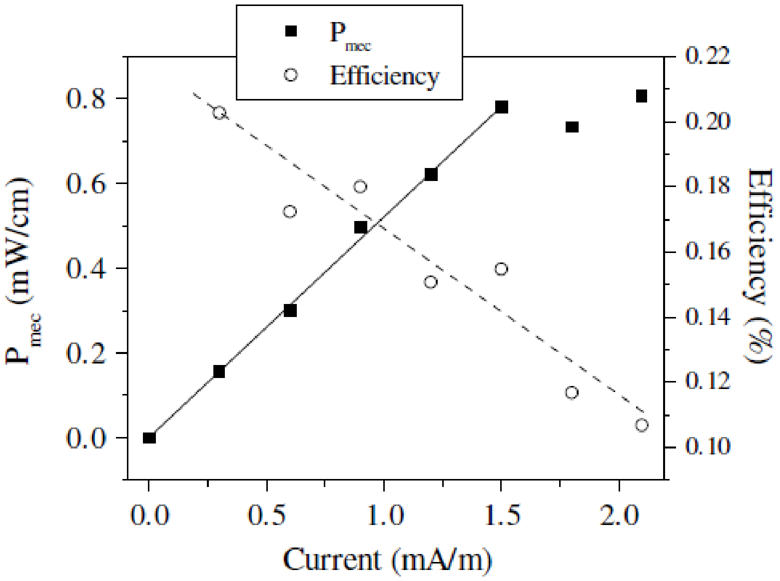

Figure 2.9: Discharge-induced kinetic power and electro-mechanical efficiency versus time-averaged current [33].

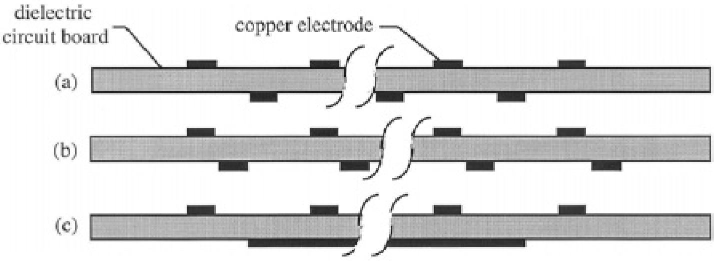

Figure 2.10: Plasma panel design concepts. (a) Symmetric staggered, (b) asymmetric staggered, (c) symmetric planar lower electrodes [45].

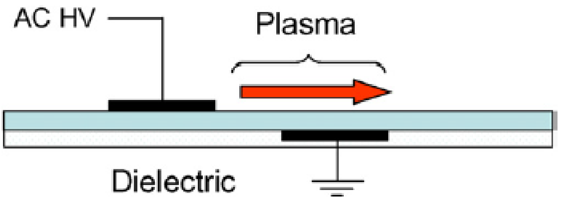

Figure 2.11: Working principle of a DBD actuator with encapsulated grounded electrode [33].

The breakdown electric field is influenced by the driving frequency. The optimum value of AC frequency depends on several factors:

- Static pressure
- Type of gas in which the actuator is working
- Dielectric material and thickness
- Frequency response of the power source
- Actuator geometry (electrode gap and shape)

These aspects will be discussed in sections 2.2.4, 2.2.5.

2.2.1 DBD operation with sinusoidal voltage

DBD actuators are commonly operated by using a sinusoidal input voltage in the order of tens of kV. The discharge current is in the form of a sinusoidal wave superimposed with fast microdischarges called streamers. Voltage and current are out of phase due to the capacitive nature of the actuator, which is mainly caused by the dielectric between the electrodes and the air gap. If plasma formed on both sides of the dielectric, current would have almost the same behaviour in the two half-cycles. In fact, Fig. 2.12 shows a symmetric current waveform, generated by a surface DBD without ground-electrode encapsulation.

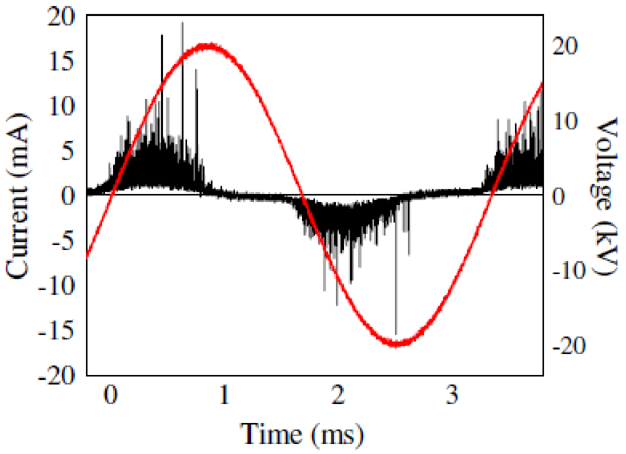

Figure 2.12: Voltage and current versus time plot of a surface DBD [33].

However, typically the lower electrode is encapsulated with a dielectric material, since plasma formation on the lower side of the surface is undesired and only causes a higher power consumption; consequently, plasma forms only on the upper side thus the current waveform is different in the negative and positive half-cycles (see Fig. 2.13). During the positive half cycle, the DBD works in the streamer regime, which is characterized by fast microdischarges. By contrast, during the negative half cycle, which is known as glow regime, plasma emission is more homogeneous. As a result, ionic wind generation is much more effective during the negative half-cycle (glow regime), see Fig. 2.14.

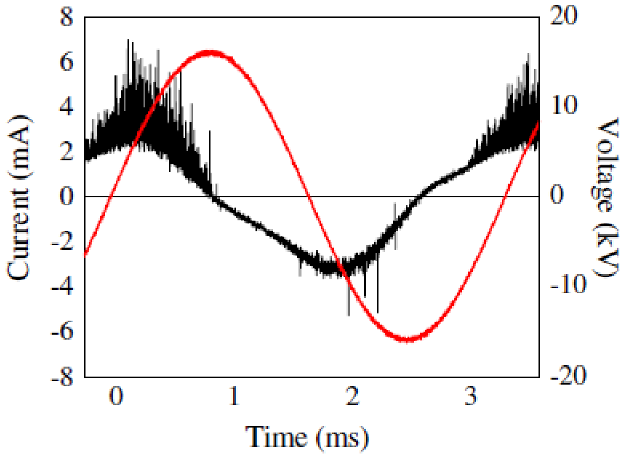

Figure 2.13: Voltage and current versus time plot of a DBD actuator with grounded electrode encapsulated [33].

The explanation of this phenomenon is associated with the source of the electrons. During the negative half-cycle electrons are released quite uniformly by the exposed electrode, and travel towards the dielectric material. During the positive half-cycle, on the other hand, the electrons are attracted from the dielectric material by the positive exposed electrode, which releases them discontinuously in the form of large microdischarges. Enloe et al in [48] as well as Benard et al in [49] confirmed this behaviour by performing an optical measurement (see Fig. 2.15). An increase in the voltage or frequency of the input waveform leads to higher body force. However, beyond a certain voltage, strong microdischarges start to form without any increase in body force and consequently in ionic wind. This is known as filamentary regime, which is better to avoid since it causes the actuator to become saturated and dangerously overheated without bringing any advantage.

2.2.2 Electrical power consumption

Regarding electrical power consumption several studies have been made. Generally power increases with voltage according to a power law (see Fig. 2.16):

Different values of the exponent have been proposed in literature, but the most common is 7/2 (see Eq. 2.5 and [50] for details). Moreover, the dependency of power consumption on the dielectric thickness is not negligible (see [51]). In particular, power decreases with dielectric thickness for the same input voltage (see Fig. 2.17).

$$P \propto V^{\frac{7}{2}} \tag{2.5}$$

Power also depends linearly on input voltage frequency, as shown in Fig. 2.16 (for further details see [51]).

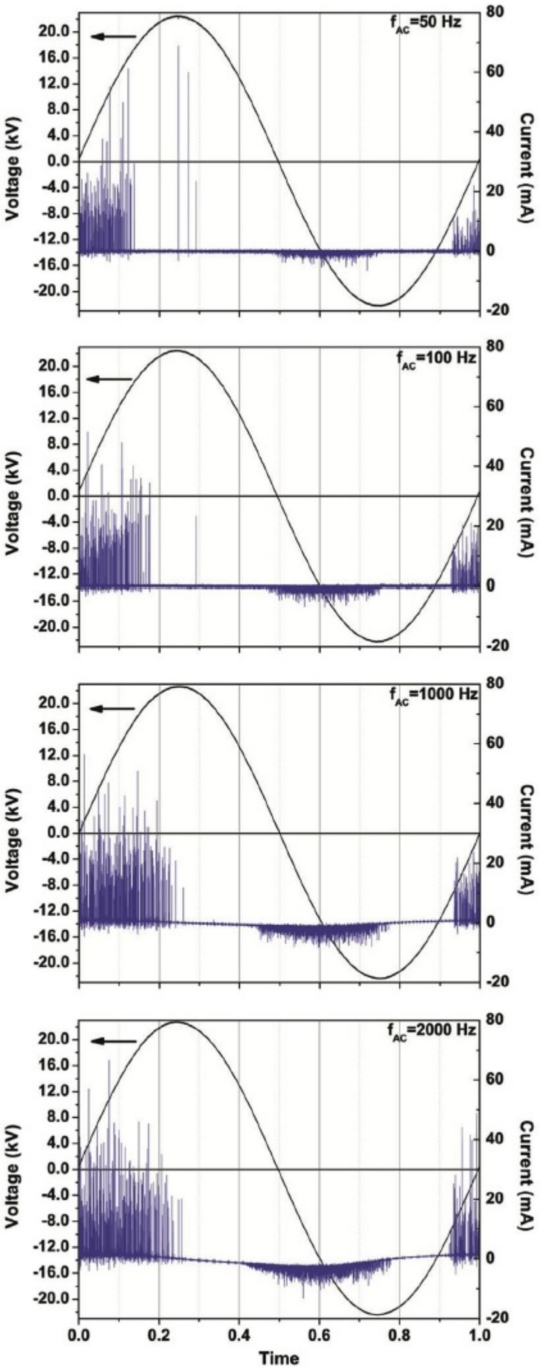

Figure 2.14: Time evolution of the current for four different frequencies [47].

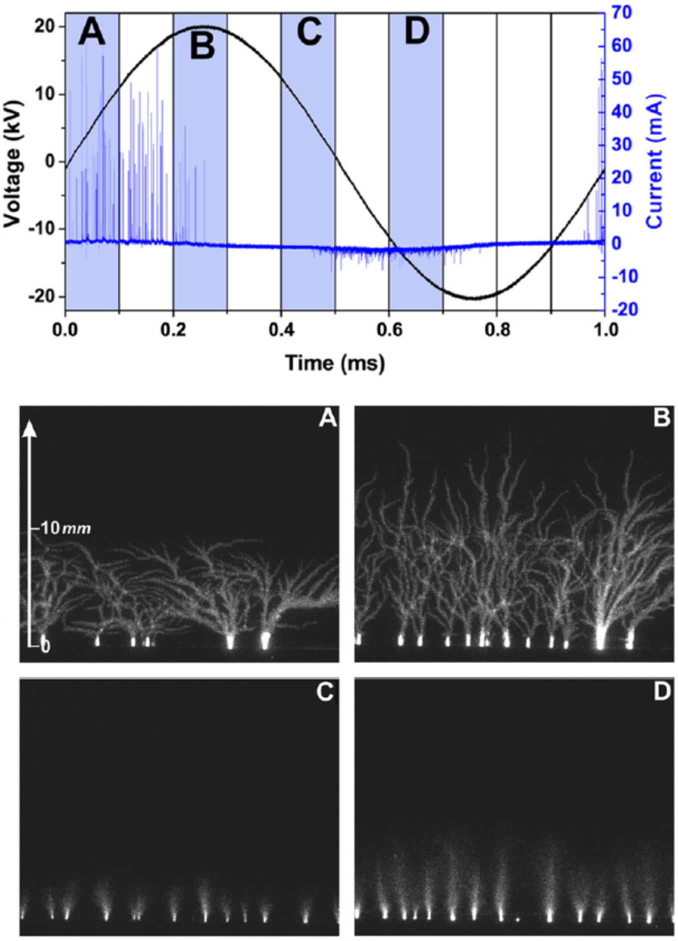

Figure 2.15: Plasma morphology in four phases of discharge [49].

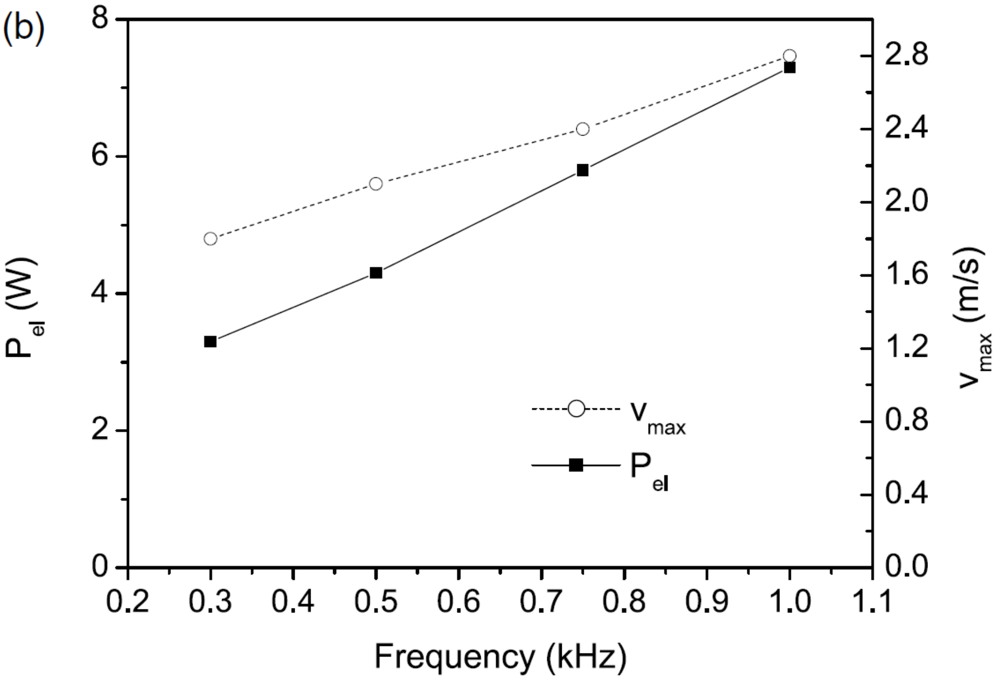

Figure 2.16: Electrical power consumption versus frequency of input voltage. [51].

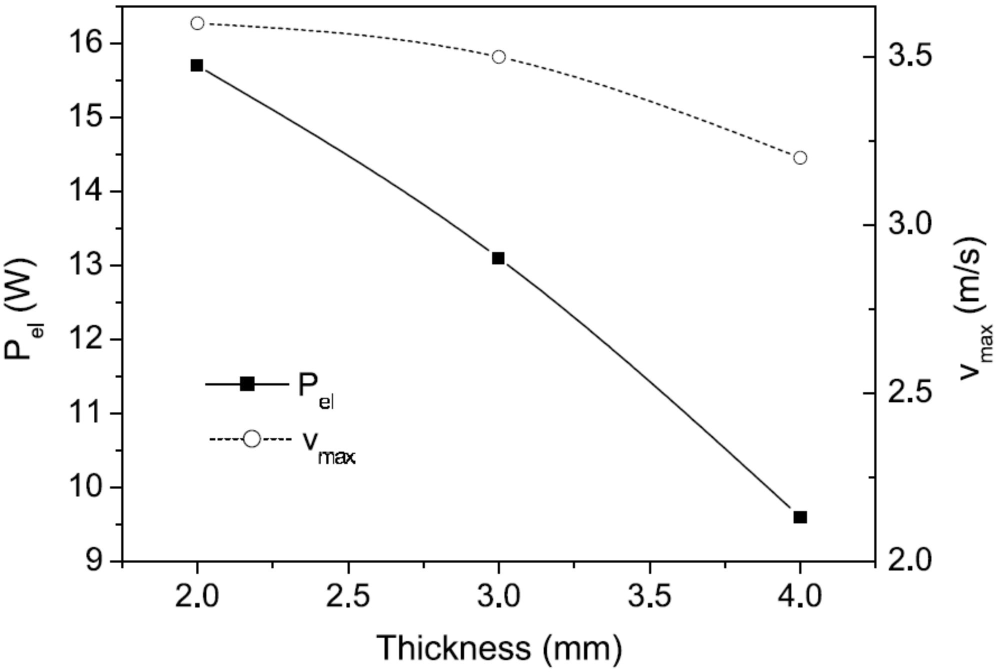

Figure 2.17: Electrical power consumption for different dielectric thicknesses [51].

2.2.3 Electrical wind

Several studies have been conducted regarding the DBD-induced velocity (see [51], [52],[53]). For instance, Pons et al [51] measured velocity profiles in the absence of a free air stream, investigating the effect of several parameters such as the applied voltage, frequency, electrode gap, dielectric thickness and dielectric nature. The key results were as follows:

- the velocity induced by the grounded (not encapsulated) electrode is slightly smaller than the velocity induced by the high voltage electrode.
- the momentum comes from the region above the air exposed electrode. As for the surface corona, the discharge induces a depression towards the wall.
- the maximum velocity is always reached at the limit of the plasma extension.
- The maximum speed is located at about 0.5mm from the wall.(see Fig. 2.18 2.19). The average velocity exhibits a power law behavior with respect to the applied voltage, with the exponent depending on the dielectric thickness.

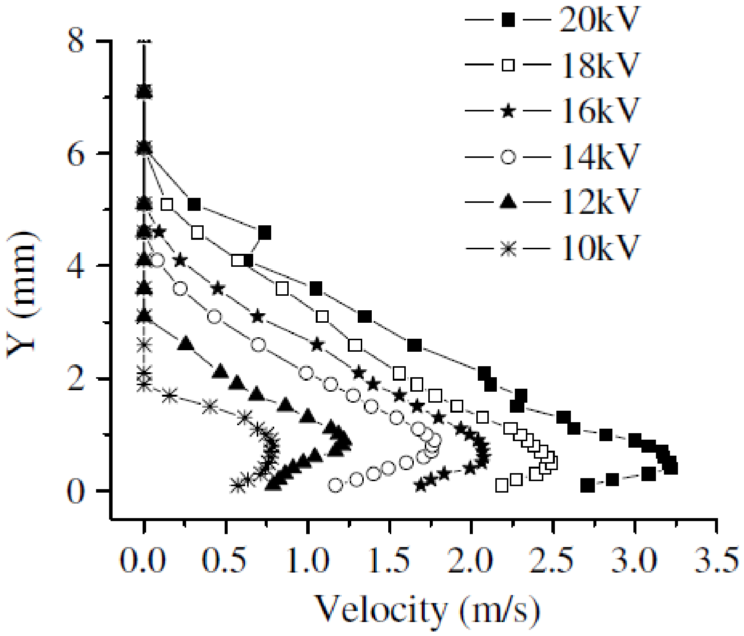

Figure 2.18: Velocity profiles for different voltages [33].

2.2.4 Geometrical optimization of DBD actuators

Geometrical shape plays a major role in the performance of DBD actuators. The main parameters involved are:

- Dielectric material and thickness
- Electrode gap

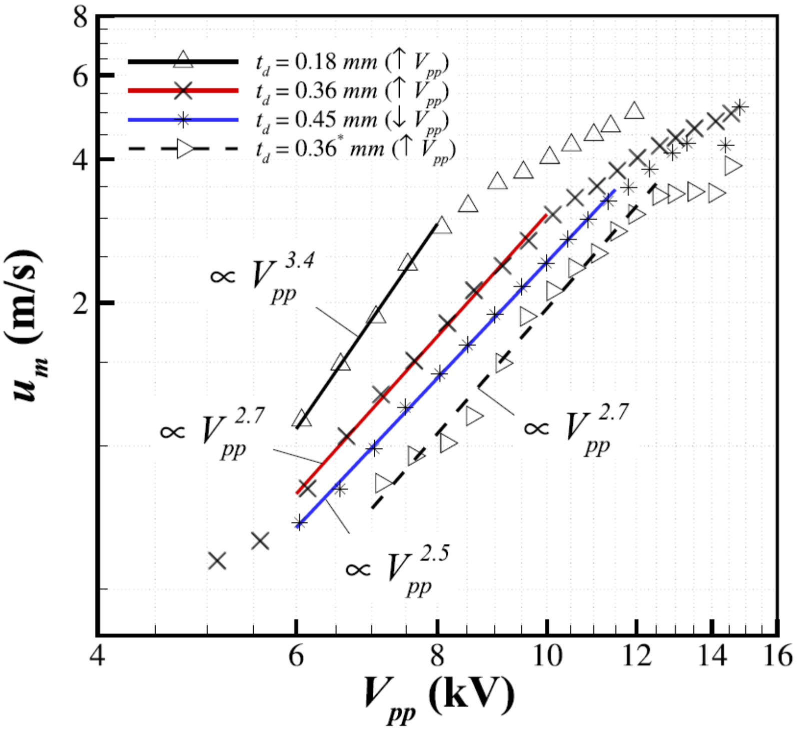

Figure 2.19: Average velocity for different voltages and dielectric thicknesses [54].

- Exposed electrode geometry
- Encapsulated electrode geometry
- Number of actuators

Dielectric material and thickness

Several studies showed that the most suitable dielectric material should have low dielectric coefficient and high breakdown voltage per unit thickness. Indeed, in order to avoid saturation, the capacitance of the actuator must be as low as possible. Since the capacitance of a DBD is proportional to $\frac{\epsilon}{thickness}$, it is advisable to increase the thickness of the dielectric material, while a lower dielectric constant allows higher voltages to be applied before the onset of streamer formation. Furthermore, being power dissipation proportional to the actuator capacitance, a lower capacitance will also reduce heat production. Fig. 2.20 shows the trend of thrust with different dielectric materials [55].

Although a thin dielectric material generates higher body forces (for the same input voltage), saturation occurs at lower voltage. Given that DBD actuators perform better at high voltages, a thick dielectric is preferable. In addition to a high dielectric strength, dielectric materials must not chemically degrade in the presence of plasma. The most common dielectric materials are Kapton, Teflon, Delrin, Macor, PMMA and other polymers with similar characteristics. Fig. 2.21 shows the thrust in saturation conditions for different dielectric materials [55].

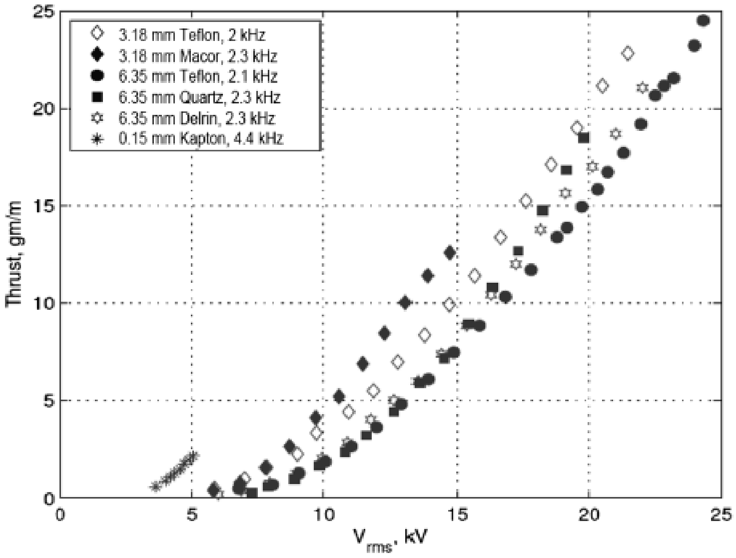

Figure 2.20: Thrust vs voltage for different dielectric materials [55].

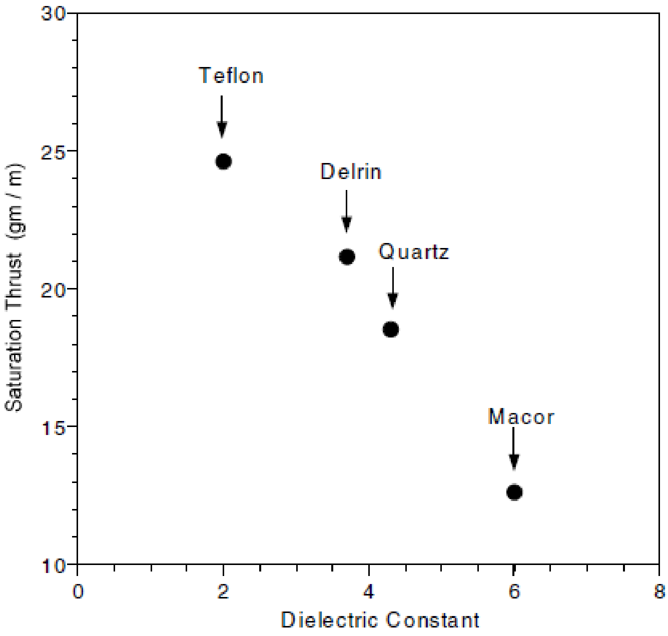

Figure 2.21: Saturation thrust vs dielectric constant [55].

Electrode gap

A long electrode gap reduces the intensity of the electric field but allows the ionized molecules to transfer more momentum to the surrounding air. It follows that higher voltage is required to produce the same effect as the one which would result from a smaller gap. On the other hand, completely overlapping the electrodes produces a symmetric distribution of the electric field and no net flow. Fig. 2.22 shows the trend of maximum induced velocity with different electrode gaps.

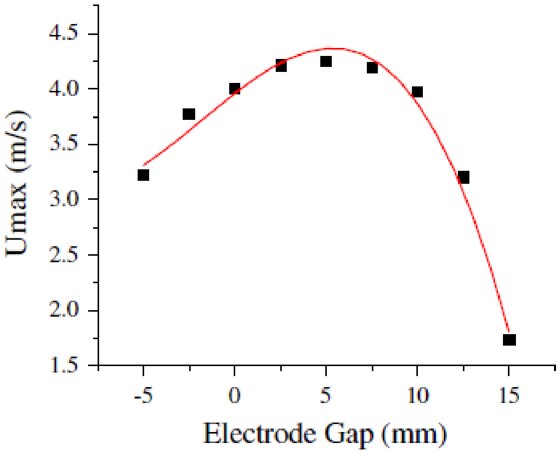

Figure 2.22: Maximum induced velocity as a function of electrode gap [33].

Encapsulated electrode geometry

As for the geometry of the encapsulated electrode, the key parameter is its width, which may limit the maximum induced velocity (see Fig. 2.23). The larger the electrode, the farther the plasma can expand, provided that the voltage is sufficiently high, until it reaches a plateau when dissipative phenomena become predominant.

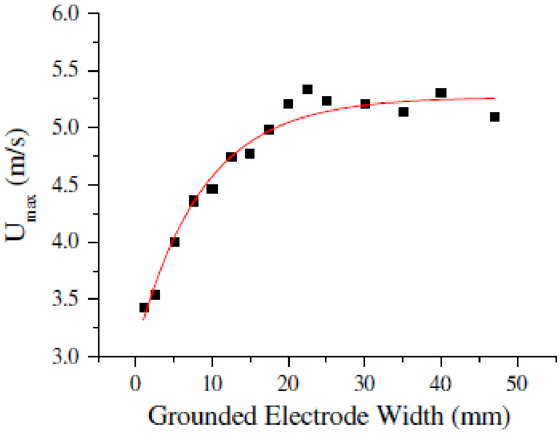

Figure 2.23: Maximum induced velocity as a function of encapsulated electrode width [33].

Exposed electrode geometry

The influence of the exposed electrode geometry has been studied intensively in literature. For instance, Joussot et al. [56] investigated the serrated electrode geometry and compared it with a traditional linear DBD. With the serrated configuration, ICCD images of the discharge showed that streamers are bent, whereas with the linear configuration they are straight. These curved streamers induce a three-dimensional flow topology. Whereas a two-dimensional wall-jet is induced with the linear configuration, a transverse velocity component is measured with the serrated configuration, implying the creation of spanwise-periodic vorticity. Furthermore, the streamers generated with the serrated design are longer than those created with the linear design for the same applied high voltage. This is due to the local increase in the electric field at each tip. Fig. 2.24 and 2.25 illustrate the discharge process of the serrated design. An increase in body force for the serrated electrode geometry was found by Thomas [55]. Also, Belan et al. in [57] and Modugno et al. [58] investigated the serrated geometry for DBDs and corona actuators observing an increase in ionic wind with respect to linear actuators.

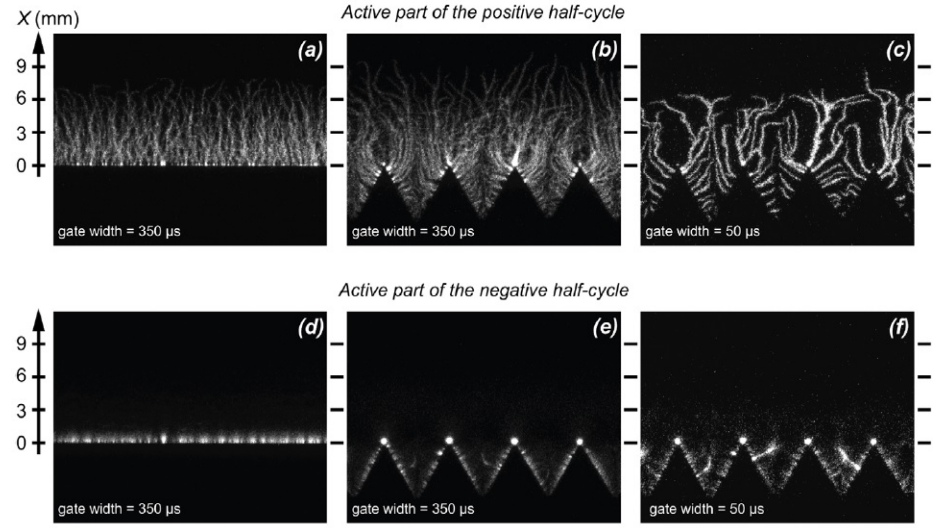

Figure 2.24: Plasma imaging during the active part of: the positive half-cycle for (a) linear and (b), (c) serrated designs, the negative half-cycle for (d) linear and (e), (f) serrated designs ($V = 10kV$ and $f = 1kHz$) [56].

The general case of serrated electrodes is the serpentine design [59],[60],[61], consisting of a DBD actuator with electrodes shape which can be described by a continuous parametric function that is periodic is some direction. Any serpentine geometries can be characterized as having a wavelength (λ) and an amplitude (A). This class of plasma actuators shows high versatility and can be useful under a wide variety of flow conditions [60]. Such a device has numerous aerodynamic applications where an increased mixing of the local fluid is desired, due to the tridimensional nature of the body force, which, in turn, implies the generation of vortices [59].

For flow separation control, the usual configuration is to orient DBD actuators along the spanwise direction so that a body force is produced in the direction of the mean flow. This directly adds momentum into the boundary layer which may re-energize the fluid. On the other hand, passive vortex generators can prevent flow separation by enhancing

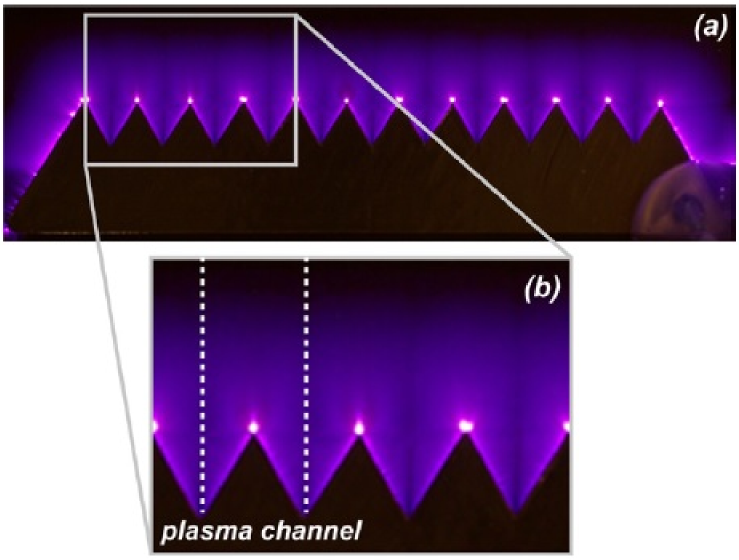

Figure 2.25: Image of the plasma for the serrated design (a) and schematic of a plasma channel (b) (exposure time of 20 s, $V = 10kV$, $f = 1kHz$) [56].

the mixing between the boundary layer and the free stream, so that high-momentum fluid is brought from the outer flow into the near-wall region. This re-energizes the near-wall fluid, allowing it to withstand more severe adverse pressure gradients before separation.

DBD actuators can be employed as alternative vortex generators [62],[63],[64],[30]. However, these devices theoretically do not induce additional drag since they are flush mounted and can be rapidly switched on and off as required. Being yawed with respect to the primary flow direction, they produce a body force with component into the spanwise direction that can generate longitudinal vortices. Jukes and Choi [65] investigated a single DBD vortex generator in a laminar boundary layer. They studied the development of the streamwise vortex using cross-stream PIV. Actuators placed at 90° to the oncoming flow produced the strongest vortex. Schatzman and Thomas [30] observed that DBD vortex generators could be just as effective as co-flow actuators in a similar configuration. Grundmann, Sayles and Eaton [66] and Grundmann et al. [67] found a significant improvement with DBD vortex generators for controlling the separation bubble in a three-dimensional diffuser.

2.2.5 Electrical optimization

The three fundamental parameters governing the electrical behaviour of plasma actuators are frequency, voltage and waveform.

Frequency optimization

The response of actuators to the frequency of the input voltage depends on its level of saturation. If the actuator is beyond saturation, an increase in frequency results in no beneficial effect since body force is not increased, while filamentary streamers increase in intensity. On the other hand, when the actuator works below saturation, an increase in frequency leads to a stronger ionic wind (see Fig. 2.27). Therefore, the filaments formation represent an upper limit for the thrust produced by the actuator. Once the filaments begin to form, an increase in voltage and/or frequency amplitude leads only to additional power dissipation without influencing saturation thrust. The effect of frequency on streamers is shown in Fig. 2.26. Eventually a further voltage/frequency increase leads to dielectric breakdown. Moreover, since saturation voltage decreases with increasing frequency, an optimization process is required.

Voltage optimization

DBD actuators respond to voltage and frequency in a similar way. In particular, since the exponent of the power-law for body force and ionic wind with voltage is higher than that of frequency, one would rather increase voltage for better performances. Saturation limits the maximum ionic wind after a certain voltage value. After saturation, the discharge process becomes filamentary and unstable.

Waveform optimization

Since ionization occurs when the difference between the instantaneous AC voltage and the charge build up on the dielectric exceeds the threshold value, it is fundamental to select optimal waveforms. For instance, previous results ([69]) show that thrust production is the highest with negative sawtooth. In fact, a positive sawtooth creates intense filaments near the exposed electrode (instantaneous anode) which causes a strong ionic wind only close to the surface.

On the other hand, a negative sawtooth causes the dielectric surface to charge with electrons from the exposed electrode, which is now the instantaneous cathode. This behaviour prevents the electric field from reaching high values. Consequently, the discharge is more uniform. In this case, ionic wind reaches higher maximum values and it is also more uniform (see Fig. 2.28). The sinusoidal waveform is another valid solution, since symmetrical waveforms produce larger mean thrust. Triangular and square waves are less effective.

2.2.6 Influence of external parameters

The efficacy of DBD plasma actuators for aerodynamic flow control has been demonstrated in several studies, performed under well-controlled laboratory environmental conditions. However, application of these devices for active flow control on aircraft is more critical, due to the wide range of ambient conditions. On the other hand, this aspect is much more delicate for corona actuators than for DBDs. Numerous studies are reported in the following paragraphs to characterize environmental influences.

Effect of pressure

The electrical characteristics and the produced electric wind of a single DBD were investigated by Benard et al. [70] for several ambient air pressure values. The analysis demonstrated that a decrease in pressure induces an increase in the consumed power (at constant voltage), and an increase in the current peaks in number and intensity. The produced electric wind is also greatly modified by the ambient air pressure conditions. Fig. 2.29 shows the different behavior of plasma discharges as well as voltage and current.

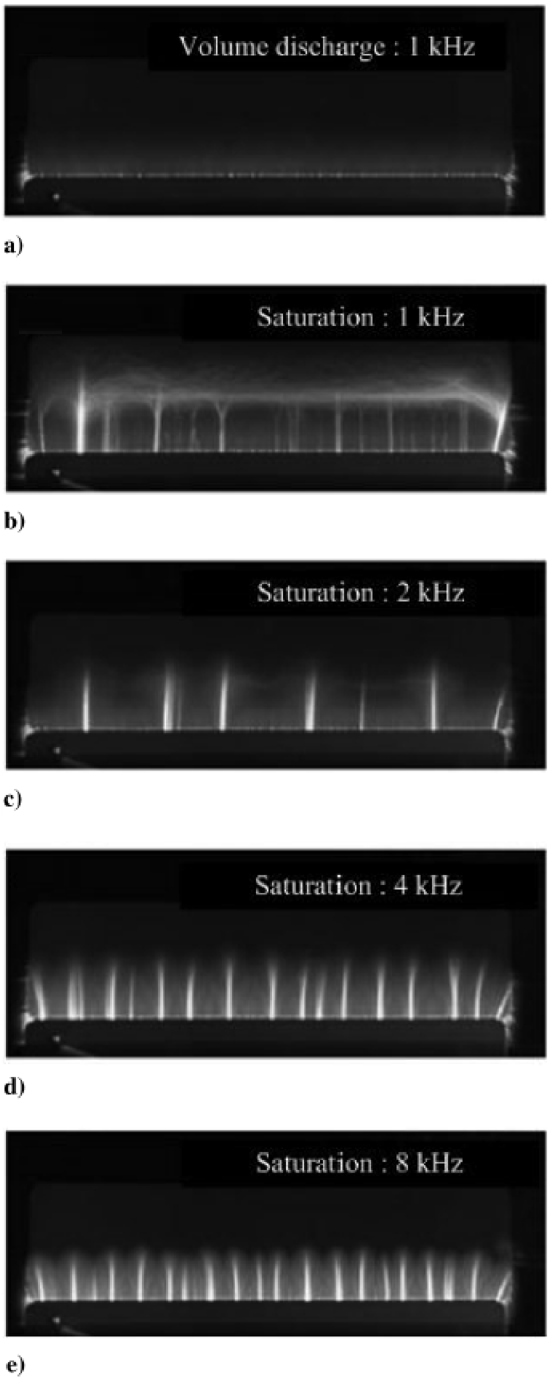

Figure 2.26: Effect of AC frequency on plasma filamentary structure [55].

Effect of air humidity

Anderson and Roy [71] reported preliminary experiments assessing the effect of relative humidity (RH) on the surface pressure coefficient over the range of $43\% \leq RH \leq 53\%$.

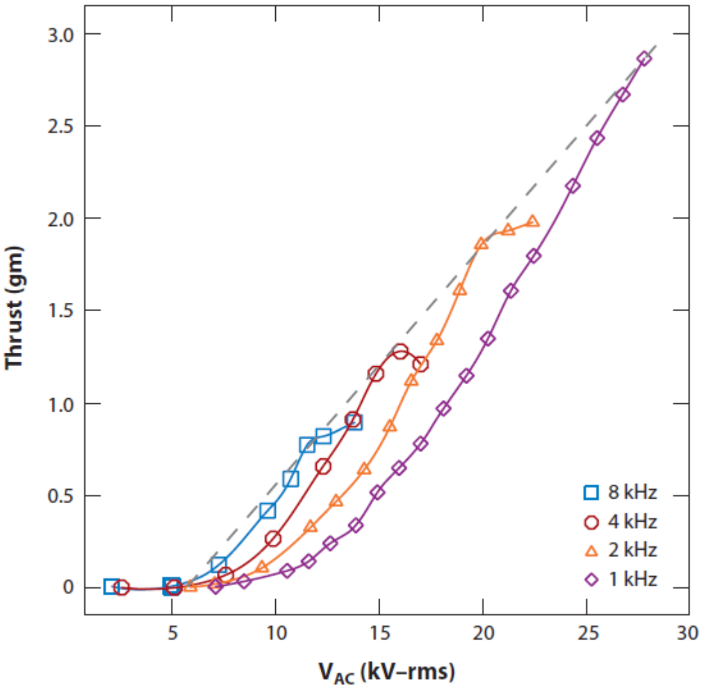

Figure 2.27: Induced thrust as a function of AC frequency [68].

They suggested a modest increase in actuator performance with relative humidity. A more recent study by Benard et al. [72] over a wider range of $40\% \leq RH \leq 98\%$ reported a reduction in plasma-induced wall jet velocity with increased RH. Wicks and Thomas [73] found that the reduction in reactive thrust produced by the actuator is negligible for $RH < 40\%$. For higher levels of relative humidity, a very significant reduction (approaching 70%) in the actuator-induced thrust is observed. The behaviour of the discharge for low and high RH is shown in Fig. 2.30.

Effect of temperature

Erfani et al.[74] investigated the impact of temperature on the performance of plasma actuators by measuring the maximum induced velocity with a PIV analysis. Results demonstrated that a hotter surface of the actuator leads to higher velocities and also higher body forces by consuming only slightly higher power. In particular, the maximum induced velocity that the hot actuator could achieve was 45.5% higher than the baseline case while requiring 6.1% more power. The power consumption of the cold dielectric actuator was 54.9% lower than the baseline case while inducing a velocity 43% lower. Therefore, performance of the actuator can be increased by using a source of heat beneath it. Another study [75] revealed that the induced force on the fluid increases almost linearly with increasing temperatures between 30 and $200°C$.

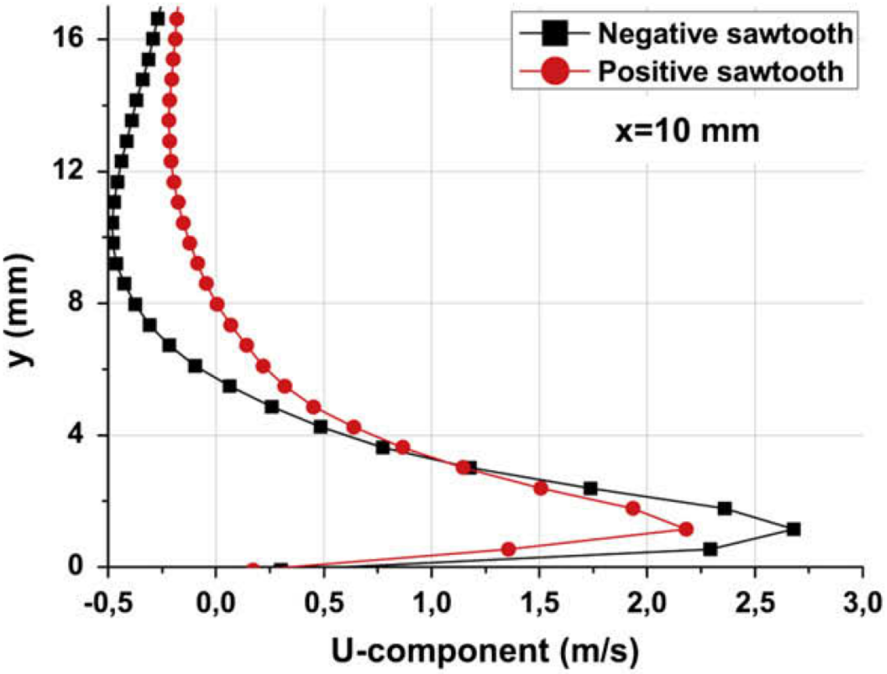

Figure 2.28: Induced velocity profile for positive and negative sawtooth [69].

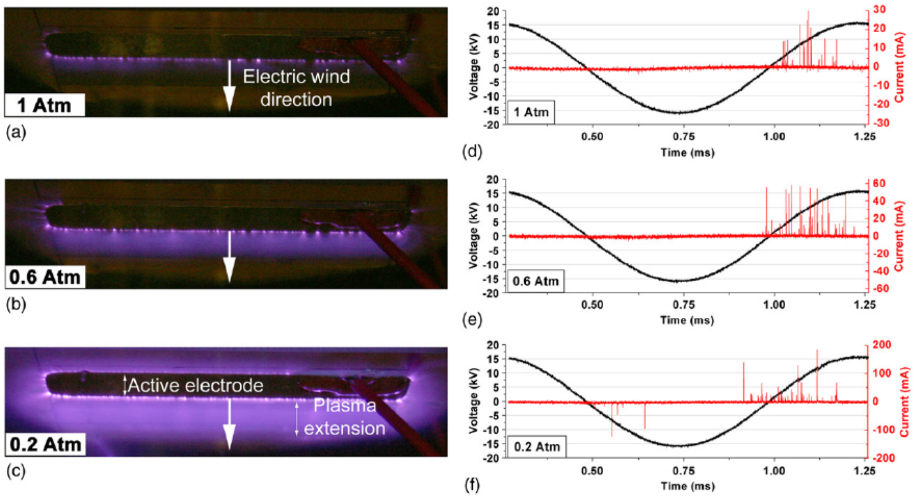

Figure 2.29: Photographs (top view) of the plasma discharge with a 1 s exposure time (a)–(c) and voltage and current of the DBD at 1 atm (d), 0.6 atm (e) and 0.2 atm (f). [70].

Effect of free air stream

The effect of the airflow on the performance of DBD plasma-actuators was investigated experimentally by [76]. In order to analyze the actuator's performance, luminosity

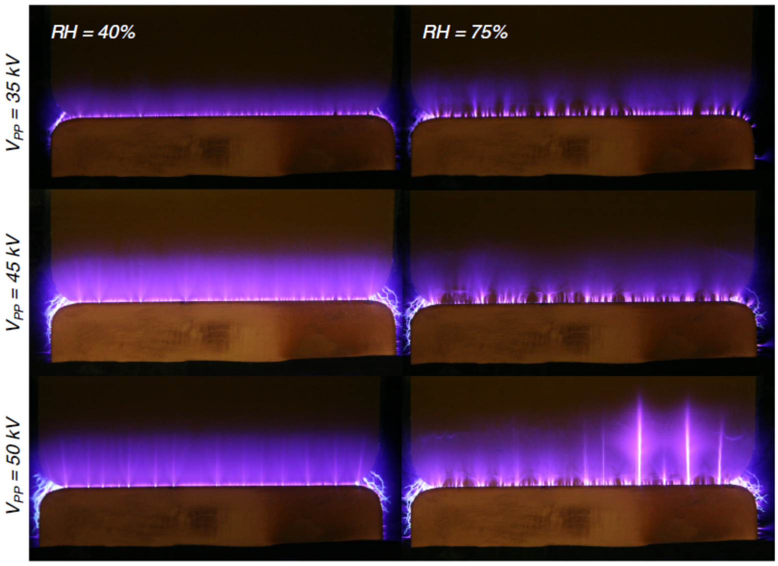

Figure 2.30: DBD discharge at ambient and high RH [73].

measurements have been carried out simultaneously with the recording of the relevant electrical parameters. A performance drop of about 10% was observed for Mach numbers $M < 0.2$. The results at higher Mach numbers ($0.4 < M < 0.8$) revealed an even more pronounced reduction of about 30%.

A detailed study of the overall discharge process can be found in [77]. Results showed that the glow component of the plasma is reduced and the discharge becomes more filamentary at high speed. Most important are the changes in individual micro discharges: a reduction of the light pulse emission duration by one order of magnitude is found, from 500 to 50 ns, when airflow velocity is increased from zero up to an isentropic Mach number of 0.7. These measurements indicate that there is a change in the breakdown mechanism, a transition from a Townsend breakdown to a streamer breakdown when the airflow velocity is increased.

2.2.7 Unsteady actuation

DBD actuators are characterized by an inherently unsteady regime, since the behaviour in the two half-cycles is very different. However, the AC frequency supplied to the actuator is far greater than the characteristic frequencies of the fluid, typically allowing the assumption of a quasi-steady state.

On the other hand, unsteady actuation consists of cycling the AC high voltage (carrier) with a square wave with a much smaller period than the carrier one. The ratio between the time in which the square wave is non-zero and its period is the duty cycle (see Fig. 2.31).

The unsteady period T has to be related to the characteristic frequency of the flow phenomenon we wish to control. In particular, Corke et al [78] found an optimum condition for the forcing frequency corresponding to a unitary Strouhal number, defined as $St = fC/U_\infty$, where f is the actuator forcing frequency, C is a characteristic length of separation and U_∞ is the free stream velocity. The separation length for a symmetric airfoil like the

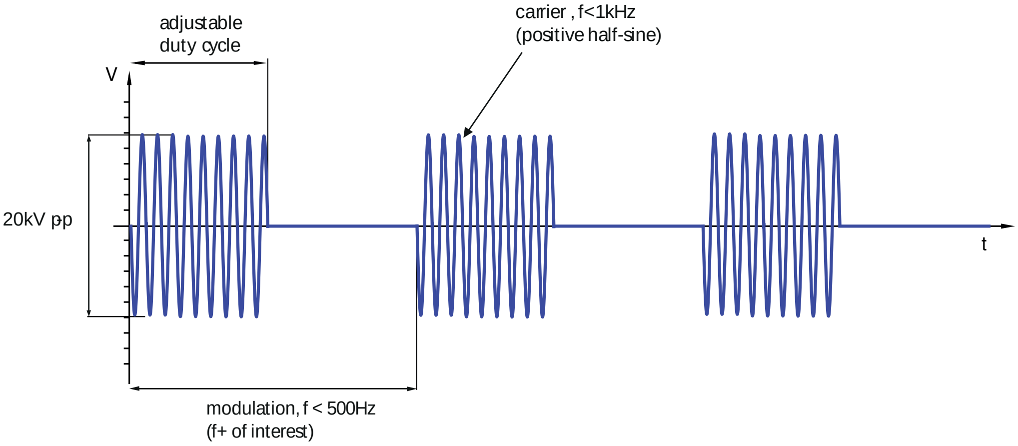

Figure 2.31: Duty cycle explanation.

NACA 0015 used in this work is simply the chord.

While in classic actuation the goal is to produce a strong ionic wind to energize the boundary layer, unsteady actuation relies on the formation of coherent vortical structures. It is expected that the global flow changes derive from phased interactions with the natural large-scale flow structures[79]. Unsteady actuation is also an effective way to reduce the electrical power consumption. As a matter of facts, modulating the AC input voltage with a square wave reduces power of a fraction equal to the duty cycle. Recent studies demonstrated that unsteady actuation is more effective than the classical steady one. In particular, Benard et al. [79] investigated the influence of the modulation frequency and the duty cycle on an axisymmetric airfoil. Results reported an optimal effect at a non-dimensional frequency around 0.5 for duty cycles between 6% and 50%. DBD plasma actuators have been used by Jukes et al. [80] to control the flow around a circular cylinder at $Re = 15000$, where the near-wake structure was studied using time-resolved particle image velocimetry. It was shown that the vortex shedding was suppressed when the surface plasma placed near the natural separation point was activated in a pulsed mode at nondimensional frequency, f+, above 0.6. Little [29] investigated the efficacy of a single DBD plasma actuator for controlling turbulent boundary-layer separation from the deflected flap of a high-lift airfoil. The modulation waveform used to excite low-frequency perturbations with a high-frequency plasma carrier signal had a considerable effect on the actuator performance.

2.3 Other configurations of plasma actuators

2.3.1 Multiple DBDs

The extension length of a single surface DBD is limited to about 2 cm. A way to extend its use to large-scale applications is using several single surface DBDs in series. The right positioning of these actuators plays a fundamental role since the mutual interactions between successive discharges often result in limited effectiveness of this configuration. In particular, if the electrodes are placed at a short distance, a backward discharge forms, called “cross talk” phenomenon, reducing the benefits of the multiple DBSs configuration. A thorough explanation of this aspect can be found in [81]. Benard et al. [49] investigated a three-electrode design in order to reduce the mutual interactions. Results demonstrate that the backward flow can be reduced by 65%, granting a lower power consumption of the actuator. Fig. 2.32 shows the innovative configuration dedicated to the reduction of the backward flow.

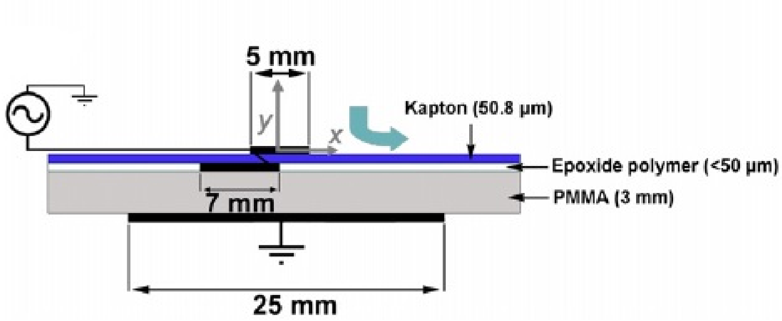

Figure 2.32: Three-electrode DBD design [49].

2.3.2 Sliding discharges

Another configuration of plasma actuators is the sliding discharge plasma actuator. This system is composed of two electrodes flush mounted on each side of a dielectric, like a single DBD, and a second air-exposed electrode supplied by a dc voltage (see Fig. 2.33). The polarity of the dc supply influences the electrical and mechanical characteristics of the actuator. In particular, a negative polarity produces a luminescent plasma sheet that occupies the whole electrode gap, while a positive polarity results in a discharge visually similar to the one produced by a DBD [82]. The advantage of these configurations is their effectiveness in large-scale applications, because the discharge extension may be increased up to the gap between electrodes (1) and (3). Several studies have been conducted so far [82],[83],[84],[85].

2.3.3 Nanosecond pulsed DBD

Nanosecond-pulse-driven DBD plasma actuators rely on a different mechanism of controlling the boundary layer to promote flow reattachment. The main phenomenon is energy transfer to and heating of the near-surface gas layer, while actuator-induced velocities are almost negligible for nanosecond pulses [86]. The overheating in the discharge region induces the formation of shock waves and secondary vortex flows, causing a transversal momentum transfer to the boundary layer. The normally separated flow is therefore reattached thanks to the formation of coherent structures [87]. More detailed information about these aspects can be found in [86],[87],[88],[89],[90].

2.3.4 LAFPA

Another heat based mechanism suitable for controlling high Reynolds and supersonic flows employs the LAFPA (localized arc filament plasma actuators). An arc filament is initiated between the electrodes embedded on the surface to generate rapid (few microseconds) local heating. The heating causes a local pressure rise, and volume change adjacent to the surface of the nozzle in the flow. The arc filament can be generated from DC to

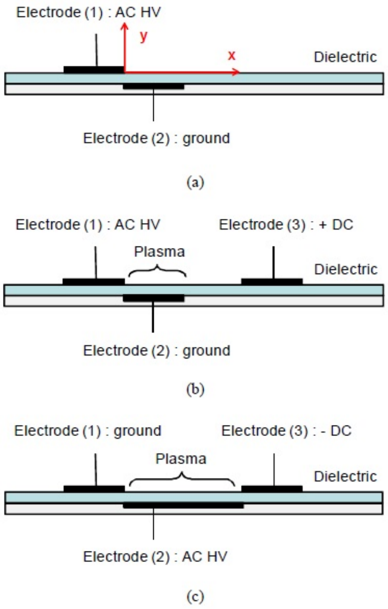

Figure 2.33: Sketch of three different types of plasma actuators: (a) single DBD, (b) extended DBD, (c) sliding discharge [82].

very high frequencies, covering the entire range of jet column and shear layer instabilities [91]. Numerical and experimental studies are found in literature [91],[92],[93].

Chapter 3

Experimental setup

3.1 Wind tunnel

Experiments have been conducted in the "red wind tunnel" of the Aerodynamics laboratory of Politecnico di Milano (see Fig. 3.1). This open-circuit wind tunnel has a closed test section of (W, H, L) $500mm \times 700mm \times 2000mmm$. The lateral test section walls are partially made of PMMA to provide optical access to the model.

After a honeycomb grid at the beginning of the circuit, there is a settling chamber followed by the nozzle. The convergent section is $3000mm$ long with a contraction ratio of 6.25. Downstream the test chamber there is a short divergent section that changes from rectangular to circular to accommodate the fan. The fan is a 7-blades rotor of $700mm$ diameter. A drive belt connects it to the three-phase electrical motor located outside the tunnel. Maximum velocity is 25 m/s, controlled by a 40kW $HitachiL300Pseries$ inverter.

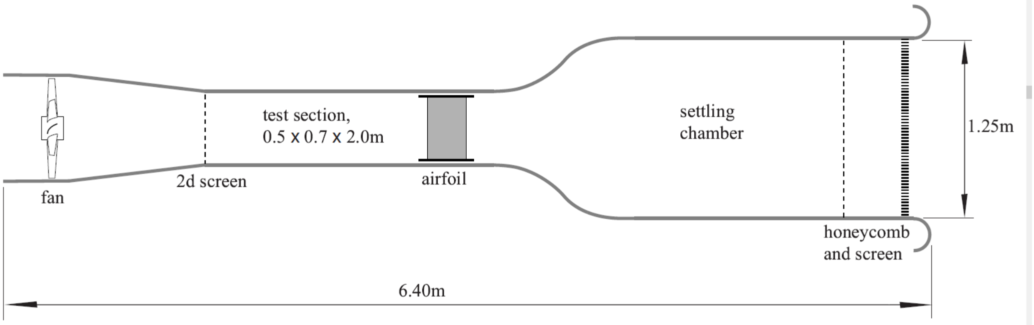

Figure 3.1: Red wind tunnel sketch.

3.1.1 Wind tunnel calibration

Flow velocity in the test section is controlled through a differential static pressure measurement. Pressure taps are installed between the beginning and the end of the convergent section. The acquisition is made with a differential pressure transducer with a FS of $250Pa$. The advantage of this measurement is that it does not affect the wind tunnel flow. However, a calibration procedure is necessary to link the differential pressure to the velocity. The velocity is immediately computed from the dynamic pressure with the following relation:

$$P_{dyn} = \frac{1}{2}\rho U^2 = K\Delta P_{static} \tag{3.1}$$

Dynamic pressure is measured by a Pitot probe located in the test section while differential static pressure is simultaneously acquired. The procedure to determine the calibration constant K consists of acquiring different pressure measurements at different speeds.

Dynamic pressure of the Pitot probe is measured through a differential pressure transducer *Furness FO510* that has an accuracy of ±0.25% of the measured value between 2 and 200 Pa.

3.2 Airfoil

The experiments have been conducted on a NACA 0015 airfoil due to the large amount of data available in literature [27, 28, 49, 78, 94–98]. The airfoil has a $250mm$ chord and a $470mm$ span. It is made of UREOL, a type of polyurethane which is easily machinable. It is also a good electric insulant with low porosity which prevents it from absorbing humidity.

Since plasma actuators are most effective near the separation point, they must be installed in the proper position. Jolibois et al in [27] performed an optimization of the position (along the chord) of a DBD actuator on a NACA 0015 airfoil. The results show that the actuator has to be near or upstream the separation point to be effective. Separation at the Reynolds numbers of this work (1.7×10^5 and 3.5×10^5) occurs nearly at the leading edge (2% of the chord). In order to fit the actuators on the airfoil, a C-shaped seat has been machined on it. The electrodes are mounted on a plexiglas insert which fits exactly with the seat on the airfoil. Fig. 3.2 shows the airfoil fitted with endplates and a DBD actuator [58].

3.2.1 Plexiglas insert

The electrodes support is made of PMMA. It has been thermoformed using a C-shaped UREOL mold. The thickness of the plexiglas sheet is $2mm$. The inserts are linked to the airfoil through eight $M3 \times 6mm$ nylon screws to ensure electrical insulation.

3.2.2 Endplates

The airfoil has two endplates. They are cut from $2mm$ thick plexiglas sheets in a rectangular shape with rounded ends. They are meant to reduce tridimensional effects of the flow. Due to practical limitations of the setup, the endplates are too small to obtain a perfectly two-dimensional flow over the airfoil. We expect some 3D flow effects to be present.

3.2.3 Support stings

The connection between the balance and the airfoil is made with two stings, one for each side. The stings are $16mm$ in diameter and $180mm$ long. Initially both stings were made of nylon to avoid Foucault currents to induce noise on balance signals. This problem has arisen in a previous experiment [99] performed with a similar setup, but with metallic

Figure 3.2: Airfoil with a DBD actuator and plexiglas endplates installed [58].

stings. However, during tests conducted at $20m/s$ we realized that torsional stiffness was insufficient. At high angles of attack, the accuracy of the angular positioning was compromised. It has been necessary to realize a new steel sting with a stiffer linking method with airfoil and rotation system. Fortunately, no electro-magnetic disturbances due to Foucault currents were measured. Further details are reported in App. C.

3.3 Plasma actuators

Plasma actuators are made of two $0.12mm$ thick aluminium electrodes, $400mm$ long. They are attached on the plexiglas inserts. We tested a classical plate-to-plate DBD and wire-to-plate corona as a baseline case, and then we investigated the multi-tip geometry for the active electrode, which is a generalization of the serrated edge shape (see[57]). The geometries tested in this thesis have been chosen from the best of previous works ([57, 58, 100]). They are represented in Tab. 3.1, 3.2.

3.3.1 DBD actuators

All DBD actuators have a $50mm$-wide grounded electrode. In order to avoid undesired plasma formation on the lower side of the dielectric, the covered electrode is coated with silicon insulating paint.

The exposed electrode of the plate-to-plate actuator is $8mm$ wide. In order to compare this actuator with the others, multi-tip electrodes are realized with an $8mm$ base from which the tips protrude along the chord. One side of the encapsulated electrode as well as the valleys of the exposed electrode are aligned with the leading edge because plasma formation starts in the valleys for DBDs. Figure 3.3 shows the geometrical parameters of

Table 3.1: List of DBD actuators tested in this campaign.

Geometry	h (mm)	w (mm)	$r = \frac{h}{w}$	$n = \frac{N}{S}(m^{-}1)$
D1 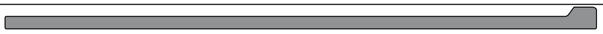	0	0	-	-
D3 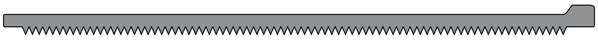	5	5	1	200
D5 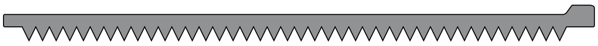	10	10	1	100
D7 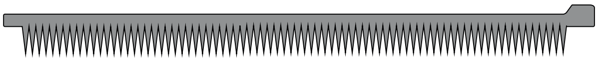	20	5	4	200
D14 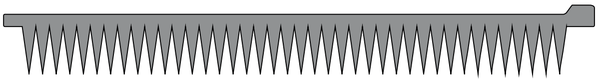	35	10	3.5	100
D15 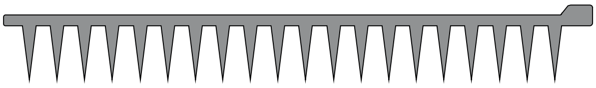	40	10	4	50
D16 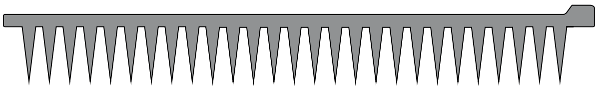	40	10	4	66.6
D17 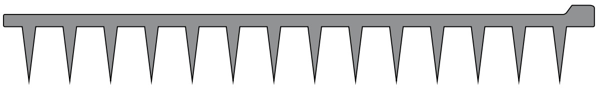	40	10	4	33.3

Table 3.2: List of Corona actuators tested in this campaign.

Geometry	h (mm)	w (mm)	$r = \frac{h}{w}$	$n = \frac{N}{S}(m^{-}1)$
C1 	0	0	-	-
C6 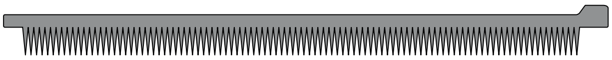	20	4	5	250
C13 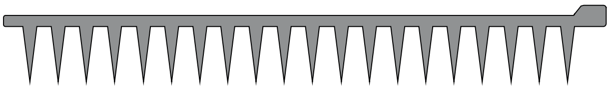	40	10	4	50

the actuators. h is the tip height, w is the tip width, $r = h/w$ is the tip sharpness ratio and $n = N/S$ is the number of tips per unit length.

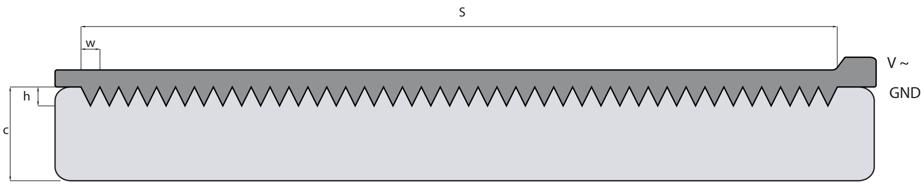

Figure 3.3: DBD active electrodes geometry.

3.3.2 Corona actuators

All corona actuators have a $25mm$-wide cathode on the suction side of the airfoil. The electrode gap is $g = 15mm$. The wire of the wire-to-plate actuator and the tips of the anode are aligned with the leading edge, unlike DBDs, since, in this case, plasma is generated at the tips. Figure 3.4 shows the geometrical parameters of the electrodes. g is the electrode gap h is the tip height, w is the tip width, $r = h/w$ is the tip sharpness ratio and $n = N/S$ is the number of tips per unit length.

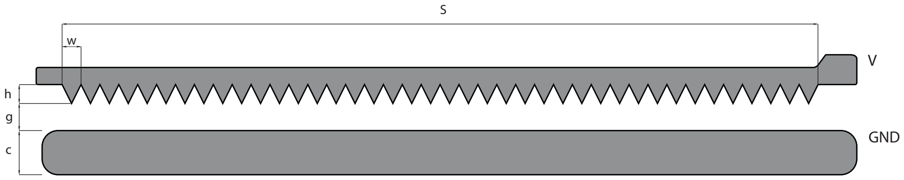

Figure 3.4: Corona electrodes geometry.

3.3.3 Power supply

The driver of the actuators consists of a linear amplifier and a transformer. The scheme of the electric circuit of the HV generator is shown in Fig. 3.8 .

The input signal is an audio sinusoidal waveform $Asin(\omega t)$ modulated with a square wave. In order to obtain accurate waveforms with any duty cycle and modulation frequency, a .wav file is generated by a Matlab routine. The HV (High Voltage) generator mainly consists of an audio amplifier and a transformer. The first multiplies the input signal amplitude of a factor of 36. The latter is a purposely built device with a power of $200VA$. Its voltage ratio depends strongly on the input signal frequency. Fig. 3.9 shows this trend, measured with a purely resistive load. It's worth noting the plateau between 400Hz and 1500Hz but plasma actuators are mainly a capacitive load. Hence the actual frequency response is different from the one with a purely resistive load. The plateau is restricted between $400Hz$ and $800Hz$. Beyond these values, the output signal amplitude decreases at constant input amplitude. Besides, the optimal working frequency of an HV amplifier connected to a plasma actuator depends on the characteristics of the actuator itself: an increase in output power and current of the transformer is obtained when it operates at the resonance frequency f_{res}. As observed by Kriegseis et al in [101], f_{res} depends on the type of actuator. Fig. 3.10 shows current and power generated by the

HV amplifier at constant voltage for two actuators of different length L. The resonance frequency decreases with L. In our case, the carrier frequency of the excitation signal is set to $800Hz$ for all the actuators except D15, D16 and D17 which are fed with a signal at $640Hz$. These actuators require more power than the others due to their large active length combined with tip separation which increases the discharge length (see Sec. 4.4.4). Pulsed actuation is obtained modulating the carrier signal (sine wave) with a square wave. A representation of the ideal waveforms for DBDs and corona is shown in Fig. 3.5, 3.6 respectively. In the latter case, the AC modulated waveform is modified by the clamper which cuts the negative part of the sine wave and shifts the signal with a mean value through the capacitor. Corona actuators are actually ignited only for a short time, when voltage is close to the peak value (see Fig. 3.7). The modulation frequencies range from $20Hz$ to $480Hz$ and they are reported in Tab. 3.3 in non-dimensional form as:

$$f^{+} = \frac{f_{mod} c}{U_{\infty}} \tag{3.2}$$

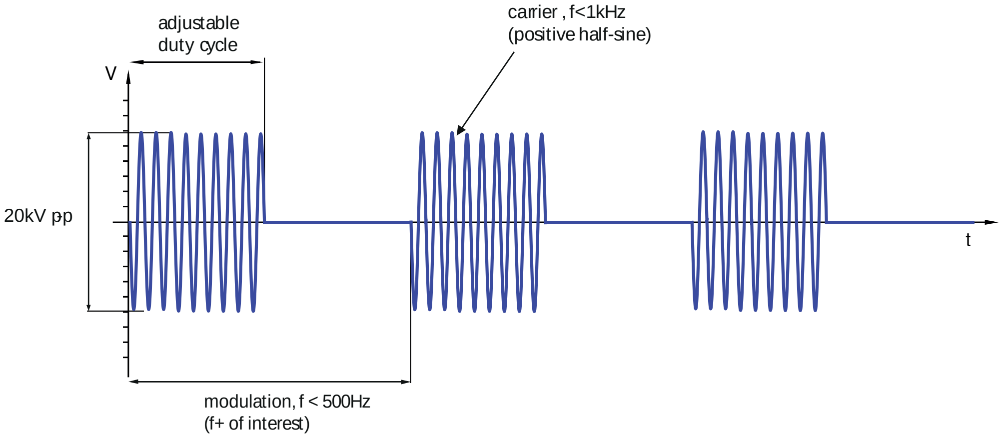

Figure 3.5: Representation of the ideal pulsed waveform used for DBDs.

Table 3.3: Waveforms used in the test campaign. Carrier frequency is $800Hz$ or $640Hz$ (for D15, D16, D17).

Modulation frequency (f^+)	Duty cycle (%)
0.5	20
0.5	50
0.75	20
0.75	50
1.25	20
1.25	50
1.5	20
1.5	50
2	20
2	50
3	20
3	50
5	20
5	50
6	20
6	50
1	5
1	7.5
1	10
1	20
1	30
1	40
1	50
1	60
1	80
1	100
4	5
4	7.5
4	10
4	20
4	30
4	40
4	50
4	60
4	80

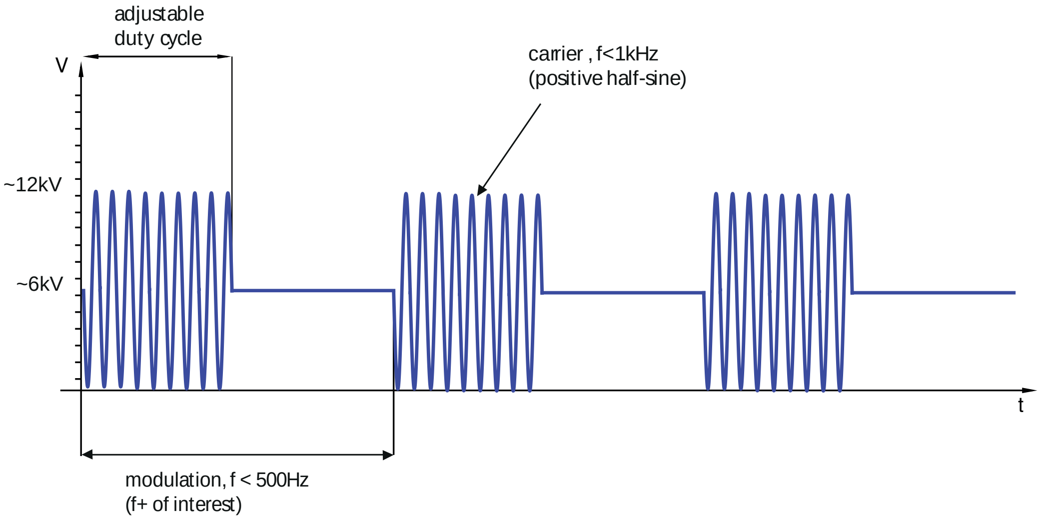

Figure 3.6: Representation of the ideal pulsed waveform used for corona actuators.

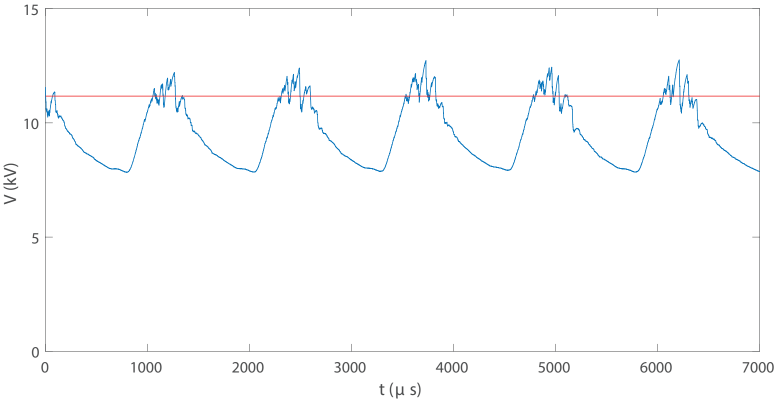

Figure 3.7: Real voltage across a corona actuator in the active phase (blue line) and ignition voltage in still air $V_{ign} = 11.25kV$ (red line).

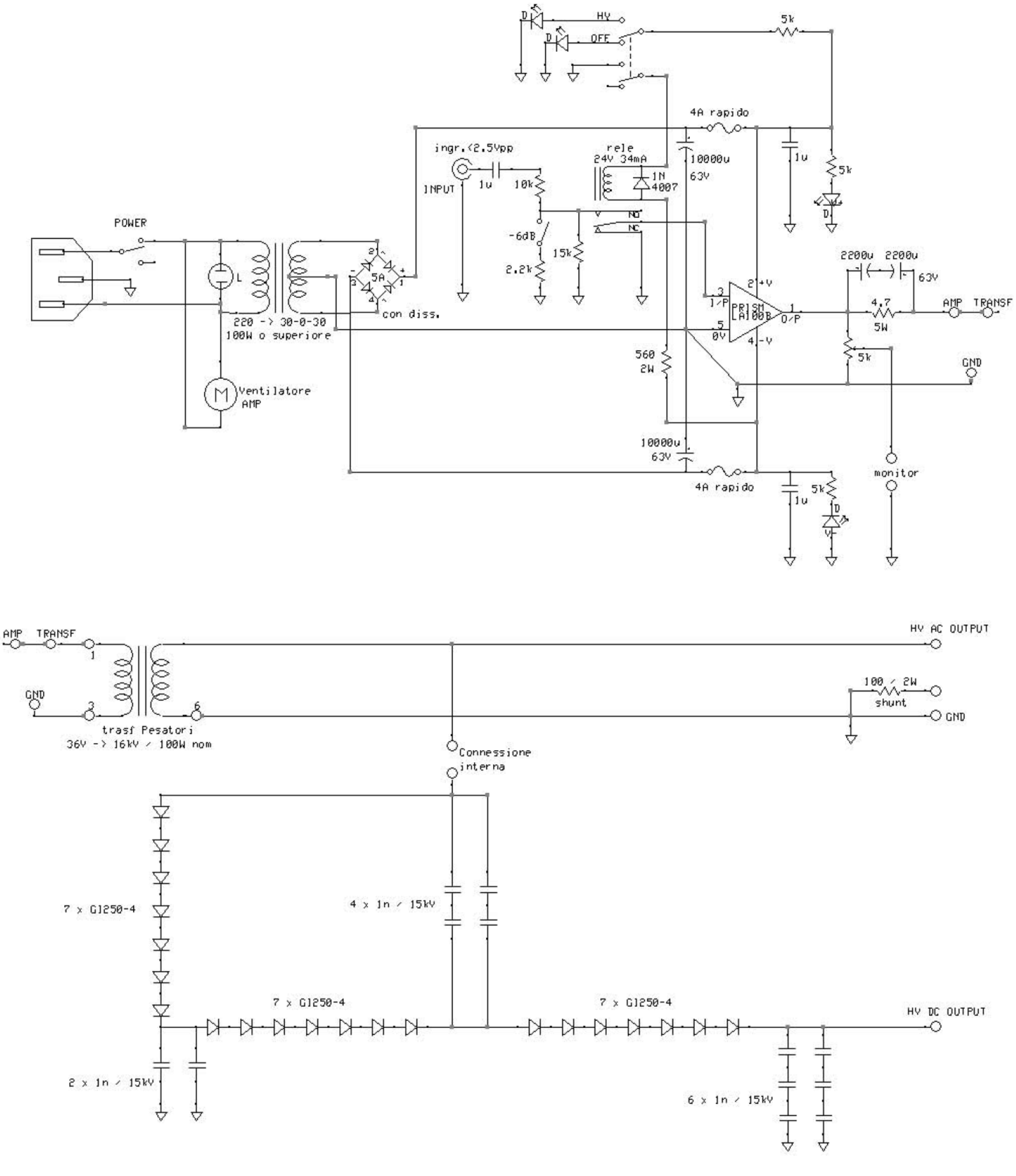

Figure 3.8: Scheme of the electric circuit of the High voltage generator [102].

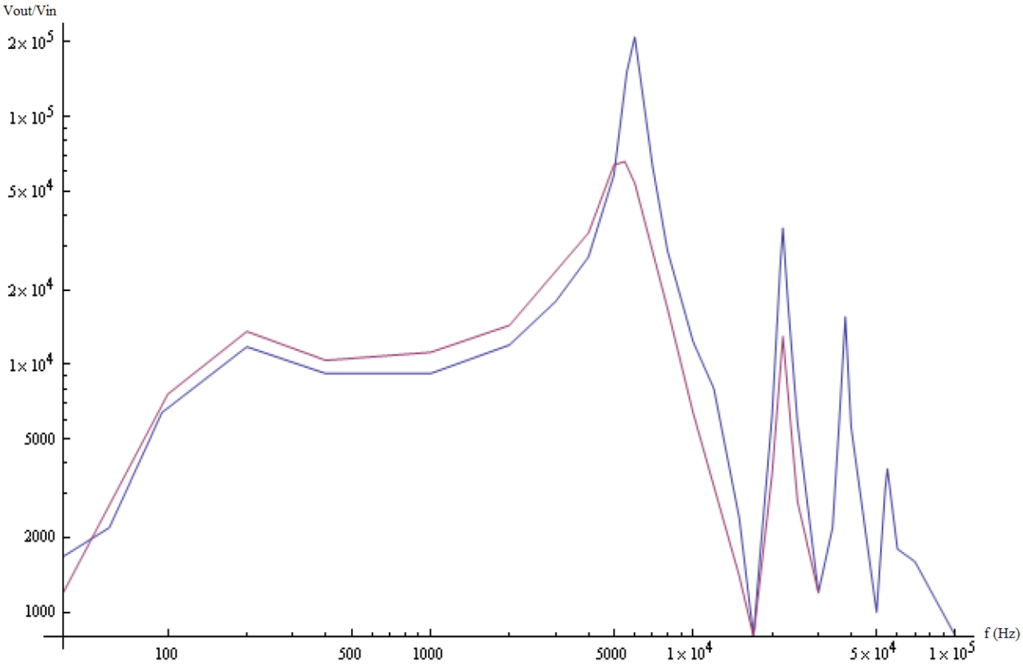

Figure 3.9: Transformer frequency response. V_{out}/V_{in} with respect to input signal frequency without any load (blue line) and with a purely resistive load of $3M\Omega$(red line) [102].

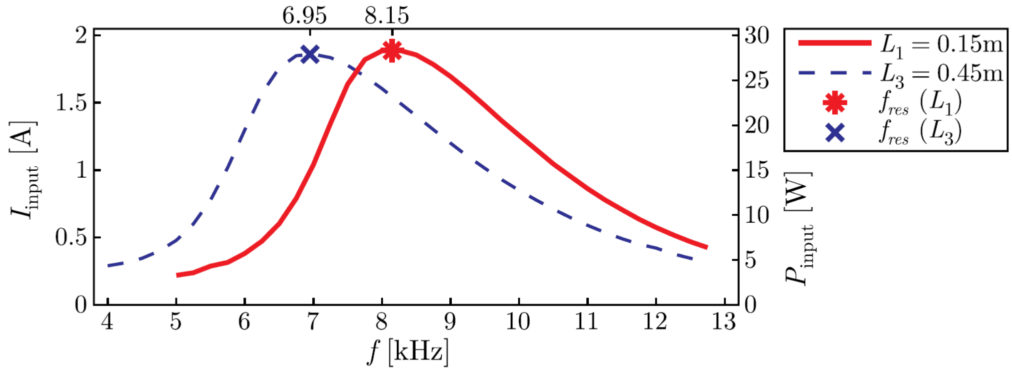

Figure 3.10: Current and power versus excitation frequency for two actuator lengths [101].

As far as the corona actuators are concerned, the power supply setup is slightly different. An external clamper with a rectifier, in series with a ballast resistor is connected between the high voltage AC output and the actuator (see Fig. 3.11). The signal on the actuator is shown in Fig. 3.7. Unlike a simple DC voltage, this peculiar waveform stabilizes the discharge, because it reduces the accumulation of electric charge which easily leads to a spark transition. A $4.4M\Omega$ ballast resistor serves the purpose to limit the current flowing to the actuator, in case of spark formation. Fig. 3.11 shows the electric circuit of the clamper.

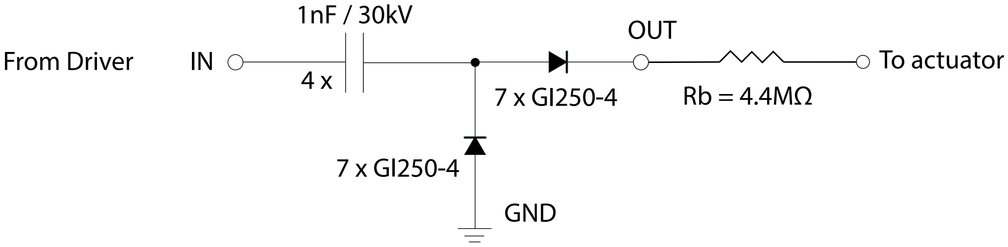

Figure 3.11: Representation of the electric circuit of the clamper.

3.4 External balance

Lift and drag are measured by a balance with four load cells HBM S2M. Two transducers measure lift and the others are sensible to drag. Load cells are of S-type and measure both static and dynamic loads of traction and compression. The maximum load before failure is 1000% of the full scale.

Considering a wind tunnel speed from $5m/s$ to $20m/s$, estimated aerodynamic loads range from $0.128kg$ to $3.76kg$ for lift and from $0.004kg$ to $0.128kg$ for drag on our NACA 0015. Also considering the static loads due to the weight of airfoil and other components, the choice of the load cells fell on $100N$ range for lift and $50N$ for drag. Accuracies are $0.02N$ and $0.01N$ for lift and drag respectively. A Wheatstone bridge generates an output signal of a few mV of amplitude, proportional to the deformation of the cell. In order to reduce the effect of electromagnetic disturbances on the load cells signals, the latters are amplified with a signal conditioning system. Finally, the conditioned signals are fed to the *Compact DAQ 9188 National Instruments* data acquisition platform. The ADC sends the balance signals to the PC where a *Labview* program acquires them at $f_s = 4000Hz$ and performs an average over 5s.

3.4.1 Balance supports

The support of the whole airfoil-balance system is provided by a rigid structure of *Bosch Rexroth* anodized aluminium bars (see figure 3.12). The requirements of this structure are high precision coupling with the balance system, to ensure symmetry and avoid undesirable loads on the airfoil and high stiffness. In fact, it is necessary to limit the interaction between aerodynamic loads and support vibrations.

On the left side of the support the airfoil is connected to the balance by means of the rotary positioning system. The right side has a dummy system which resemble the rotation system in geometry and weight, to preserve symmetry. The dummy system consists of a hole, the same size of the rotation system, in which a teflon bushing seats and leaves the airfoil free to rotate. Some lead weights are attached to the right load cells to match the weight of the left assembly.

3.4.2 Balance calibration

The calibration procedure was performed by Modugno and Mulone in [58] by applying six different weights in four different directions. The relation between output signal and applied forces is:

$$v = Kf \tag{3.3}$$

where K is the calibration matrix.

By knowing exactly the applied loads and their directions, it is possible to evaluate K. Consequently, the relation $f = Ev$ gives the desired loads given the relative voltage signal. E is simply the inversion of K. Σ_E is the matrix of the standard deviation of E:

$$E = \begin{bmatrix} -1.0192 & -0.0002 \\ -0.0063 & 1.0254 \end{bmatrix} \tag{3.4}$$

$$\Sigma_E = \begin{bmatrix} 0.0019 & 0.0039 \\ 0.0024 & 0.0012 \end{bmatrix} \tag{3.5}$$

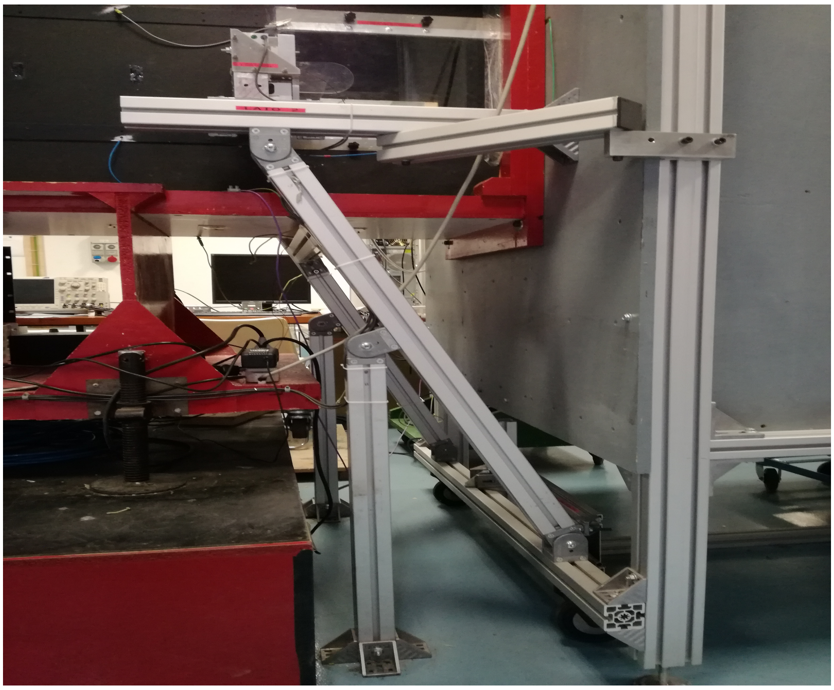

Figure 3.12: Side view of the support structure of the model.

Extra-diagonal terms are almost null, allowing the use of a linear calibration matrix. Third-order non-linearity can also be neglected since the balance shows a symmetrical behaviour with respect to the direction of the applied loads.

3.4.3 OWIS rotary system

The angular positioning system is an *OWIS DMT65-D35-HSM*. It allows an accurate setting of the angle of attack. This instrument is characterized by an accuracy of $174.5 \mu rad$ which is more than what is required for our purposes. The system is driven by a stepper motor, controlled by the related software *OWIS PS10-SM*. Fig. 3.13 shows the test section of the wind tunnel with the airfoil mounted on the supports.

3.5 Other instruments

In this paragraph we describe the instruments we used for the experimental campaign in the wind tunnel.

- Oscilloscope: a Tektronix MDO4034C with bandwidth of 350MHz and a sample rate of 2.5GS/s. The first channel is used to monitor the input low voltage signal. The second channel is connected to the HV generator output through a voltage divider. Two other channels are used for electric power measurements. These have been made in two different ways. Normally, power is computed acquiring voltage and current on the secondary winding. It is also possible to measure them on the primary, obtaining a current signal with small influence of streamers and disturbances of the HV line. This procedure, once the transformer efficiency is known, leads to

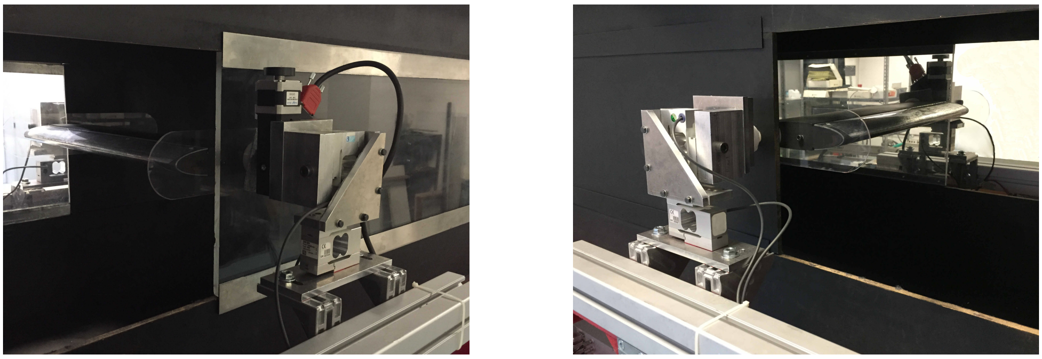
(a) Side 1 **(b)** Side 2

Figure 3.13: Close view of the test section. Positioning system side (a) and dummy support (b)[58].

an affordable measurement of the electric power consumption. Further details are reported in Par. 4.4.4. When the acquisition is made on the primary winding of the transformer, a shunt resistor of 0.33Ω is placed between the AMP and TRANSF terminals which are usually short-circuited (see Fig. 3.8). Two channels are used to acquire the signals in the terminals. Voltage on the primary winding V_{tran} is acquired from the TRANSF terminal. Current is obtained by the voltage across the shunt resistor:

$$I_{prim}(t) = \frac{V_{amp}(t) - V_{tran}(t)}{R_{shunt}} \tag{3.6}$$

Power is then immediately obtained by integrating the voltage and current signals on the primary winding over a period:

$$P_{prim} = \frac{1}{T}\int_0^T V_{tran}(t) I_{prim}(t) dt \tag{3.7}$$

When the acquisition is made on the secondary winding, power is acquired by means of a different shunt resistor of 100Ω, placed on the actuator ground return. In this case, voltage across the shunt can be measured with a single channel of the oscilloscope, since the resistor is directly connected to ground.

Power is calculated in the same way as in the primary acquisition:

$$P_{sec} = \frac{1}{T}\int_0^T V_{act}(t) I_{act}(t) dt \tag{3.8}$$

$V_{act}(t)$ is the voltage across the actuator, measured with a voltage divider (described below). $I_{act}(t)$ is the current flowing into the actuator and the shunt resistor.

- Digital multimeter: it is connected to the differential pressure transducer across the convergent section of the wind tunnel. It is used to set and control wind tunnel speed.

- Voltage divider: the output voltage of the power supply is of the order of $20kV$ peak-to-peak for DBDs and $13kV$ (peak) for Corona actuators. In order to measure it with the oscilloscope, it needs to be reduced substantially. Therefore, we use a voltage divider with total impedance of $47M\Omega$ (with an accuracy of $\pm 1\%$) and $V_{out}/V_{in} = 1/1000$.
- Thermometer and barometer: they have been used to calculate air density and consequently wind tunnel speed during the tests. The accuracy of the thermometer is $\pm 0.5K$ and that of the barometer is $\pm 0.1mbar$

3.6 Measurement procedure

The performance of the actuators has been measured at two different speeds $10m/s$ and $20m/s$ corresponding to $Re = 163000$ and $Re = 326000$. The angle of attack sweeps from $0°$ to $35°$ until the effect of the actuator is negligible. For each actuator (both DBDs and Corona), several modulated waveforms have been tested (see Tab. 3.3 for the complete list). The unsteady actuation on corona actuators is, to the best of our knowledge a novelty. Voltage is kept constant at $20kV$ for DBDs and at $13kV$ for Coronas with a carrier frequency of $800Hz$. The only exceptions are the D15, D16 and D17 which have been tested with a carrier frequency of $640Hz$. These actuators have the highest power consumption. For this reason, the HV transformer causes a non-negligible distortion of the output signal at $800Hz$.

In order to avoid hysteresis effect, airfoil angular position was always brought back to zero before changing the angle of attack.

Given the airfoil symmetry, the zero lift position was easily found after measuring a C_L value close to zero ($C_L < 10^{-3}$).

The offset values of the four load cells have to be acquired before turning the wind tunnel on, so they can be subtracted afterwards, in order to eliminate the static loads from the purely aerodynamic analysis. Each measure was acquired multiple times and averaged to assess repeatability, specially for angles near stall condition.

3.7 Blockage corrections

Considering the size of the airfoil and the test section area, blockage effects could not be neglected. Following Pope [103] we adopted these corrections during post-processing of the data:

- solid blockage model of [104]:

  $$\epsilon_{sb} = \Lambda\sigma \tag{3.9}$$

  where $\Lambda = 0.3$ for a NACA0015 airfoil and σ is:

  $$\sigma = \frac{\pi^2}{48}\left(\frac{c}{h}\right)^2 \tag{3.10}$$

  where c is the airfoil chord and h the height of the test section.

- wake blockage correction proposed by [105]:

  $$\epsilon_{wb} = \frac{c/h}{2} C_{Du} \tag{3.11}$$

  where C_{Du} is the uncorrected drag coefficient.

- streamline curvature [104]

  $$\Delta C_{Lsc} = -\sigma C_{Lu} \tag{3.12}$$

  $$\Delta\alpha_{sc} = \frac{57.3\sigma}{2\pi} C_{Lu} \tag{3.13}$$

  where C_{Lu} is the uncorrected lift coefficient.

- global corrections for angle of attack and force coefficients

  $$\alpha = \alpha_u + \frac{57.3\sigma}{2\pi} C_{Lu} \tag{3.14}$$

  $$C_L = C_{Lu}(1 - \sigma - 2(\epsilon_{sb} + \epsilon_{wb})) \tag{3.15}$$

  $$C_D = C_{Du}(1 - 3\epsilon_{sb} - 2\epsilon_{wb})) \tag{3.16}$$

- Corrections for velocity and Reynolds number:

  $$U = U_u(1 + \epsilon_{sb} + \epsilon_{wb})) \tag{3.17}$$

  $$Re = Re_u(1 + \epsilon_{sb} + \epsilon_{wb})) \tag{3.18}$$

3.8 Propagation of errors

Assuming independent Gaussian-distributed sources of error, it is possible to adopt the RSS method (Root Sum Square), which is represented by the following:

$$w_Z = \sqrt{\sum_i \left(\frac{\partial Z}{\partial x_i} w_{x_i} \right)^2} \tag{3.19}$$

3.8.1 Force coefficients

In this case Z is the lift and drag coefficient and w_Z the related uncertainty. The force coefficients are obtained from the balance output signals:

$$C_L = \frac{1}{\frac{1}{2}\rho U^2 S}(E_{11}V_L + E_{12}V_D) \tag{3.20}$$

$$C_D = \frac{1}{\frac{1}{2}\rho U^2 S}(E_{21}V_L + E_{22}V_D) \tag{3.21}$$

Where E_{ii} are the elements of the balance matrix, $S = bc$ is the airfoil surface, U the free stream velocity and ρ the air density obtained in the hypothesis of ideal gas:

$$\rho = \frac{P}{RT} \tag{3.22}$$

One should also recall that free stream velocity U is obtained from a pressure measurement:

$$P_{din} = \frac{1}{2}\rho U^2 = K\Delta P_{static} \tag{3.23}$$

It follows immediately:

$$U = \sqrt{\frac{2K\Delta P_{static}}{\rho}} \tag{3.24}$$

Thus the uncertainty of lift coefficient is:

$$w_{C_L} = \sqrt{\begin{aligned} &\left(\frac{\partial C_L}{\partial \rho} w_\rho\right)^2 + \left(\frac{\partial C_L}{\partial U} w_U\right)^2 + \left(\frac{\partial C_L}{\partial S} w_S\right)^2 + \left(\frac{\partial C_L}{\partial E_{11}} w_{E_{11}}\right)^2 \\ &+ \left(\frac{\partial C_L}{\partial E_{12}} w_{E_{12}}\right)^2 + \left(\frac{\partial C_L}{\partial V_L} w_{V_L}\right)^2 + \left(\frac{\partial C_L}{\partial V_D} w_{V_D}\right)^2 \end{aligned}} \tag{3.25}$$

And the uncertainty of the drag coefficient is:

$$w_{C_D} = \sqrt{\begin{aligned} &\left(\frac{\partial C_D}{\partial \rho} w_\rho\right)^2 + \left(\frac{\partial C_D}{\partial U} w_U\right)^2 + \left(\frac{\partial C_D}{\partial S} w_S\right)^2 + \left(\frac{\partial C_D}{\partial E_{22}} w_{E_{22}}\right)^2 \\ &+ \left(\frac{\partial C_D}{\partial E_{21}} w_{E_{21}}\right)^2 + \left(\frac{\partial C_D}{\partial V_L} w_{V_L}\right)^2 + \left(\frac{\partial C_D}{\partial V_D} w_{V_D}\right)^2 \end{aligned}} \tag{3.26}$$

The uncertainties of the quantities in Eq. 3.25 and 3.26 are:

- $w_b = w_c = \pm 0.0001m$
- $w_{V_L} = w_{V_D} = 0.001V$
- $w_{E_{ii}}$ standard deviations of the evaluation matrix of the balance are considered as uncertainty values:

$$\Sigma_E = W_E = \begin{bmatrix} 0.0019 & 0.0039 \\ 0.0024 & 0.0012 \end{bmatrix} \tag{3.27}$$

- w_ρ is evaluated from equation 3.22:

$$w_\rho = \sqrt{\left(\frac{\partial \rho}{\partial P} w_P\right)^2 + \left(\frac{\partial \rho}{\partial T} w_T\right)^2} \tag{3.28}$$

  where $w_T = 0.5K$ and $w_P = 0.1mbar$.

- w_U is evaluated from 3.24

$$w_U = \sqrt{\left(\frac{\partial U}{\partial K} w_K\right)^2 + \left(\frac{\partial U}{\partial \Delta P_{static}} w_{\Delta P_{static}}\right)^2 + \left(\frac{\partial U}{\partial \rho} w_\rho\right)^2} \tag{3.29}$$

  Where:

  - w_ρ comes from equation 3.28
  - $w_{\Delta P_{static}} = 0.25Pa$ is the $0.1\%FS$ of the pressure transducer across the nozzle.
  - w_K is found using the regression coefficient uncertainties. The regression is linear so $P_{dyn} = K\Delta P + q$ and assuming all measurements have the same uncertainty we get:

$$w_K = w_{\Delta P_{static}} \sqrt{\frac{N}{N\sum_{k=1}^{n} x_i^2 - \left(\sum_{k=1}^{n} x_i\right)^2}} \tag{3.30}$$

    Where N is the number of calibration measurements x_i.

Values of the force coefficients uncertainties in stall conditions are reported in table 3.4:

Table 3.4: Uncertainty of the force coefficients at the stall angle for the test velocities in standard atmospheric conditions.

$V_\infty(m/s)$	w_{C_L}	w_{C_D}
10	0.0069	0.0038
20	0.0052	0.0031

3.8.2 Electric power

Power is obtained through integration of the voltage and current signals over a period of the carrier sine wave, as already discussed in section 3.5. For the sake of completeness, we report in Eq. 3.31, 3.32 the expression of P in the case of exact and numerical integration with trapezoidal method:

$$P_e = \frac{1}{T}\int_0^T V(t)I(t)dt \tag{3.31}$$

$$P_e = \frac{1}{T}\sum_{j=1}^{n-1} \frac{(V_{actj}I_j + V_{actj+1}I_{j+1})\Delta t}{2} \tag{3.32}$$

Where:

- Δt is the sampling period of the acquisition
- T is the period of the carrier sine wave
- V_{actj} is the j-th component of the voltage signal acquired through the voltage divider and the oscilloscope:

  $$V_{actj} = V_j \frac{R_{in}}{R_{out}} \tag{3.33}$$

  R_{in} and R_{out} are the resistors of the voltage divider; their ratio in Eq. 3.33 is equal to $R_v = 1000$.

- I_j is the j-th component of the current signal, acquired through the voltage V_s across the shunt resistor R_s:

  $$I_j = V_{sj}/R_s \tag{3.34}$$

By substituting the previous relations in Eq. 3.32 we obtain:

$$P_e = \frac{1}{T}\sum_{j=1}^{n-1} \frac{(V_j R_v \frac{V_{sj}}{R_s} + V_{actj+1} R_v \frac{V_{sj+1}}{Rs})\Delta t}{2} \tag{3.35}$$

The uncertainty on electrical power satisfies the following equation:

$$w_{P_e} = \frac{\sqrt{\left(\frac{\partial P}{\partial \Delta t} w_{\Delta t}\right)^2 + \left(\frac{\partial P}{\partial T} w_T\right)^2 + \left(\frac{\partial P}{\partial V_j} w_{V_j}\right)^2 + \left(\frac{\partial P}{\partial V_{sj}} w_{V_{sj}}\right)^2}}{\left(\frac{\partial P}{\partial V_{j+1}} w_{V_j+1}\right)^2 + \left(\frac{\partial P}{\partial V_{sj+1]}} w_{V_{sj+1}}\right)^2 + \left(\frac{\partial P}{\partial R_v} w_{R_v}\right)^2 + \left(\frac{\partial P}{\partial R_s} w_{R_s}\right)^2} ; j = 1,...,n \tag{3.36}$$

The uncertainties of the quantities in Eq. 3.36:

- $w_{\Delta t} = \frac{\Delta t}{2}$
- $w_T = \frac{\Delta t}{2}$

- $w_{V_j} = \frac{FS_V}{2^9}$ due to the quantization error of the oscilloscope, with a full scale FS_V of the voltage channel, and an 8-bit depth signal.
- $w_{V_s} = \frac{FS_I}{2^9}$ due to the quantization error of the oscilloscope, with a full scale FS_I of the current channel, and an 8-bit depth signal.
- $w_{R_v} = 0.02R_v$ due to the voltage divider impedance.
- $w_{R_s} = 0.02R_s$ due to the uncertainty of the shunt resistor impedance.

Values of power uncertainty for actuators C1 and D17 are reported in table 3.5. These actuators are, respectively, the less and the most energy consuming of the whole set tested in this thesis. C1 power consumption is measured at 20 m/s, while D17 is independent on free stream velocity.

Table 3.5: Uncertainty of power consumption for actuators C1 at 20 m/s and D17, supplied with non-modulated sine wave at $800Hz$.

Actuator	$P_e(W)$	$w_{P_e}(W)(3\sigma)$
C1	0.68	0.06
D15	19.5	1.62

Chapter 4

Results

This chapter presents the experimental results obtained during wind tunnel testing. First, we characterized the aerodynamic performances of the NACA0015 airfoil, in order to compare all actuators with a common baseline, as well as to assess the effects of plasma actuators as passive devices. Secondly, we present the most significant results of both DBD and corona type actuators. In the final section, power consumptions and other relevant considerations are analyzed.

4.1 NACA 0015 Aerodynamics

All our results are calculated between turned-off and turned-on-actuator performances, to align with the dissertation of previous theses [58, 99, 100]. Nevertheless, we performed a preliminary study to obtain the clean aerodynamic curves of the NACA 0015 airfoil as a reference baseline for comparison as well as to quantify the effects of plasma actuators as passive devices. This was achieved by means of a C-shaped plexiglas insert (without electrodes installed), accurately fitted to the airfoil nose cavity with the aid of modelling clay. We analyzed three different freestream speeds ($10m/s$, $15m/s$ and $20m/s$),see Fig. 4.1 and 4.2.

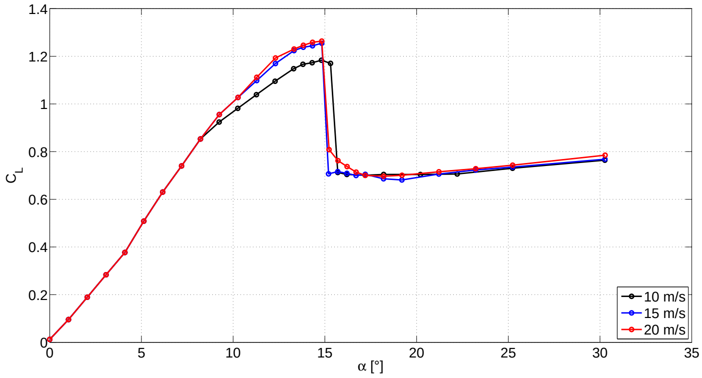

Figure 4.1: $C_L - \alpha$ curves at various speeds.

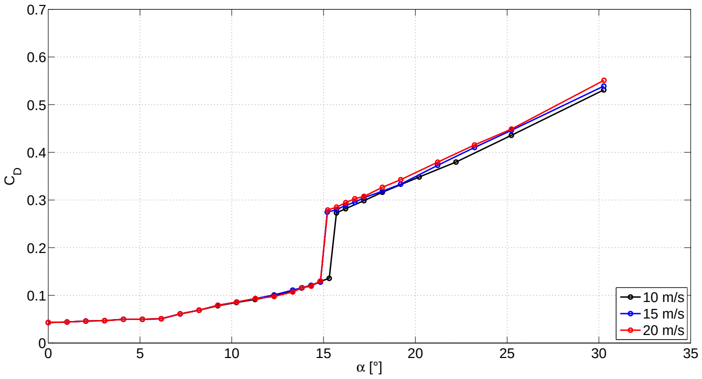

Figure 4.2: $C_D - \alpha$ curves at various speeds.

Several issues may affect the airfoil behavior, turning it away from the one of an ideal NACA 0015. First of all, due to technical limitations, the endplates are not large enough to completely prevent 3D effects at the airfoil extremities. Another aspect involving 3D effects on the real flow is the aspect ratio of the airfoil, which is limited by the test section size and by the choice of the chord of the airfoil, hence the Reynolds number. Nevertheless, our attention will be more focused on the relative performances between plasma off and plasma on. We will not further investigate 3D effects which will be present in both cases and consequently will not compromise our study, as it was done in other literature cases (see [79, 98]). Finally, the shedding frequency of the airfoil was measured by means of HWA (hot wire anemometry). Wind tunnel speed (U) was set to $20m/s$, with $alpha = 20^\circ$. The resulting frequency was around $50Hz$, which corresponds to the classical expression $f = StU/csin\alpha$, where St is the Strouhal number (≈ 0.21), and $csin\alpha$ is the projection of the chord in the direction normal to the flow.

4.2 Passive effects of plasma actuators

In this section, the behavior of the airfoil equipped with actuators as passive devices is presented. The electrodes are placed on the leading edge of the airfoil, a region which is very sensitive to geometry and roughness variation. As a result, the actuators act as manipulators, promoting boundary layer transition and changing the characteristics of lift and drag coefficients as well as critical angle position. In the case of corona actuators this effect is enhanced by the presence of the grounded electrode which is exposed to the free stream, instead of being encapsulated as for the DBD actuators. These passive effects are limited to a 10% deviation from the clean aerodynamic curve at $10m/s$ (Re = 170000) for DBD actuators, except for the case of the D3 actuator, which manifested a 20% in the post-stall range (see Fig. 4.3a and 4.3b). On the other hand, at higher Reynolds number ($20m/s$, Re = 340000), the post-critical range is strongly dependent on the particular actuator shape, as shown in Fig. 4.4a and 4.4b. The C_L drop is less prominent and shifted to larger angles of attack. Moreover, an additional local maximum appears in the $C_L - \alpha$ curve at high angles of attack. This phenomenon had already been observed in previous works [106, 107].

The different behaviour at the two test velocities is due to the reduction of boundary layer thickness at increasing free-stream velocity. The exposed electrode is made with a 0.12 mm-thick aluminium tape while the displacement thickness at 15° at the leading edge is 0.2 mm at 10m/s and 0.15 mm at 20m/s (XFOIL results). At the lowest Reynolds number, the boundary layer detachment occurs at 2% of the chord, generating a separation bubble which closes at 7% of the chord. Boundary layer is turbulent downstream of the bubble. Instead, at 20 m/s, the separation bubble is shorter, closing at 4% of the chord. At 10 m/s the bubble is longer than many of the exposed electrode tips. But actuators $D14 \div D17$ protrude further downstream where boundary layer thickness is in the order of 4 mm. At 20m/s, all actuators except D1 and D2 have tips longer than the separation bubble. Moreover, the displacement thickness after the free transition predicted by XFOIL is 0.5 mm which is comparable to the electrode thickness. For this reason, the passive influence of the tips is an expected result at this Reynolds number.

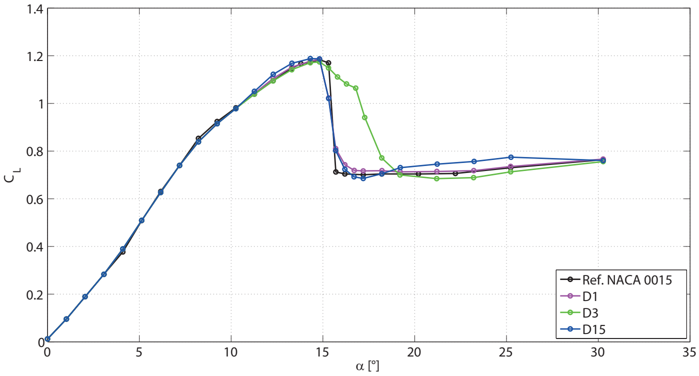

(a) $C_L - \alpha$ curves.

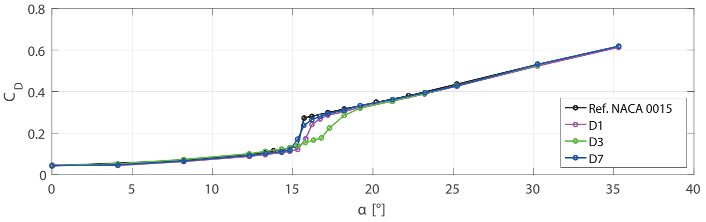

(b) $C_D - \alpha$ curves.

Figure 4.3: DBD comparison at $10m/s$.

Fig. 4.5a and 4.5b show the same comparison at $10m/s$ for corona actuators. The curves are similar to each other, except for the geometry C1, which consists of a wire-to-plate configuration. Its aerodynamic performances are reduced in pre-stall condition while in post-critical angles of attack, the drop of lift coefficient is more gentle.

At $20m/s$, the disparity between the curves is increased, especially for the wire-to-plate geometry (see Fig. 4.6a and 4.6b). As a result, the relative performances of the tested actuators are strongly affected by the passive effect of the actuator geometry.

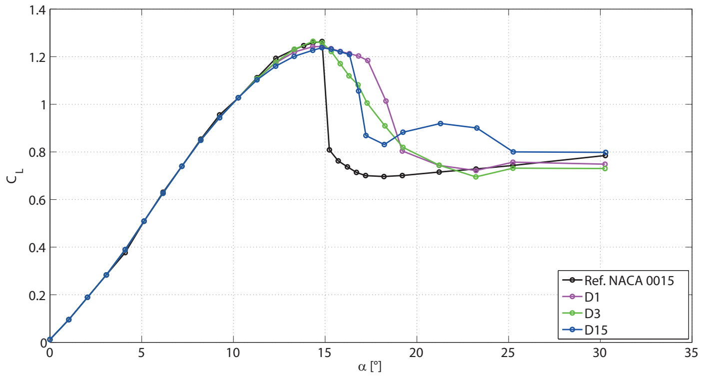

(a) $C_L - \alpha$ curves.

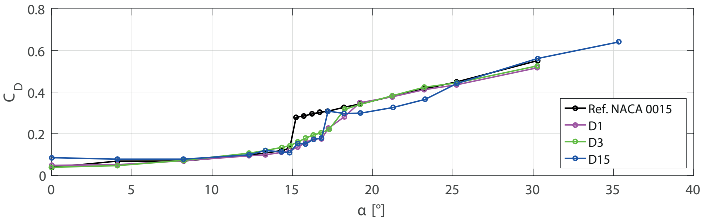

(b) $C_D - \alpha$ curves.

Figure 4.4: DBD comparison at $20m/s$.

4.3 Performance parameters

To assess the performances of plasma actuators, we introduced some parameters which will be described in the following sections. All results are calculated comparing the tests with and without plasma actuation. The curves are obtained as the average of several tests, to ensure robust results and assess repeatability.

4.3.1 Lift coefficient

As for the lift coefficient, we selected two parameters: the first one represents the percentage increase of the maximum C_L (see Fig. 4.7):

$$\Delta C_{L_{max}} \triangleq \frac{maxC_{L_{on}} - maxC_{L_{off}}}{maxC_{L_{off}}} \tag{4.1}$$

The second one is an integral parameter which represents the area enclosed between the two curves (see Fig. 4.8):

$$\Delta C_{L_{mean}} \triangleq \frac{< C_{L_{on}} > - < C_{L_{off}} >}{< C_{L_{off}} >} \tag{4.2}$$

The effectiveness of plasma actuators decreases with increasing free-stream speed. Tests performed at $20m/s$ showed a slight increase of the maximum C_L which has the same order of magnitude of the measuring error. Therefore, we could not adopt this parameter to compare the tested actuator performances at this speed.

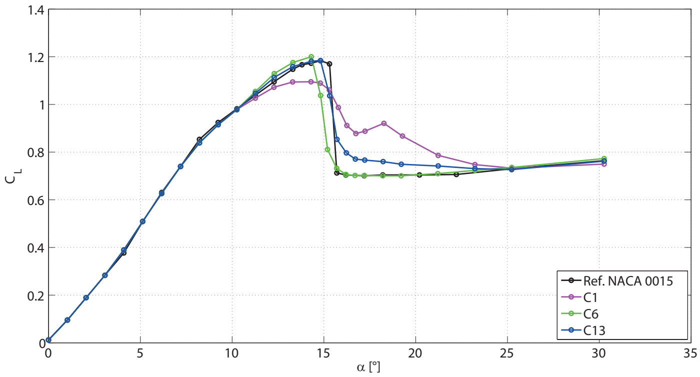

(a) $C_L - \alpha$ curves.

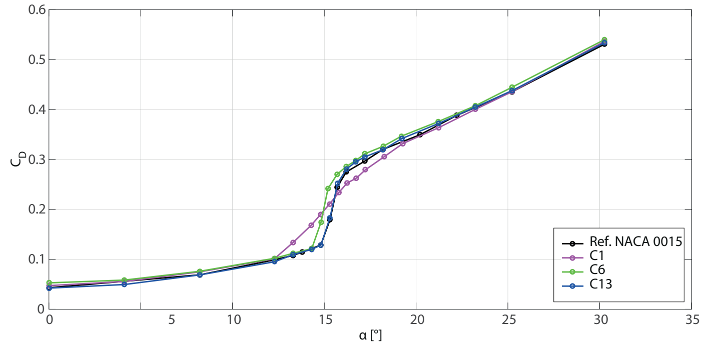

(b) $C_D - \alpha$ curves.

Figure 4.5: Corona comparison at $10m/s$.

4.3.2 Stall delay

The delay of the stall angle is directly linked to the maximum C_L:

$$\Delta\alpha_{stall} \triangleq \alpha_{stall_{on}} - \alpha_{stall_{off}} \tag{4.3}$$

This parameter is strictly related to $\Delta C_{L_{max}}$ so it is not very significant at $20m/s$. It is indeed more interesting at $10m/s$.

4.3.3 Drag coefficient

As for the drag coefficient, we adopted an integral parameter analogous to that for the lift (see Fig. 4.9):

$$\Delta C_{D_{mean}} \triangleq \frac{< C_{D_{on}} > - < C_{D_{off}} >}{< C_{D_{off}} >} \tag{4.4}$$

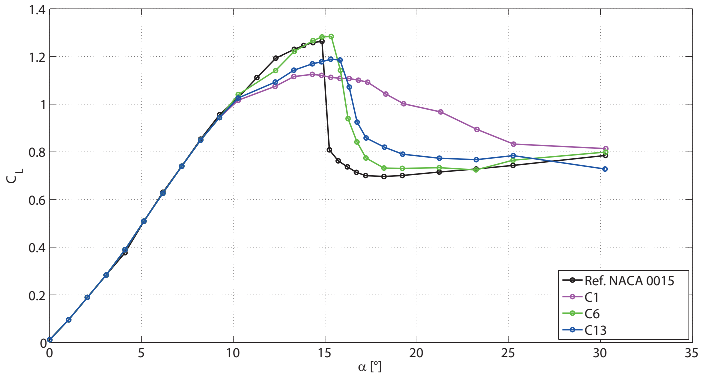

(a) $C_L - \alpha$ curves.

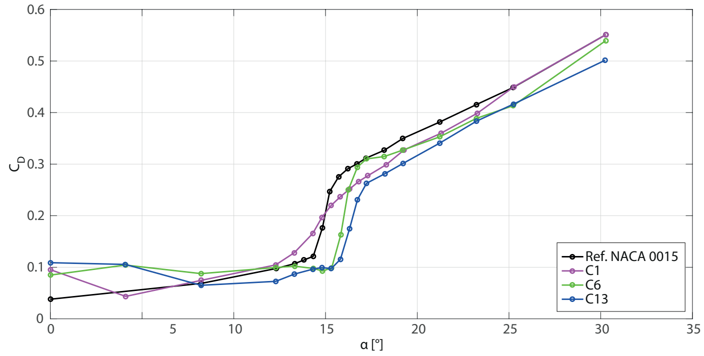

(b) $C_D - \alpha$ curves.

Figure 4.6: Corona comparison at $20m/s$.

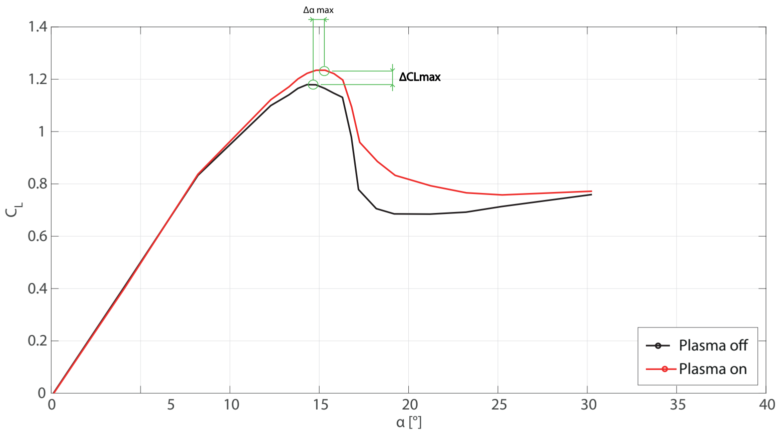

Figure 4.7: $\Delta C_{L_{max}}$ explanation.

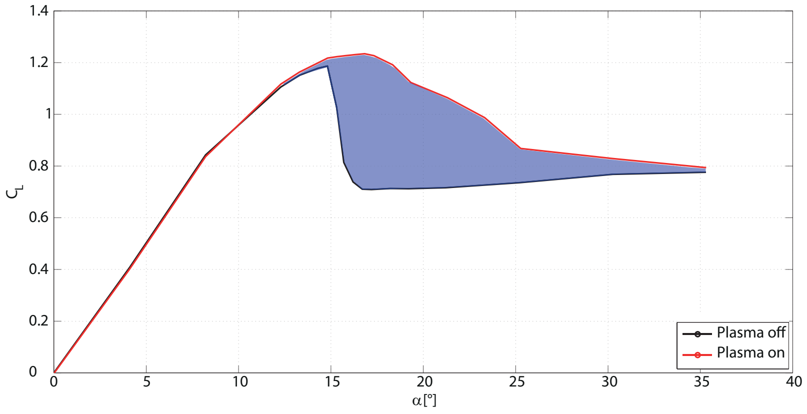

Figure 4.8: $\Delta C_{L_{mean}}$ explanation.

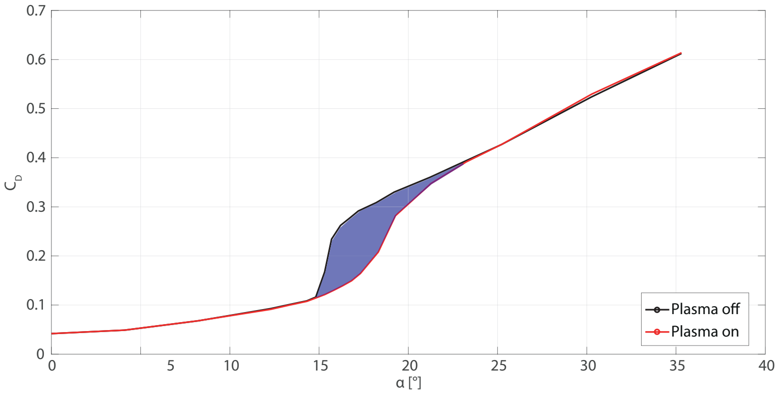

Figure 4.9: $\Delta C_{D_{mean}}$ explanation.

4.4 DBD results

In this section, results of wind tunnel experiments on DBD actuators are presented. The actuators effectiveness is estimated by means of parametric maps, where each aerodynamic performance parameter is plotted in the space of duty cycle and f^+ for both wind tunnel speeds ($10m/s$ and $20m/s$). The $C_L - \alpha$ and $C_D - \alpha$ curves of the most relevant actuators are presented along with the relative maps.

4.4.1 Tests at 10 m/s

Plasma actuation greatly enhances the aerodynamic performances of the airfoil at this free stream speed. As Fig. 4.10 shows, the maximum C_L is increased by over 7% and stall is delayed by 2 degrees (see Fig. 4.11), in the case of actuator D7, which resulted to be the best geometry. However, the effect of unsteady actuation does not seem to increase the effectiveness of the actuator at $10m/s$ (see Fig. 4.11). This is probably due to the fact that, before the post-critical range, the predominant effect is ionic wind generation, which is stronger with the steady actuation, while in the post-critical range, vortex generation is more effective. All geometries indeed manifested a similar trend, as shown in Tab. 4.1. The term “steady” refers to non-modulated actuation, corresponding to a 100% duty cycle. The maximum lift augmentation is always found in the steady case, except for the D1 actuator.

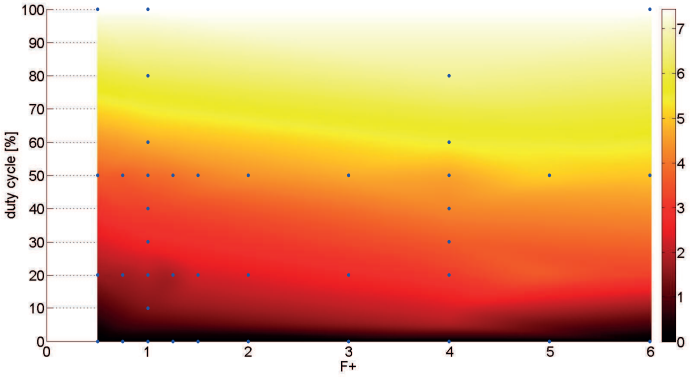

Figure 4.10: $\Delta C_{L_{max}}$ in the parameter space at $10m/s$ of actuator D7.

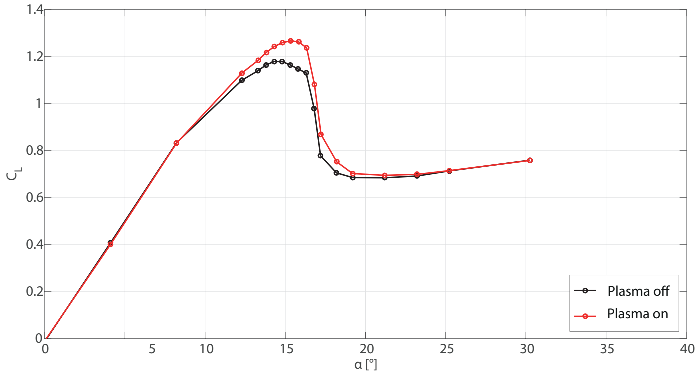

Figure 4.11: $C_L - \alpha$ curve at $10m/s$ of actuator D7, $f^+ = 1$, $DutyCycle = 100\%$.

As for the mean C_L, most of the tested geometries found an optimum around $f^+ = 1$, with duty cycles ranging from 20 to 50% (see Fig. 4.14). This confirms the result that unsteady actuation is more effective in the post-critical range, in particular when the reduced frequency is equal to one. As Fig. 4.13 shows, the maximum C_L is lower than the one achievable with 100% duty cycle, however, stall is less abrupt and the effect of plasma is appreciable even at high angles of attack.

The effect of plasma actuation on drag reduction is substantial between 15.5 and 19°, as shown in Fig. 4.15. The most performing actuator was D1, with a reduction of 12.6% (see Fig. 4.14), evaluated with the integral parameter introduced in section 4.3.3. The region around $f^+ = 4$ is the best, confirming previous results (see Sec. 4.6).

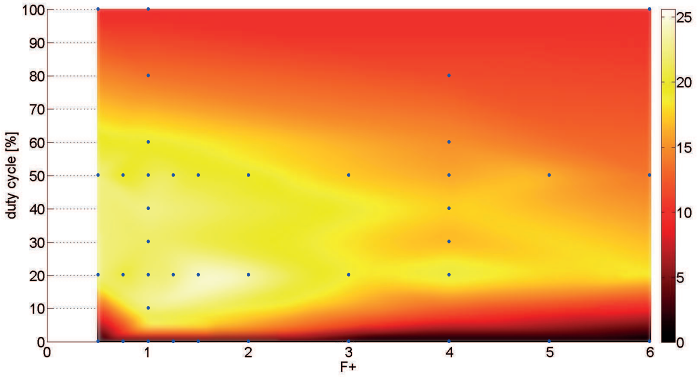

Figure 4.12: $\Delta C_{L_{mean}}$ in the parameter space at $10m/s$ of actuator D1.

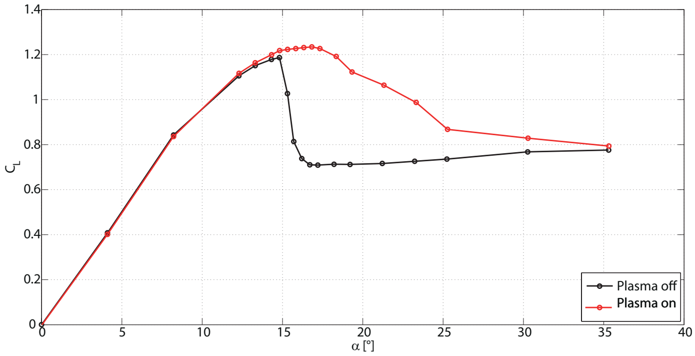

Figure 4.13: $C_L - \alpha$ curve at $10m/s$ of actuator D1, $f^+ = 2$, $DutyCycle = 20\%$.

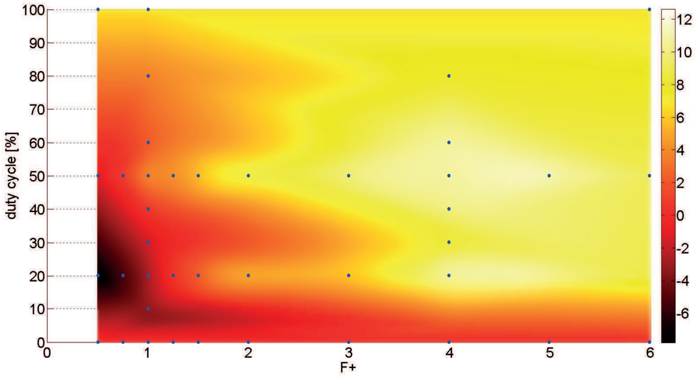

Figure 4.14: $\Delta C_{D_{mean}}$ in the parameter space at $10m/s$ of actuator D1.

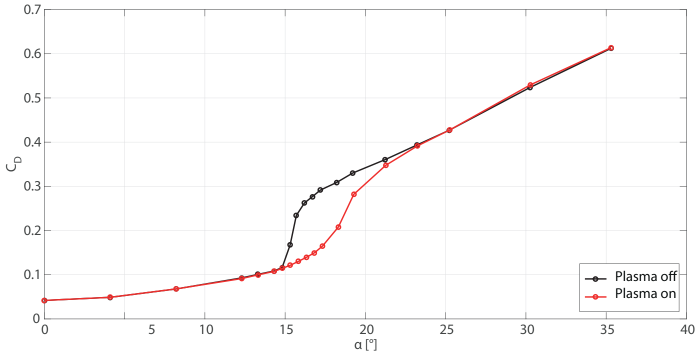

Figure 4.15: $C_D - \alpha$ curve at $10m/s$ of actuator D1, $f^+ = 5$, $DutyCycle = 20\%$.

Table 4.1: Aerodynamic performance parameters at $10m/s$.

Actuator	$\Delta C_{L_{max}}$	f^+ - D.C. (%)	$\Delta C_{L_{mean}}$	f^+ - D.C. (%)	$\Delta C_{D_{mean}}$	f^+ - D.C. (%)
D1	5.8%	1 - 50	25.6%	2 - 20	12.6%	5 - 20
D3	7%	steady	13.5%	1 - 40	7.5%	steady
D5	7.6%	steady	13.2%	1.25 - 50	4.9%	4 - 80
D7	7.4%	steady	10.2%	0.75 - 20	1.3%	steady
D14	4.5%	steady	5.4%	1 - 30	0.5%	steady
D15	7.1%	steady	17.1%	1 - 60	9.7%	steady
D16	5.9%	steady	8%	2 - 50	3.6%	2 - 50
D17	7.2%	steady	14.7%	1 - 30	3.9%	4 - 40

4.4.2 Tests at 20 m/s

The performance of the actuators is drastically reduced at $20m/s$, as can be seen in Fig. 4.17. The maximum C_L augmentation is slightly higher than the measuring error, therefore a comparison between the tested actuators is not attainable by means of this parameter. As for the integral parameter, actuator D15 stands out from the others, with a $\Delta C_{L_{mean}}$ of 17.7%, obtained with a $f^+ = 1$ at DutyCycle 30% (see Fig. 4.16). Despite of having the highest passive effect, this actuator allows a great increment of lift coefficient in the post critical region, probably attributable to vorticity generation due to plasma actuation (see Sec. 4.6). Tip separation allows a complete development of the plasma discharge (see Par. 4.4.4) which, reasonably, energizes the boundary layer more than the other actuators. This actuator was the only separated-tips DBD in our previous works. An investigation of the influence of tip separation and unsteady actuation has been performed testing three similar geometries (D14, D16, D17). Actuator D15 resulted to be the best of the four. This may be linked to the reduced power consumption of the other actuators and to the non-optimal tip separation as well.

As for drag reduction, most of the actuators showed a modest drag decrease with an $f^+ = 4$, with a D.C. of either 10% or 50%. The maximum $\Delta C_{D_{mean}}$ was found to be 4.5% for actuator D14 (see Table 4.2).

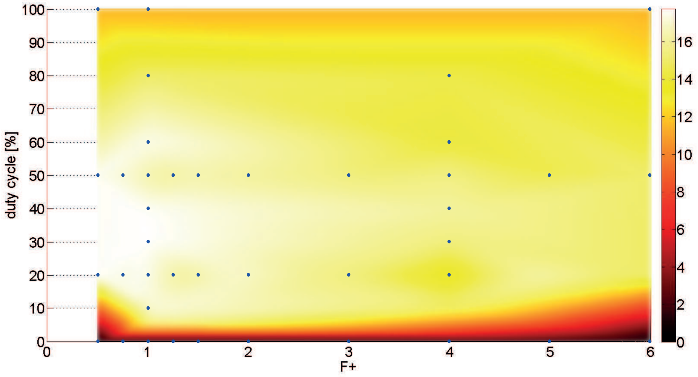

Figure 4.16: $\Delta C_{L_{mean}}$ in the parameter space at $20m/s$ of acuator D15.

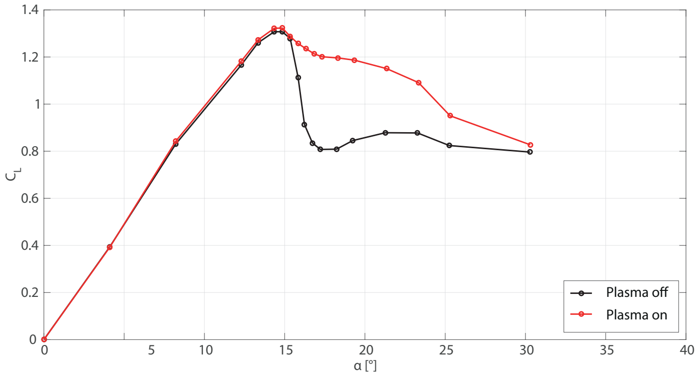

Figure 4.17: $C_L - \alpha$ curve at $20m/s$ of actuator D15, $f^+ = 1$, $DutyCycle = 30\%$.

4.4.3 Effect of the free-stream speed

The effectiveness of plasma actuators decreases with increasing free-stream speed. Moreover, as the Reynolds number is increased, even passive effects of the actuators become predominant and dramatically reduce the relative performances between the case of plasma off and plasma on. Fig. 4.19 show a comparison between two $C_L - \alpha$ curves at different free-stream speeds of the same actuator (D7). Both the maximum C_L and stall delay are greatly enhanced at $10m/s$, while the increase at $20m/s$ is small. As for the post-critical range, it can be noticed that the actuator passively influences the stall process, smoothing out the abrupt drop typical of the clean NACA 0015. As a result, the integral performance turns out to be reduced as well.

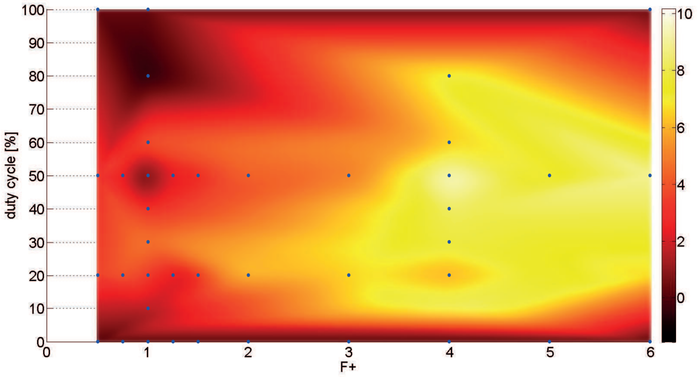

Figure 4.18: $\Delta C_{D_{mean}}$ in the parameter space at $20m/s$ of actuator D15.

Table 4.2: Aerodynamic performance parameters at $20m/s$.

Actuator	$\Delta C_{L_{mean}}$	f^+ - D.C. (%)	$\Delta C_{D_{mean}}$	f^+ - D.C. (%)
D1	6.2%	1 - 7.5	-0.7%	4 - 10
D3	2.1%	2 - 20	2.8%	steady
D5	3.9%	0.75 - 20	2.8%	6 - 50
D7	3.6%	2 - 50	-0.5%	steady
D14	6.1%	steady	4.5%	4 - 50
D15	17.7%	1 - 30	10%	4 - 50
D16	4.5%	1 - 80	2.3%	4 - 50
D17	4.2%	4 - 50	1.1%	4 - 10

4.4.4 Electrical power measurements

This section contains the electrical characterization of DBD actuators. The method adopted to measure their power consumption, the behaviour with respect to sampling frequency of voltage and current signals and effectiveness evaluation are presented. A representation of the setup for power measurements on the primary and secondary winding is shown in Fig. 4.20 and 4.21 respectively.

Electrical power of DBD actuators has been measured acquiring voltage and current signals and integrating them as follows:

$$P_e = \frac{1}{T}\int_0^T V(t)I(t)dt \tag{4.5}$$

As explained in Sec. 3.5, power has been evaluated both at the primary and secondary winding of the HV transformer. In this way, it was possible to validate the secondary winding power measurements with the primary ones, which are not affected by electro-

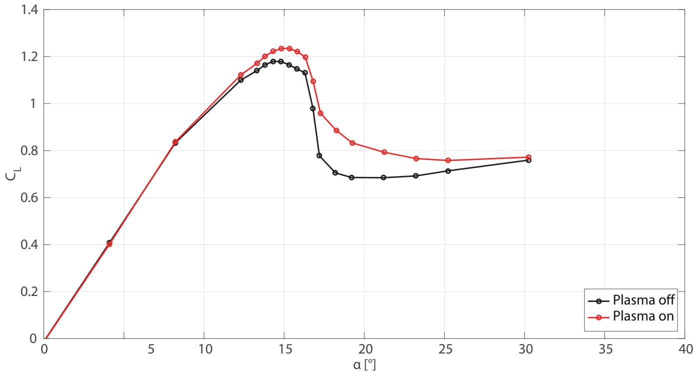

(a) $C_L - \alpha$ at $10m/s$ with $f^+ = 1$, D.C. 60%.

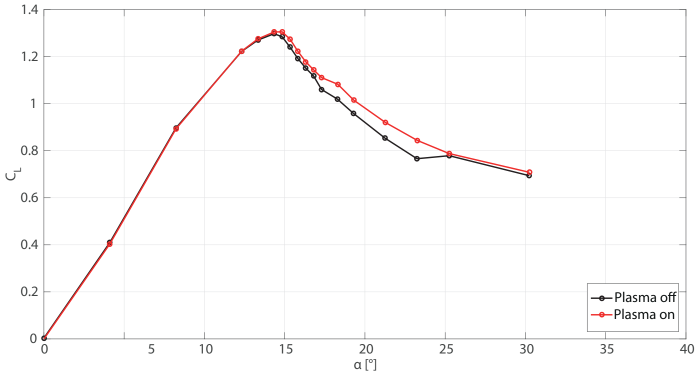

(b) $C_L - \alpha$ at $20m/s$ with $f^+ = 1$, D.C. 60%.

Figure 4.19: Comparison between $10m/s$ and $20m/s$ of actuator D7.

magnetic disturbances captured by the ground return of the actuator. For the sake of completeness, we report the expression of power in these two cases:

- Primary winding:

$$P_{prim} = \frac{1}{T}\int_0^T V_{tran}(t) I_{prim}(t) dt \tag{4.6}$$

  Where:

  $V_{tran}(t)$ is the voltage at the primary winding, after the 0.33Ω shunt resistor. $I_{prim}(t)$ is the current flowing into the shunt resistor:

$$I_{prim}(t) = \frac{V_{amp}(t) - V_{tran}(t)}{R_s} \tag{4.7}$$

- Secondary winding:

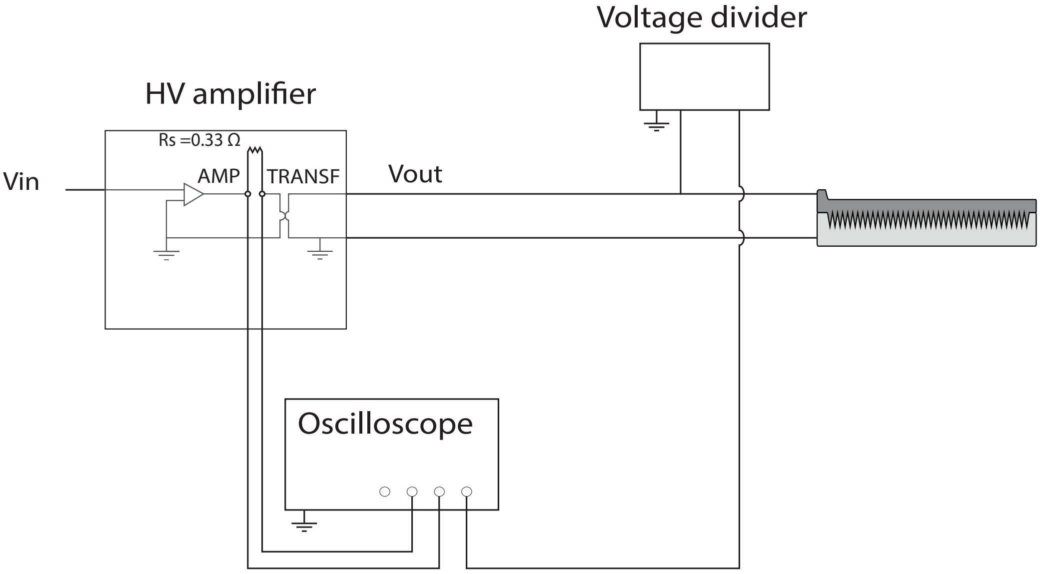

Figure 4.20: Schematic of the setup for DBD power measurements on primary winding of the HV amplifier.

$$P_{sec} = \frac{1}{T}\int_0^T V_{act}(t)I_{act}(t)dt \tag{4.8}$$

$V_{act}(t)$ is the voltage across the actuator, measured with a voltage divider. $I_{act}(t)$ is the current flowing into the actuator and the 100Ω shunt resistor.

Sampling frequency

The sampling rate for the acquisitions is $f_s = 5MS/s$. This is sufficient to resolve current on the primary winding because the signal is weakly disturbed by streamers generated by the actuator. Fig. 4.22 shows voltage and current signals on the primary winding for actuator D5. On the other hand, current on the actuator has many peaks in the positive half cycle due to streamer formation. Their characteristic frequency is in the order of $f_{streamer} \approx 10MHz$. A sampling rate of 5MS/s is not sufficient to resolve them correctly. For this reason, power measurements on the secondary winding has been taken at $5MS/s$ and $500MS/s$. Fig. 4.23, 4.24 show voltage and current time histories at the aforementioned sampling frequencies. It is worth noting the difference of the current peaks in the two figures. At $5MS/s$ (Fig. 4.23), the current peaks are around $15mA$ whereas at $500MS/s$ (Fig. 4.24), they set to $50mA$. Inevitably, in the latter case, the slow part of the current signal, which is the one that contributes to over 95% of power consumption, is not well resolved as in the former. In fact, its maximum value is approximately $5mA$, $\frac{1}{10}$ of the peak of the signal. Hence, the quantization error at $500MS/s$ is not negligible. Power consumption of DBD actuators D1, D5 and D15 at two sampling rates is shown in Tab. 4.3:

In order to assess the source of the discrepancy between the two sets of measurements, power at high sampling frequency has also been measured acquiring the current signal

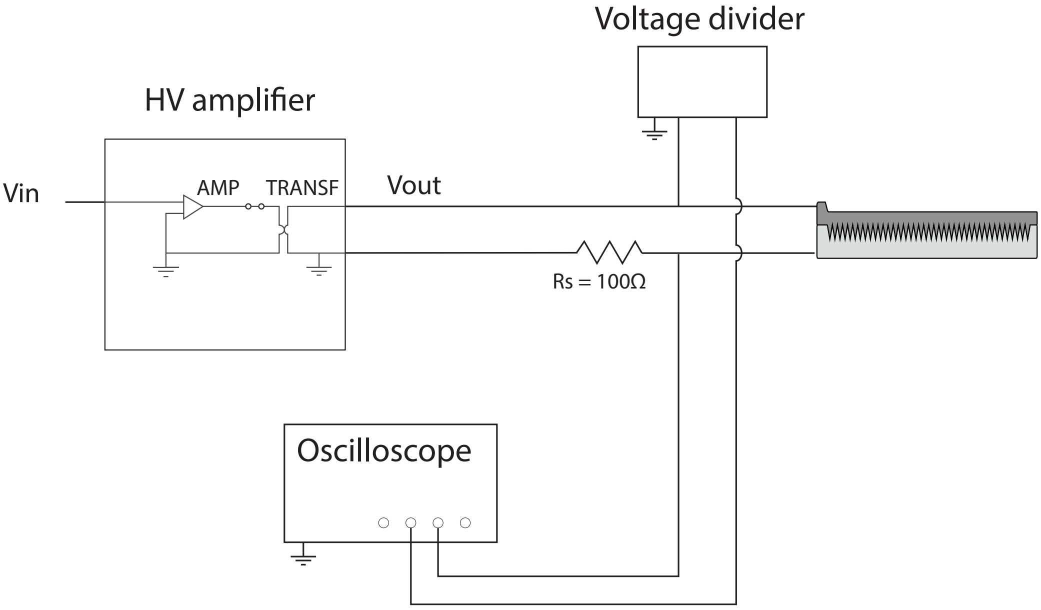

Figure 4.21: Schematic of the setup for DBD power measurements secondary winding of the HV amplifier.

Table 4.3: Comparison of electric power of DBD actuators D1, D5 and D15 at $5MS/s$ and $500MS/s$.

Actuator	$P_e(W)$ at $5MS/s$	$P_e(W)$ at $500MS/s$
D1	5.8	5.5
D5	8.2	7.6
D15	19.5	20.1

filtered with a low-pass filter. This consists of a simple RC circuit with a resistor of 68Ω and a capacitor of $100nF$. The cutoff frequency is then $f_c = \frac{1}{2\pi RC} = 23kHz$. Power measured with this setup is substantially the same as without the RC filter: $P_{efilt} = 0.97P_e$. This small difference is due to the streamer contribution.

Hence, the results at $500MS/s$ are affected by a non-negligible quantization error. Therefore, we decided to measure the electric power with a low sampling rate, in order to correctly resolve the slow part, since streamers do not give a substantial contribution to power consumption and can be underestimated.

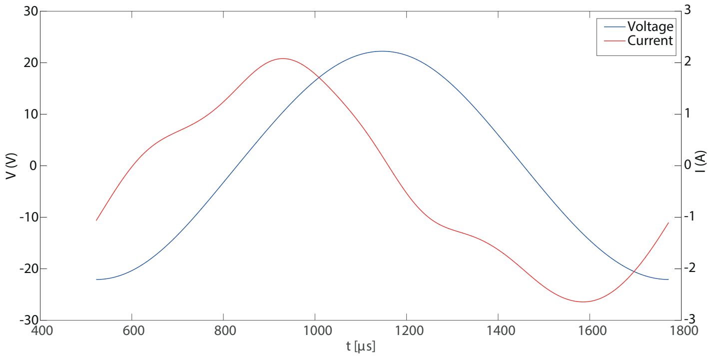

Figure 4.22: Voltage and current time histories on the primary winding for actuator D5 at 5MS/s.

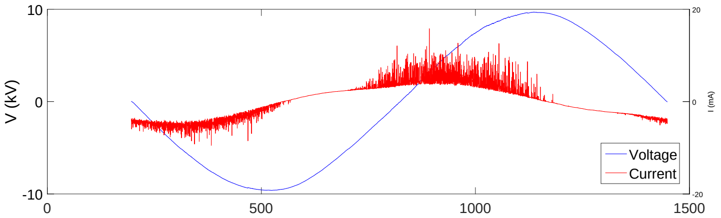

Figure 4.23: Voltage and current time histories on the secondary winding for actuator D5 at 5MS/s.

Primary and secondary winding power measurements

Power measurement on the primary winding of the HV amplifier is a good way to validate the results obtained on the secondary one. It is also possible to estimate power losses of the transformer and the high voltage line. Furthermore, the latter is a source of electromagnetic disturbances which are captured by the ground return of the actuator and by the measurement system as well. Voltage and current signals on the primary winding are not affected by these phenomena. Tab. 4.4 shows the results obtained for all DBD actuators. Power of the actuator is obtained subtracting the dissipation of the voltage divider from P_{sec}.

Efficiency, calculated as the mean of the values for each actuator, is 0.92. It does not show a dependency on power because the HV amplifier can manage a maximum power output of $100W$. All actuators require at most a fifth of this value.

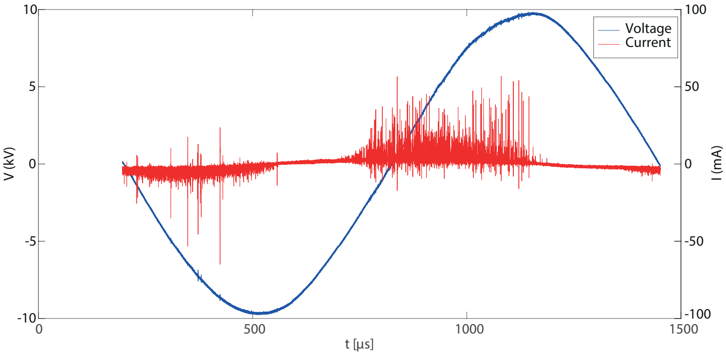

Figure 4.24: Voltage and current time histories on the secondary winding for actuator D5 at 500MS/s.

Table 4.4: Power measured on primary and secondary winding, power line efficiency

Actuator	P_{prim} (W)	P_{sec} (W)	$P_{act}(W)$	η
D1	7.75	6.77	5.79	0.87
D3	8.57	7.87	6.89	0.92
D5	9.25	9.13	8.17	0.98
D7	14.1	13.8	12.8	0.98
D14	17.7	14.5	13.5	0.82
D15	22.6	20.4	19.5	0.90
D16	20.0	18.9	17.9	0.95
D17	18.9	17.5	16.5	0.92

Duty cycle

We briefly report the dependency of DBD electric power on duty cycle. Fig. 4.25 shows the voltage signal across actuator D5 with a modulated waveform of $f = 80Hz$ and a duty cycle of 40%. After four periods of carrier, voltage theoretically goes to zero. The actual behaviour departs slightly from the ideal one because of the interaction of the transformer with the load, and of the finite values of stray capacity and inductance. This aspect is enhanced at very short duty cycles, where the linearity is lost. In spite of this fact, the voltage after the end of the pulse is in the order of 1kV, not sufficient for the actuator to turn on. For this reason, electric power of the actuators is linear with respect to the duty cycle. Fig. 4.26 shows the trend of power versus duty cycle for actuator D15.

Electrical performances

In this paragraph, electrical performances of DBD actuators will be presented. The quantities adopted to express DBD actuators performances are:

- Power per unit length: P_e/S, where $S = 400mm$ for all actuators.
- Power referred to active length: P_e/l. It is a meaningful quantity for DBDs since the entire contour of the tips takes part in plasma production [57].
- Effectiveness with respect to the mean lift increase: $\epsilon_{lm} =< \Delta L > /P_e$, where $< \Delta L >= \frac{1}{2}\rho U_\infty^2 bc\Delta CL_{mean}$. Actually this is a dimensional parameter [N/W]. The

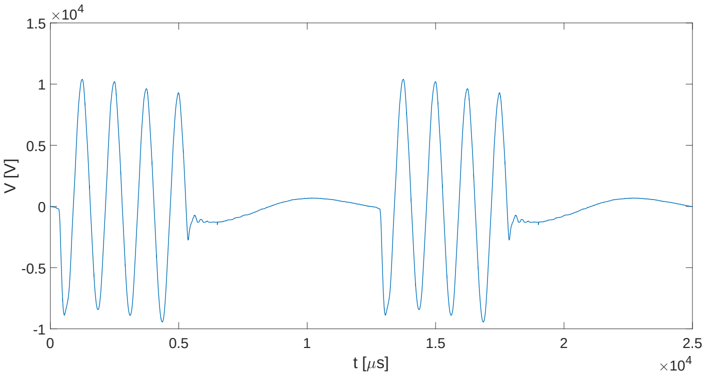

Figure 4.25: Voltage signal on actuator D5 supplied with a waveform modulated at 80Hz with 40% of duty cycle.

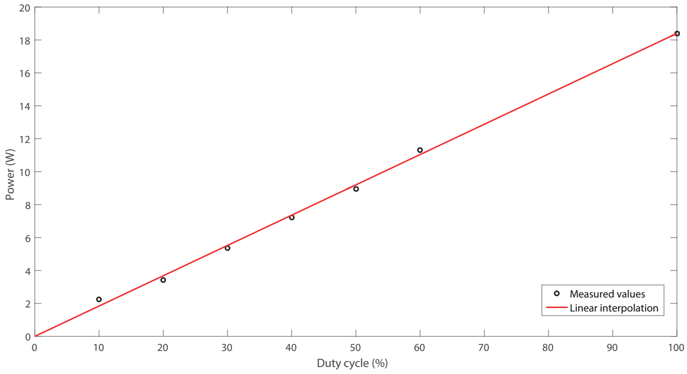

Figure 4.26: Power versus duty cycle for actuator D15.

ideal effectiveness would require the knowledge of the vertical velocity induced by the actuator, which multiplied by the lift gives the mechanical power of the actuator. This parameter will be presented for the measurements at 20m/s.

Values of P_e/S and P_e/l are reported in Tab. 4.5. Power grows with the active length of the actuator but the trend of these results also shows the dependency on tip separation. As a matter of fact, this geometrical parameter is directly related to the length of plasma discharge in the spanwise direction. If tip separation is smaller than the length of discharge, power consumption is less than that in the opposite case. This is demonstrated by the values of P_e/S for actuators D3 and D5. The active length is the same for the two cases but D5 power consumption is greater than the other due to the larger tip separation. A similar observation can be made for actuators D15, D16 and D17. Separation of the D16 is still limiting the discharge, so P_e is smaller than that of D15. Conversely tip distance of D17 is greater than the discharge length, so its power consumption is smaller than D15 and D16 due to the shorter active length. Fig. 4.27 shows the trace of dielectric material near the tips of actuators D15 D16 and D17 that ends approximately at 10 mm from the electrode edges. In Fig.4.27a there is no visible separation of the discharge deposit, while in the other two it is clearly visible a deposit-free zone between adjacent tips.

Table 4.5: Power consumption for DBD actuators.

Actuator	$P_e/S(W/m)$	$P_e/l(W/m)$
D1	14.5	14.5
D3	17.2	7.7
D5	20.4	9.1
D7	32.0	4.0
D14	33.8	4.8
D15	46.0	10.2
D16	44.8	7.8
D17	41.3	11.9

Another interesting way to evaluate actuators performances is comparing aerodynamic with electric performances. The values of ϵ_{lm} are reported in Tab. 4.6 along with the respective waveform. Actuator D1 is the one with maximum effectiveness, while D15 is the actuator with the best aerodynamic performance at 20 m/s. It should be remarked that electric power increases linearly with duty cycle.

Table 4.6: Actuator effectiveness at 20 m/s for actuators D1 and D15.

Actuator	f^+ - $D.C.(\%)$	$\epsilon_{lm}(N/W)$
D1	1 - 7.5	2.7
D15	1 - 30	0.4

It is worth noting that both duty cycles at which these performances are obtained are small. This means that pulsed actuation has the desirable effect of reducing power consumption and increasing aerodynamic performances.

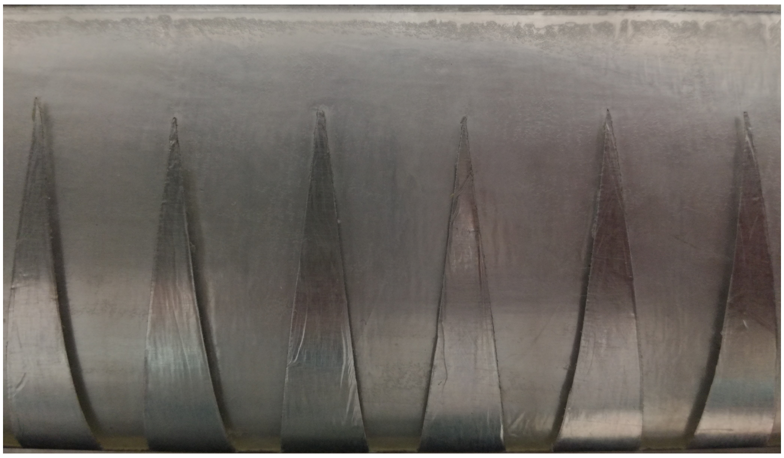

(a)

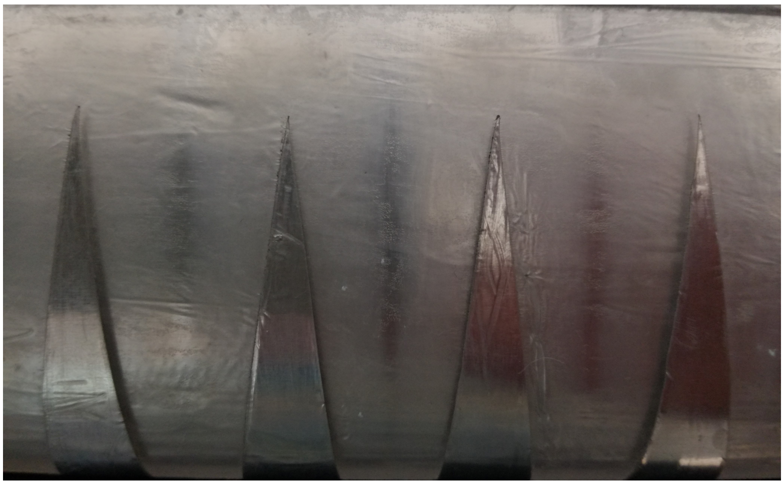

(b)

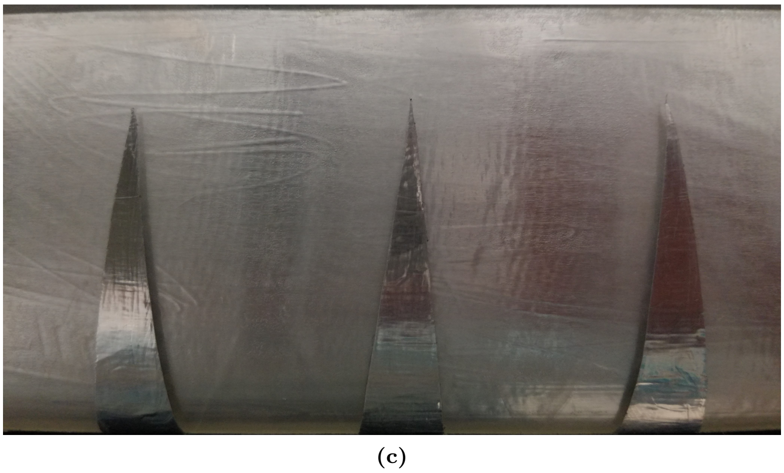

(c)

Figure 4.27: Close view of actuators D16 (a), D15 (b) and D17 (c).

4.5 Corona results

In this section, results of wind tunnel experiments on corona actuators are presented. The actuators effectiveness is estimated by means of the same parametric maps employed for DBD actuators. Only 3 geometries have been investigated, therefore it is not possible to establish a global trend.

4.5.1 Tests at 10 m/s

The performances of the three tested corona actuators at $10m/s$ resemble the DBD ones. The max lift is achieved with steady actuation, see Table 4.7, and the maximum value was obtained by actuator C6, see Fig. 4.28. Similarly to the DBD case, steady actuation allows to reach higher values of the C_L, with a stall delay of 2 degrees. However, stall occurs abruptly and the effect of the actuation is no longer appreciable in the post-critical range (see Fig. 4.29).

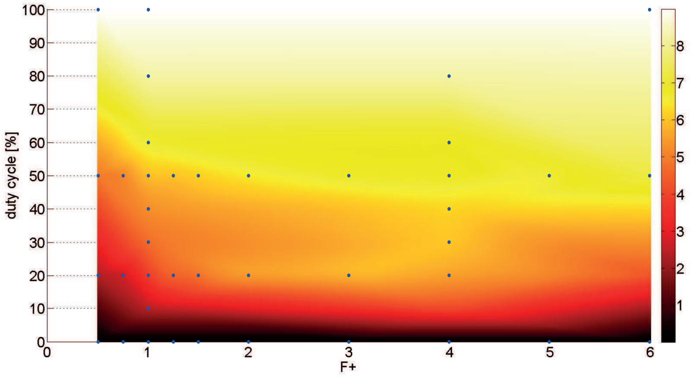

Figure 4.28: $\Delta C_{L_{max}}$ in the parameter space at $10m/s$ of actuator C6.

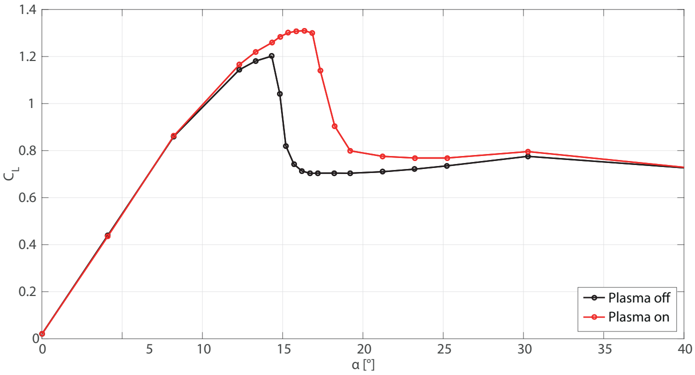

Figure 4.29: $C_L - \alpha$ curve at $10m/s$ of actuator C6, $f^+ = 1$, $DutyCycle = 100\%$.

On the contrary, pulsed actuation mostly influences the post-stall region, which results to be smoothed out (see Fig. 4.31).

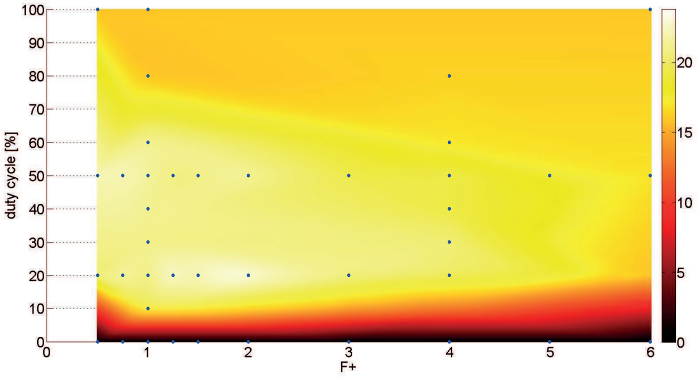

Figure 4.30: $\Delta C_{L_{mean}}$ in the parameter space at $10m/s$ of actuator C6.

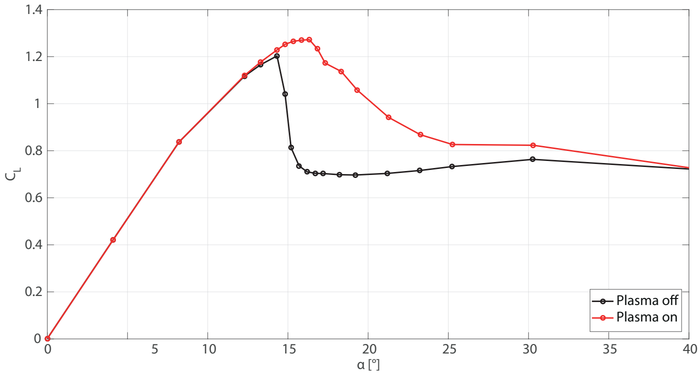

Figure 4.31: $C_L - \alpha$ curve at $10m/s$ of actuator C6, $f^+ = 2$, $DutyCycle = 20\%$.

Fig. 4.33 shows the $C_D - \alpha$ curve of actuator C6, characterized by a $C_{D_{mean}}$ reduction of 9.5% (see Fig. 4.32).

4.5.2 Tests at 20 m/s

Similarly to DBD actuators, the maximum C_L increase was not employed to assess the performances of the tested geometries at $20m/s$. As for the lift integral parameter, all actuators exhibited good results when excited with a f^+ close to unity (see Table 4.8 and Fig. 4.34). The C6 geometry reached the highest relative value of 22%, with $f^+ = 1.25$ and D.C. 20%, as shown if Fig. 4.35. Separated tips, unlike DBDs are not the best configuration. The substantial difference between DBD and corona actuators is that the latters do not interact with the flow field in the spanwise direction, instead, plasma is generated from the tips and spreads advancing towards the ground electrode.

Fig. 4.36 illustrates the mean drag reduction of actuator C13, which achieved the highest performance. A trend similar to DBD actuators can be noticed, as $f^+ = 4$ seems to be the most effective.

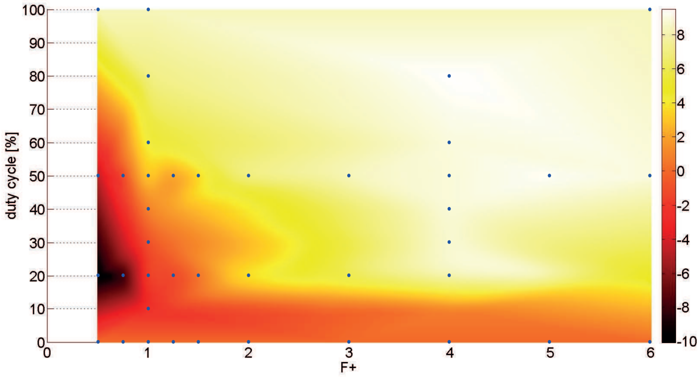

Figure 4.32: $\Delta C_{D_{mean}}$ in the parameter space at $10m/s$ of actuator C6.

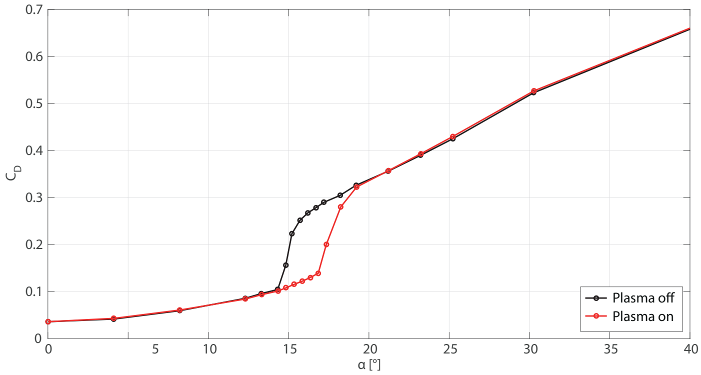

Figure 4.33: $C_D - \alpha$ curve at $10m/s$ of actuator C6, $f^+ = 4$, $DutyCycle = 80\%$.

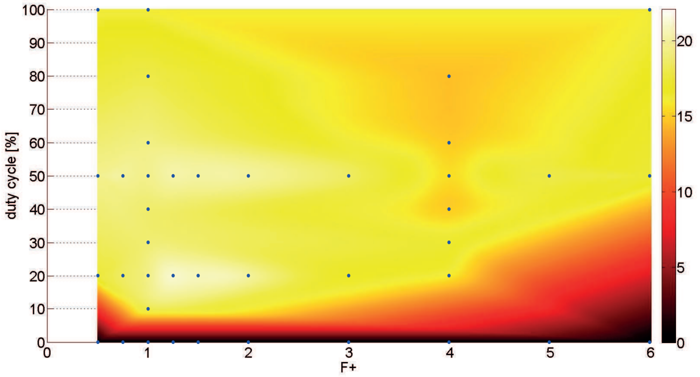

Figure 4.34: $\Delta C_{L_{mean}}$ in the parameter space at $20m/s$ of actuator C6.

Table 4.7: Aerodynamic parameter performances at $10m/s$.

Actuator	$\Delta C_{L_{max}}$	f^+ - D.C. (%)	$\Delta C_{L_{mean}}$	f^+ - D.C. (%)	$\Delta C_{D_{mean}}$	f^+ - D.C. (%)
C1	5.8%	1 - 20	12.1%	1 - 10	7.5%	4 - 80
C6	8.9%	steady	23.8%	2 - 20	9.5%	4 - 80
C13	5.8%	steady	14%	1 - 80	6.8%	5 - 50

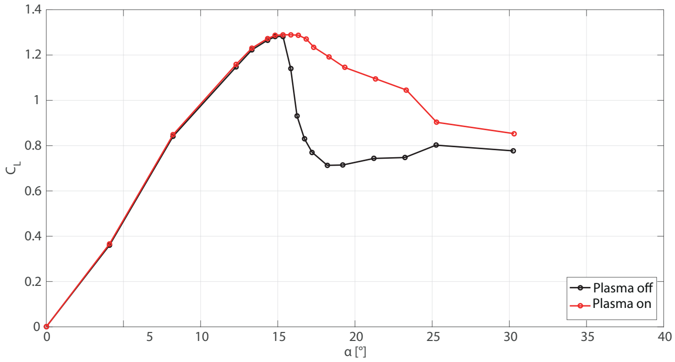

Figure 4.35: $C_L - \alpha$ curve at $20m/s$ of actuator C6, $f^+ = 1.25$, $DutyCycle = 20\%$.

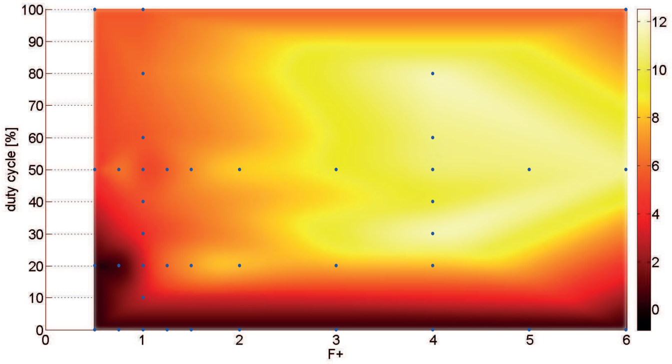

Figure 4.36: $\Delta C_{D_{mean}}$ in the parameter space at $20m/s$ of actuator C13.

4.5.3 Effect of the free-stream speed

Similarly to DBD actuators, the effectiveness of corona actuators decreases with increasing free-stream speed. Fig. 4.37 shows the comparison of actuator C13 at the two tested free-stream speeds. Both the maximum C_L and stall delay are greater at $10m/s$, while the alteration at $20m/s$ is almost negligible. As for the post-critical range, it can be noticed that unsteady actuation is more effective at $20m/s$. Stall is less abrupt with respect to the $10m/s$, thanks to the effect of plasma actuation which is still present at high angles of attack.

Table 4.8: Aerodynamic parameter performances at $20 m/s$.

Actuator	$\Delta C_{L_{mean}}$	f^{+} - D.C. (%)	$\Delta C_{D_{mean}}$	f^{+} - D.C. (%)
C1	6.2%	1 - 30	3.8%	1 - 30
C6	22.1%	1.25 - 20	11.9%	5 - 50
C13	14.1%	1.5 - 50	12.4%	4 - 30

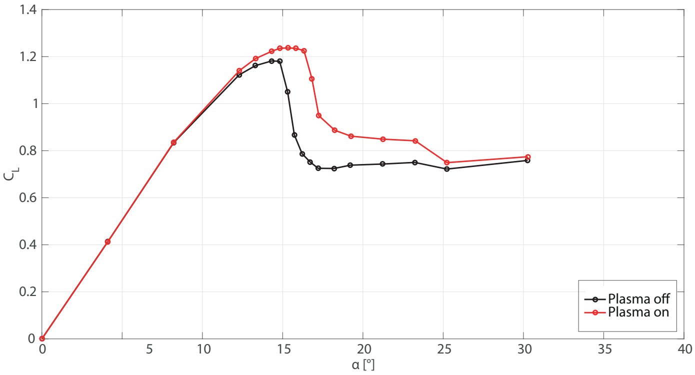

(a) $C_L - \alpha$ at $10 m/s$ with $f^{+} = 5$, D.C. 50%.

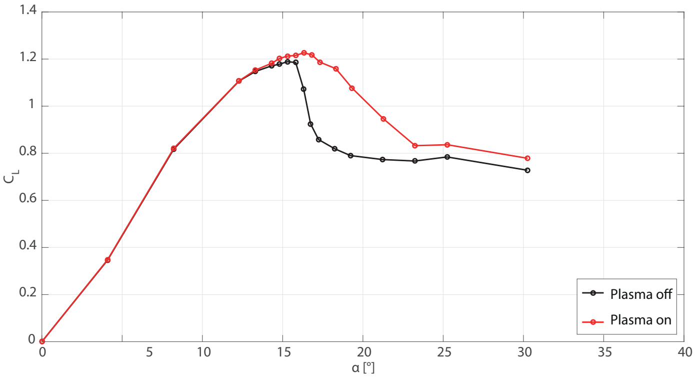

(b) $C_L - \alpha$ at $20 m/s$ with $f^{+} = 5$, D.C. 50%.

Figure 4.37: Comparison between $10 m/s$ and $20 m/s$ of actuator C13.

4.5.4 Electrical power measurements

This section shows the electrical characterization of corona actuators. The method adopted to measure their power consumption, the behaviour with respect to free stream velocity and effectiveness evaluation are presented. Power measurements of corona actuators have been performed only on the primary winding. The reason lies in two facts:

- The ratio between current peaks due to the streamers and the effective value of I is even greater than that of DBD actuators. Current peaks are in the order of $50 mA$

while $I_{RMS} = 0.3mA$ (see [99]). Current time history of a corona actuator is shown in Fig. 4.38.

- Although pulsed actuation and multi-tip geometry greatly improve the discharge stability of corona actuators, spark formation has not been completely avoided. Current peaks during a transient spark are in the order of $1A$. If current signal is acquired with the 100Ω shunt resistor on the ground return line (Fig. 4.21), the oscilloscope may be damaged permanently.

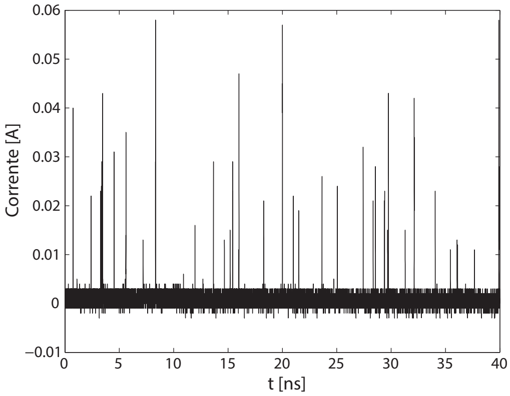

Figure 4.38: Current time history of a corona actuator, supplied with DC voltage $V = 13kV$ [99].

The setup for power measurements on corona actuators is shown in Fig. 4.39

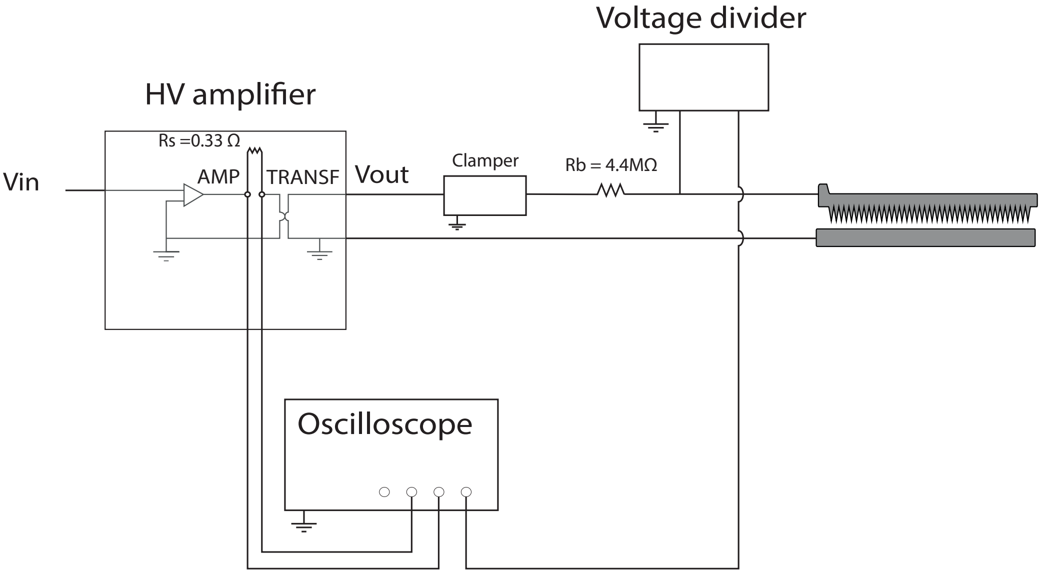

Figure 4.39: Schematic of the setup for power measurements on corona actuators.

In order to obtain the power of the actuator only, one has to measure the power dissipated by the ballast resistor R_b and the voltage divider $R_{div} = 47M\Omega$. This is accomplished by measuring the voltage output of the latter $V_{act}(t)$. Then the effective voltage is easily computed:

$$V_{RMS} = \sqrt{\frac{1}{T}\int_0^T V_{act}^2(t)dt} \tag{4.9}$$

Knowing power measured on the primary winding P_{prim} and the efficiency of the HV transformer $\eta = 0.92$, the RMS current flowing in the secondary winding I_{sec} can be computed using the following equation:

$$I_{sec} = \frac{-V_{RMS} + \sqrt{V_{RMS}^2 + 4\eta P_{prim} Rb}}{2Rb} \tag{4.10}$$

The power of the actuator is then:

$$P_{act} = \eta P_{prim} - \frac{V_{RMS}^2}{R_{div}} - R_b I_{sec}^2 \tag{4.11}$$

Fig. 4.40 shows the time history of the voltage across actuator C1 and the associated value of effective voltage along a carrier period. It may be observed that voltage drops are caused by intense streamers which partially discharge the capacity of the actuator. The relative signal, on the primary winding is shown in Fig. 4.41.

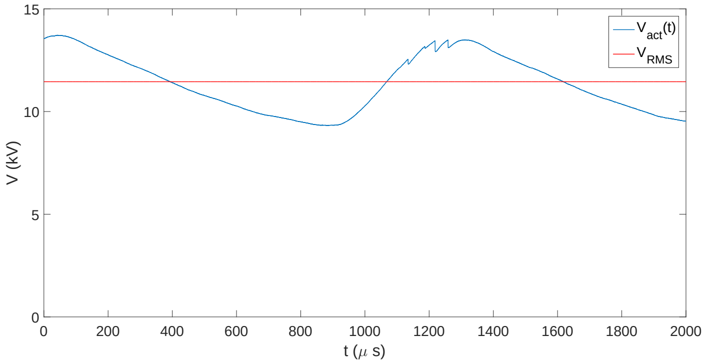

Figure 4.40: Time history of voltage across actuator C1 and relative effective value $V_{RMS} = 11.5kV$.

Free stream velocity

Unlike DBDs, corona actuators electric power depends on free-stream velocity. In [108] Moreau et al observed that discharge current increases almost linearly with asymptotic flow velocity, at fixed voltage/gap intensity (see Fig. 4.42). Consequently, an increase in power is expected. This behaviour stems from the convection of positive ions from the anode towards the cathode.

We performed power measurements with no free-stream velocity, at 10 m/s and 20 m/s, leaving input voltage unaltered setting the airfoil at an angle of attack of 13°. This angle is near to the critical conditions but separation of the boundary layer is still downstream

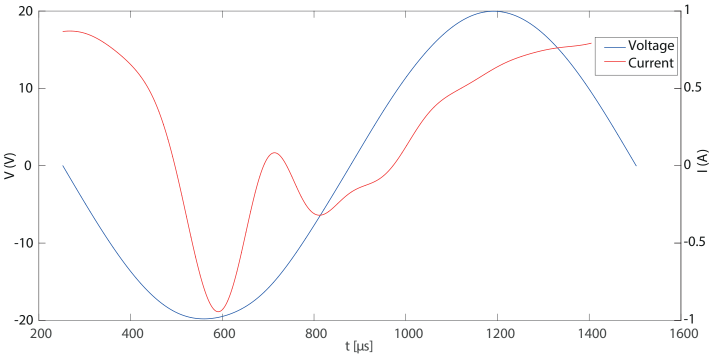

Figure 4.41: Time history of voltage and current on the primary winding of actuator C1.

the electrodes. Consequently, the actuator is working in a region where local fluid velocity is higher than free -stream speed. Results of this analysis are reported in Tab. 4.9.

Table 4.9: Power consumption versus free-stream velocity at 13° for the whole set of corona actuators.

Actuator	V_{max}	$P_e/S(W/m), U = 0m/s$	$P_e/S(W/m), U = 10m/s$	$P_e/S(W/m), U = 20m/s$
C1	13.5kV	1.4	1.2	1.7
C6	12.5kV	7.6	11.8	19.8
C13	12.4kV	2.7	3.9	6.2

The actuators have been working in the same regime. Input voltage has been set in order to reach a fully developed streamer regime, with the occasional formation of few transient sparks, without the presence of a free air stream. An external flow indeed greatly facilitates both the ignition and stabilization of surface corona discharges. Apart from actuator C1, the trend of electric power is indeed monotonically increasing.

Duty cycle

In the same fashion as for the DBDs, the trend of electric power as a function of duty cycle will be discussed in this paragraph. This is necessary to compute actuator efficiency correctly. Whereas voltage signal on DBDs goes to zero after small oscillations in the inactive part of the modulation period (see Fig. 4.25), the waveform supplied to corona actuators does not. Fig. 4.43 shows the voltage across actuator C6 with a modulated waveform at $80Hz$ and a duty cycle of 40%. Voltage after the four pulses sets around $7kV$. Further information can be obtained by observing current and voltage signals on the primary winding. Fig. 4.44 shows these signals for the same waveform as Fig. 4.43.

Current signal in Fig. 4.44 is very different from the analogous of a DBD, due to the presence of the clamper as well the different type of load of these actuators. As a matter of fact, current is negative at the beginning of the period of modulation, but voltage is close to zero. Fig. 4.45 shows the results of power measurements for actuator C6 at 20 m/s.

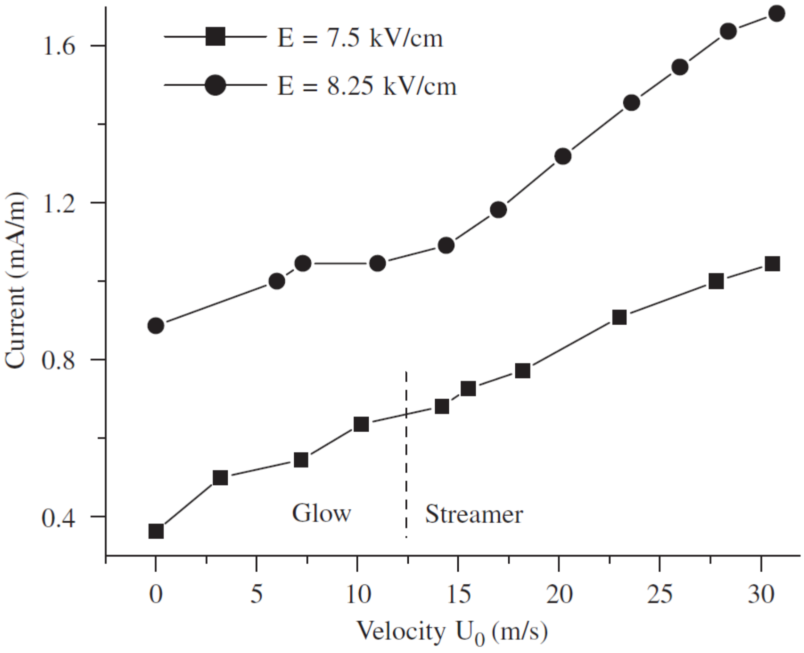

Figure 4.42: Current versus free-stream velocity for two voltage/gap ratio values [108].

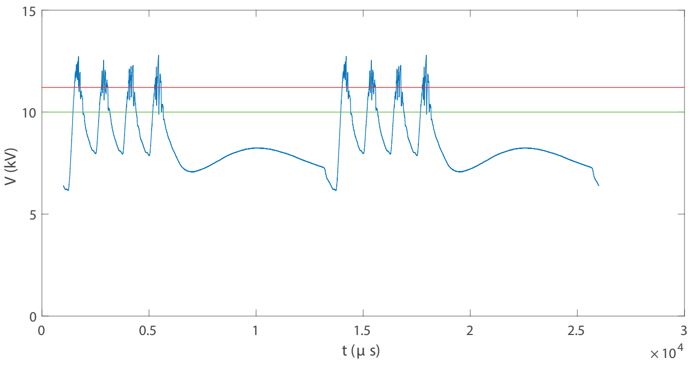

Figure 4.43: Voltage signal on actuator C6 at $20m/s$ on the secondary winding with a waveform modulated at 80Hz with 40% duty cycle (blue line), ignition voltage in still air $V_{ign} = 11.25kV$ (red line), ignition voltage at 20 m/s $V_{ign} = 10.0kV$ (green line).

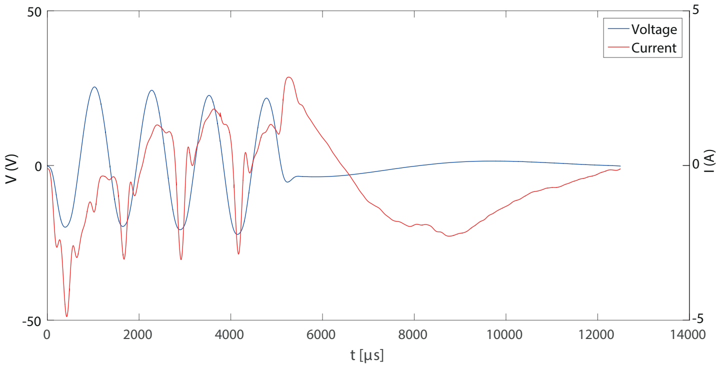

Figure 4.44: Voltage and current signals on actuator C6 at $20m/s$ on the primary winding with a waveform modulated at 80Hz with 40% of duty cycle.

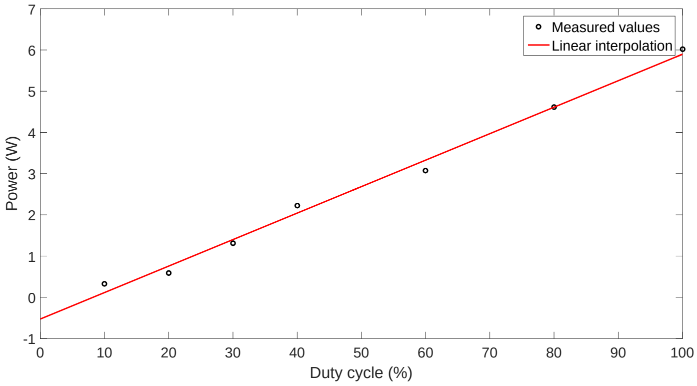

Figure 4.45: Power versus duty cycle for actuator C6 at $20m/s$.

Electrical performances

This paragraph contains the performances of the three corona actuators tested in this campaign. Results will be presented in terms of ϵ_{lm}. Power per active length will not be reported since it is not a relevant quantity for corona actuators. As a matter of fact, plasma generation occurs only in the proximity of the tips.

Tab. 4.10 and 4.11 show the maximum effectiveness of the actuators at 20 m/s and the effectiveness at $max\Delta CL_{mean}$.

Table 4.10: Maximum actuator effectiveness at 20 m/s for actuators C1, C6 and C13.

Actuator	f^+ - $D.C.(\%)$	$\epsilon_{lm}(N/W)$
C1	1 - 10	8.1
C6	1 - 10	6.1
C13	1 - 10	8.4

Table 4.11: Actuator effectiveness corresponding to $max\Delta CL_{mean}$ at 20 m/s for actuators C1, C6 and C13.

Actuator	f^+ - $D.C.(\%)$	$\epsilon_{lm}(N/W)$ at $max\Delta CL_{mean}$
C1	1 - 30	3.7
C6	1.25 - 20	3.6
C13	1.5 - 50	2.4

It's evident that corona actuators, like DBDs, have the best performances in the vicinity of $f^+ = 1$, as far as lift increase is concerned. Moreover, the effect of pulsed actuation at short duty cycles is definitely beneficial.

4.6 Comparison with literature

In this section, the outcome of this work will be compared with previous results. Although few studies on pulsed corona actuators can be found in literature (see [109–111]), the interaction between serrated electrode geometries and modulation is still a new matter. Therefore, the discourse will mainly be about DBD actuators. The database regarding NACA 0015 and pulsed DBD actuators is substantial but one should be careful to determine the conditions in which data have been acquired. The Reynolds number, the airfoil aspect ratio, endplate size, dielectric material, excitation voltage and frequency are only some of the parameters involved in these tests. The majority of the previous literature about pulsed actuations is about traditional geometries while the focus of our thesis is to couple the effect of serrated edge electrodes with unsteady excitation. The former produces streamwise vortices due to the combined effect of passive interaction with boundary layer and plasma in the spanwise direction between the tips. The latter is responsible for the production of spanwise vortices which can be efficiently exploited to interact with the aerodynamic instability in post-critical conditions. The superposition of time and space modulation is far from being trivial and it is not fathomed yet.

The best DBD actuators of our test campaign at $20m/s$ are the ones with long and separated tips. These geometries resemble the plasma vortex generators (PSVG) realized by Wicks et al in [63]. In their work, the scaling of the mean streamwise vorticity increment $\overline{\omega_x}$ induced by the PSVG in the near wall region has been determined:

$$\overline{\omega_x} \approx O\left(\frac{\Delta\overline{U}L}{\lambda\delta^*}\right) \tag{4.12}$$

Where $\Delta\overline{U}$ is the difference between induced velocity at the tip and at the valley of the electrode; L is the tip length, λ is the inter-electrode spacing (in our case coincides with the distance between tips); δ^* is the boundary layer displacement thickness upstream the electrode. After discovering that the optimal spacing is $\lambda_{opt} = \delta^*$, Wicks group demonstrated that this was just incidental and the optimal tip separation is independent from the displacement thickness. The dependency of λ_{opt} is only on electrical parameters. In our case, four different tip separation values have been tested and the best is $\lambda = 20mm$ (actuator D15).

The authors of [78] studied the effectiveness of DBD actuators to postpone the stall on a NACA0015 airfoil with a chord length of $127mm$ and $305mm$ span. The freestream velocity was set to $30m/s$, resulting in a Reynolds number of 307000, which is comparable to our tests at $20m/s$. The plasma actuators consisted of two copper electrodes separated by two layers of $0.1mm$ thick Kapton film. The actuators, placed on the leading edge, were supplied by a 11kV pp voltage, with a power consumption of about $65W/m$. Significant results were achieved using the unsteady power supply, which performed better than the steady case and allowed reduced power consumption.

In [79] the authors studied a NACA 0015 (chord length of $200mm$ and $300mm$ span) equipped with a DBD actuator. Freestream velocity is set to $20m/s$, resulting in a Reynolds numbers based on the chord length of approximately 260000. Electrodes consist of $80\mu m$ thick aluminium tape strips separated by a $3mm$ thick PMMA dielectric. Steady actuation is performed by applying a sinusoidal signal to the air-exposed electrode. In this case, the high-voltage amplitude is investigated from 12 up to $20kV$ while the frequency f_{AC} is changed from 0.5 up to $1.5kHz$. The unsteady excitation is produced by switching on and off the discharge thanks to a gate function operating at a lower frequency f_p. They confirm that the periodic excitation results in a lift enhancement and a drag reduction compared to the steady actuation. The most effective actuation is obtained for $6\% < D.C. < 50\%$ and $40\% < D.C. < 50\%$ for lift and drag, respectively. We obtained similar results at $20m/s$, as shown in Table 4.2. In particular the actuators studied in this work seem to perform better, since we find a larger ΔC_L under post-critical conditions despite the larger Reynolds number of the present tests.

Chapter 5

Conclusions and future developments

Conclusions

This thesis work allowed us to investigate the effectiveness of plasma actuators for separation control of a NACA0015 airfoil at high angles of attack for Reynolds numbers between 170000 and 340000. We focused our attention on the performances of serrated-edge geometry actuators supplied with unsteady HV actuation. In particular, we researched the optimal configuration in terms of maximum C_L increase, stall delay and electrical power consumption. Both corona and DBD actuators have been studied. Different electrode shapes have been tested with several modulated sinusoidal waveforms at duty cycles between 10% and 100%.

Wind tunnel tests confirmed previous results and theory predictions of performance degradation as the free stream speed is increased, at the same electrical and geometrical parameters. This is due to the fact that airstream power grows with the cube of the velocity, quickly overwhelming the ability of these actuators to manipulate the boundary layer flow, if electric power supplied to them is unaltered. According to these results, the scaling parameter for the performance reduction of plasma actuators is the freestream velocity, rather than the Reynolds number. This fact is supported by the result of unsteady actuation which is the most effective at $20m/s$. The classical "steady" actuation is on the other hand better at lower speeds. In the latter case, the ionic wind of plasma actuators is in the same order of free-stream speed. Its intensity is maximum in the non-pulsed actuation.

As for DBD actuators, the optimum configuration corresponds to the D15 actuator ($h = 40mm$, $w = 10mm$, $r = 4$, $n = 50$), which provides superior aerodynamic performance also compared to the basic case of plate-to-plate (D1). This actuator effectively works as a vortex generator, drawing air from the external flow to energize the boundary layer. Three similar geometries (D14, D16 and D17) have been tested to find an optimum in the tip spacing. Actuator D15 turned out to be the best of the three, since a shorter distance between tips generates small vortices unable to re-energize the boundary layer flow, while a greater distance between tips is excessive to prove useful. In this contest, electric power of the separated-tips actuators plays an important role. Actuator D14 and D16 are less energy-consuming because the discharge length is limited by the insufficient gap between the tips. Hence the aerodynamic performance is poorer than D15. On the contrary actuator D17 has an excessive tip gap which reduces the active length of the actuator, as well as the vorticity production in the streamwise direction.

The number of tested corona actuators was limited to three, therefore, a direct comparison is not straightforward. However, the C6 actuator showed the best performance in terms of C_L augmentation, while the C13 geometry resulted superior in drag reduction. The effect on unsteady actuation had the remarkable effect on facilitating the ignition process, a procedure which caused serious troubles in previous thesis works [58, 99, 100], especially for the wire-to-plate actuator. It is a novelty that such a long wire-to-plate corona actuator has been quickly ignited with good stability throughout the whole wind tunnel test. When comparing corona and DBD actuators it should be noticed that corona actuators electric power is about one order of magnitude inferior to that of DBDs. However, the aerodynamic performances of corona actuators are remarkable, despite the fact that their streamwise vorticity production is small. Actually, plasma develops only near the tips weakly spreading in the spanwise direction. Thus, ionic wind is mainly in the streamwise direction, unlike DBDs. The drawback of corona actuators, though, is their sensibility to external conditions, even if pulsed actuation has proved to make them more usable.

Future developments

A complex interaction is established when the serrated geometry is employed along with unsteady actuation. PIV analysis would greatly contribute to better understand the physical phenomenon. It would allow to characterize in a more detailed manner the flow field close to the serrated-edge actuators, when supplied with an unsteady HV actuation.

Even smoke flow visualizations could be useful to get qualitative information about the flow field around the airfoil. It would be interesting to observe the flow pattern at stall incidences as well as vortex generation. A new setup would be necessary to run these visualizations in the same wind tunnel used in this work. Due to presence of the actuators, the tracer should be made of non-aqueous insulating particles, to prevent undesired interactions with plasma.

Future experiments could be run in the De Ponte wind tunnel. This closed circuit wind tunnel, situated in the same laboratory, has a significantly larger test section and is able to reach higher speeds compared to the one used in this work. In this way, Reynolds numbers of aeronautical interest ($Re > 10^6$) would be achieved, of course by scaling the supply voltage and the other parameters of interest. To perform this task, it would be necessary to design a more advanced power supply for plasma actuators, capable of providing higher voltages at a wide frequency range.

Multiple actuators installed at different location on the airfoil chord can be used to increase aerodynamic performances before stall. Alternatively, the combined effects of corona and DBD actuators could be investigated by means of sliding discharge actuators.

Finally, numerical simulations could provide additional information of the underlying phenomena. Plasma actuation can be modelled as a body force. The challenge is to reproduce the actual trend of the electric-wind-induced force with respect to wall distance. Considering the non-negligible tridimensional effect of DBD actuators, the correct modelling of the phenomenon is far from trivial.

Bibliography

[1] P K Chang. Control of flow separation: Energy conservation, operational efficiency, and safety. *NASA STI/Recon Technical Report A*, 77, 1976.

[2] GV Lachmann. Boundary layer and flow control,(1961).

[3] D McCormick. Boundary layer separation control with directed synthetic jets. In *38th Aerospace Sciences Meeting and Exhibit*, page 519, 2000.

[4] A Seifert and LG Pack. Oscillatory control of separation at high reynolds numbers. *AIAA journal*, 37(9):1062–1071, 1999.

[5] A Seifert, S Eliahu, D Greenblatt, and I Wygnanski. Use of piezoelectric actuators for airfoil separation control. *AIAA journal*, 36(8):1535–1537, 1998.

[6] I Wygnanski and A Seifert. The control of separation by periodic oscillations. In *25th Plasmadynamics and Lasers Conference*, page 2608, 1994.

[7] L Löfdahl and M Gad-el Hak. Mems applications in turbulence and flow control. *Progress in Aerospace Sciences*, 35(2):101–203, 1999.

[8] G Godard and M Stanislas. Control of a decelerating boundary layer. part 1: Optimization of passive vortex generators. *Aerospace Science and Technology*, 10(3):181–191, 2006.

[9] E Coustols and AM Savill. Turbulent skin-friction drag reduction by active and passive means. Technical report, DTIC Document, 1992.

[10] E Coustols. Riblets: main known and unknown features. *Emerging techniques in drag reduction. Mechanical Engineering Publications, UK*, pages 3–43, 1996.

[11] MJ Walsh. Riblets, viscous drag reduction in boundary layers: progress in astronautics and aeronautics. 1990.

[12] PR Viswanath. Aircraft viscous drag reduction using riblets. *Progress in Aerospace Sciences*, 38(6):571–600, 2002.

[13] M Quadrio. Drag reduction in turbulent boundary layers by in-plane wall motion. *Philosophical transactions of the Royal Society*, 369, 2011.

[14] JP Robert. Special course on skin friction drag reduction. *Drag Reduction: An Industrial Challenge, AGARD*, pages 2–1, 1992.

[15] J L Lumley. Drag reduction in two phase and polymer flows. *The Physics of Fluids*, 20(10):S64–S71, 1977.

[16] S Grundmann and C Tropea. Active cancellation of artificially introduced tollmien–schlichting waves using plasma actuators. *Experiments in Fluids*, 44(5):795–806, 2008.

[17] E Spong and J A Reizes. Efficiency improvements of electromagnetic flow control. In *ICHMT DIGITAL LIBRARY ONLINE*. Begel House Inc., 2004.

[18] Y Sung, W Kim, MG Mungal, and MA Cappelli. Aerodynamic modification of flow over bluff objects by plasma actuation. *Experiments in fluids*, 41(3):479–486, 2006.

[19] F O Thomas, A Kozlov, and TC Corke. Plasma actuators for cylinder flow control and noise reduction. *AIAA journal*, 46(8):1921–1931, 2008.

[20] D Greenblatt, M Schulman, and A Ben-Harav. Vertical axis wind turbine performance enhancement using plasma actuators. *Renewable Energy*, 37(1):345–354, 2012.

[21] R Nelson, T Corke, H Othman, M Patel, S Vasudevan, and T Ng. A smart wind turbine blade using distributed plasma actuators for improved performance. In *46th AIAA Aerospace Sciences Meeting and Exhibit*, page 1312, 2008.

[22] R Van Dyken, T McLaughlin, and CL Enloe. Parametric investigations of a single dielectric barrier plasma actuator. In *42nd AIAA Aerospace Sciences Meeting and Exhibit*, page 846, 2004.

[23] S Grundmann, M Frey, and C Tropea. Unmanned aerial vehicle (uav) with plasma actuators for separation control. In *47th AIAA Aerospace Sciences Meeting including The New Horizons Forum and Aerospace Exposition*, page 698, 2009.

[24] P.F. Zhang, J.J. Wang, L.H. Feng, and G.B. Wang. Experimental study of plasma flow control on highly swept delta wing. *AIAA Journal*, 48:4, 2010.

[25] M Post and T Corke. Separation control using plasma actuators-stationary & oscillating airfoils. In *42nd AIAA Aerospace Sciences Meeting and Exhibit*, page 841, 2004.

[26] M Post and T Corke. Separation control using plasma actuators: dynamic stall vortex control on oscillating airfoil. *AIAA journal*, 44(12):3125–3135, 2006.

[27] J Jolibois, M Forte, and E Moreau. Application of an ac barrier discharge actuator to control airflow separation above a naca 0015 airfoil: optimization of the actuation location along the chord. *Journal of Electrostatics*, 66(9):496–503, 2008.

[28] R Sosa and G Artana. Steady control of laminar separation over airfoils with plasma sheet actuators. *Journal of Electrostatics*, 64(7):604–610, 2006.

[29] J Little and M Samimy. High-lift airfoil separation with dielectric barrier discharge plasma actuation. *AIAA journal*, 48(12):2884–2898, 2010.

[30] D M Schatzman and F O Thomas. Turbulent boundary-layer separation control with single dielectric barrier discharge plasma actuators. *AIAA journal*, 48(8):1620–1634, 2010.

[31] S Grundmann and C Tropea. Experimental damping of boundary-layer oscillations using dbd plasma actuators. *International Journal of Heat and Fluid Flow*, 30(3):394–402, 2009.

[32] V Boucinha, P Magnier, R Weber, A Leroy-Chesneau, B Dong, D Hong, and R Joussot. Characterization of the ionic wind induced by a sine dbd actuator used for laminar-to-turbulent transition delay. In *4th flow control conference*, page 4210, 2008.

[33] E Moreau. Airflow control by non-thermal plasma actuators. *Journal of Physics D: Applied Physics*, 40(3):605, 2007.

[34] A Schutze, J Y Jeong, S E Babayan, J Park, G S Selwyn, and R F Hicks. The atmospheric-pressure plasma jet: a review and comparison to other plasma sources. *IEEE transactions on plasma science*, 26(6):1685–1694, 1998.

[35] LB Loeb. *Electrical coronas, their basic physical mechanisms.* Univ of California Press, 1965.

[36] A Fridman, A Chirokov, and A Gutsol. Non-thermal atmospheric pressure discharges. *Journal of Physics D: Applied Physics*, 38(2):R1, 2005.

[37] JR Roth. *Industrial Plasma Engineering. Volume 1: Principles.* Institute of Physics Publishing, 1995.

[38] JR Roth. *Industrial Plasma Engineering: applications to nonthermal plasma processing. Vol. 2*, volume 2. CRC Press, 2002.

[39] M Goldman and RS Sigmond. Corona and insulation. *IEEE Transactions on Electrical Insulation*, (2):90–105, 1982.

[40] M Robinson. Movement of air in the electric wind of the corona discharge. *Transactions of the American Institute of Electrical Engineers, Part I: Communication and Electronics*, 80(2):143–150, 1961.

[41] RS Sigmond and IH Lagstad. Mass and species transport in corona discharges. *High Temp. Chem. Processes*, 2(4):5, 1993.

[42] CF Gallo. Corona-a brief status report. *IEEE Transactions on Industry Applications*, (6):550–557, 1977.

[43] Moreau E. *Application des plasma non thermiques au controle électrofluidodynamique des écoulement.* PhD thesis, Université de Poitiers, France, 2004.

[44] L Léger, E Moreau, and G Touchard. Effect of a dc corona electrical discharge on the airflow along a flat plate. *IEEE Transactions on Industry Applications*, 38(6):1478–1485, 2002.

[45] J Roth, D Sherman, and S Wilkinson. Boundary layer flow control with a one atmosphere uniform glow discharge surface plasma. In *36th AIAA Aerospace Sciences Meeting and Exhibit*, page 328, 1998.

[46] J R Roth, D M Sherman, and S P Wilkinson. Electrohydrodynamic flow control with a glow-discharge surface plasma. *AIAA journal*, 38(7):1166–1172, 2000.

[47] N Benard, P Noté, M Caron, and E Moreau. Highly time-resolved investigation of the electric wind caused by surface dbd at various ac frequencies. *Journal of Electrostatics*, 2017.

[48] CL Enloe, Th E McLaughlin, R D Van Dyken, KD Kachner, E J Jumper, and T C Corke. Mechanisms and responses of a single dielectric barrier plasma actuator: plasma morphology. *AIAA journal*, 42(3):589–594, 2004.

[49] N Benard, A Mizuno, and E Moreau. A large-scale multiple dielectric barrier discharge actuator based on an innovative three-electrode design. *Journal of Physics D: Applied Physics*, 42(23):235204, 2009.

[50] J Kriegseis, B Möller, S Grundmann, and C Tropea. Capacitance and power consumption quantification of dielectric barrier discharge (dbd) plasma actuators. *Journal of Electrostatics*, 69:302–312, 2011.

[51] J Pons, E Moreau, and G Touchard. Asymmetric surface dielectric barrier discharge in air at atmospheric pressure: electrical properties and induced airflow characteristics. *Journal of Physics D: Applied Physics*, 38(19):3635, 2005.

[52] R Rivir, A White, C Carter, and B Ganguly. Ac and pulsed plasma flow control. In *42nd AIAA Aerospace Sciences Meeting and Exhibit*, page 847, 2004.

[53] A Seraudie, E Aubert, N Naudé, and J Cambronne. Effect of plasma actuators on a flat plate laminar boundary layer in subsonic conditions. In *3rd AIAA Flow Control Conference*, page 3350, 2006.

[54] JP Murphy, J Kriegseis, and P Lavoie. Scaling of maximum velocity, body force, and power consumption of dielectric barrier discharge plasma actuators via particle image velocimetry. *Journal of Applied Physics*, 113(24):243301, 2013.

[55] F O Thomas, T C Corke, M Iqbal, A Kozlov, and D Schatzman. Optimization of dielectric barrier discharge plasma actuators for active aerodynamic flow control. *AIAA journal*, 47(9):2169–2178, 2009.

[56] R Joussot, A Leroy, R Weber, H Rabat, S Loyer, and D Hong. Plasma morphology and induced airflow characterization of a dbd actuator with serrated electrode. *Journal of Physics D: Applied Physics*, 46(12):125204, 2013.

[57] M Belan and F Messanelli. Compared ionic wind measurements on multi-tip corona and dbd plasma actuators. *Journal of Electrostatics*, 76:278–287, 2015.

[58] M Modugno and A Mulone. Ottimizzazione geometrica di attuatori al plasma: caratterizzazione al banco e prove in galleria del vento. Master's thesis, DAST Politecnico di Milano, 2015.

[59] RJ Durscher and S Roy. Three-dimensional flow measurements induced from serpentine plasma actuators in quiescent air. *Journal of Physics D: Applied Physics*, 45(3):035202, 2012.

[60] M Riherd and S Roy. Serpentine geometry plasma actuators for flow control. *Journal of applied physics*, 114(8):083303, 2013.

[61] S Roy, P Zhao, A DasGupta, and J Soni. Dielectric barrier discharge actuator for vehicle drag reduction at highway speeds. *AIP Advances*, 6(2):025322, 2016.

[62] T N Jukes and K S Choi. On the formation of streamwise vortices by plasma vortex generators. *Journal of Fluid Mechanics*, 733:370–393, 2013.

[63] M Wicks, F O Thomas, T C Corke, M Patel, and A B Cain. Mechanism of vorticity generation in plasma streamwise vortex generators. *AIAA Journal*, 53(11):3404–3413, 2015.

[64] M Wicks, F Thomas, D Schatzman, P Bowles, T Corke, M Patel, and A Cain. A parametric investigation of plasma streamwise vortex generator performance. In *50th AIAA Aerospace Sciences Meeting including the New Horizons Forum and Aerospace Exposition*, page 824, 2012.

[65] T N Jukes and K S Choi. Dielectric-barrier-discharge vortex generators: characterisation and optimisation for flow separation control. *Experiments in fluids*, 52(2):329–345, 2012.

[66] S Grundmann, EL Sayles, and JK Eaton. Sensitivity of an asymmetric 3d diffuser to plasma-actuator induced inlet condition perturbations. *Experiments in Fluids*, 50(1):217–231, 2011.

[67] S Grundmann, EL Sayles, Christopher J Elkins, and JK Eaton. Sensitivity of an asymmetric 3d diffuser to vortex-generator induced inlet condition perturbations. *Experiments in fluids*, 52(1):11–21, 2012.

[68] T C Corke, C L Enloe, and S P Wilkinson. Dielectric barrier discharge plasma actuators for flow control. *Annual review of fluid mechanics*, 42:505–529, 2010.

[69] N Balcon, N Benard, Y Lagmich, J-P Boeuf, G Touchard, and E Moreau. Positive and negative sawtooth signals applied to a dbd plasma actuator–influence on the electric wind. *Journal of electrostatics*, 67(2):140–145, 2009.

[70] N Benard, N Balcon, and E Moreau. Electric wind produced by a surface dielectric barrier discharge operating in air at different pressures: aeronautical control insights. *Journal of Physics D: Applied Physics*, 41(4):042002, 2008.

[71] R Anderson and S Roy. Preliminary experiments of barrier discharge plasma actuators using dry and humid air. In *44th AIAA Aerospace Sciences Meeting and Exhibit*, page 369, 2006.

[72] N Benard, N Balcon, and E Moreau. Electric wind produced by a surface dielectric barrier discharge operating over a wide range of relative humidity. In *47th AIAA Aerospace Sciences Meeting including the New Horizons Forum and Aerospace Exposition*, page 488, 2009.

[73] M Wicks and F O Thomas. Effect of relative humidity on dielectric barrier discharge plasma actuator body force. *AIAA Journal*, 53(9):2801–2805, 2015.

[74] R Erfani, H Zare-Behtash, and K Kontis. Plasma actuator: influence of dielectric surface temperature. *Experimental Thermal and Fluid Science*, 42:258–264, 2012.

[75] P Versailles, V Gingras-Gosselin, and H D Vo. Impact of pressure and temperature on the performance of plasma actuators. *AIAA journal*, 48(4):859–863, 2010.

[76] J Kriegseis, S Grundmann, and C Tropea. Airflow influence on the discharge performance of dielectric barrier discharge plasma actuators. *Physics of Plasmas*, 19(7):073509, 2012.

[77] S Pavon, JL Dorier, Ch Hollenstein, P Ott, and P Leyland. Effects of high-speed airflows on a surface dielectric barrier discharge. *Journal of Physics D: Applied Physics*, 40(6):1733, 2007.

[78] C He, T C Corke, and M P Patel. Plasma flaps and slats: an application of weakly ionized plasma actuators. *Journal of Aircraft*, 46(3):864–873, 2009.

[79] N Bénard, J Jolibois, and E Moreau. Lift and drag performances of an axisymmetric airfoil controlled by plasma actuator. *Journal of Electrostatics*, 67(2):133–139, 2009.

[80] T N Jukes and K S Choi. Flow control around a circular cylinder using pulsed dielectric barrier discharge surface plasma. *Physics of Fluids*, 21(8):084103, 2009.

[81] H Do, W Kim, M A Cappelli, and M G Mungal. Cross-talk in multiple dielectric barrier discharge actuators. *Applied Physics Letters*, 92, 2008.

[82] A Debien, N Benard, and E Moreau. Electric wind produced by sliding discharges. *Proceeding of 2nd ISNPEDADM new electrical technologies for environment, Nouméa*, 2011.

[83] C Louste, G Artana, E Moreau, and G Touchard. Sliding discharge in air at atmospheric pressure: electrical properties. *Journal of Electrostatics*, 63(6):615–620, 2005.

[84] E Moreau, C Louste, and G Touchard. Electric wind induced by sliding discharge in air at atmospheric pressure. *Journal of Electrostatics*, 66(1):107–114, 2008.

[85] R Sosa, E Arnaud, E Memin, and G Artana. Study of the flow induced by a sliding discharge. *IEEE transactions on Dielectrics and Electrical Insulation*, 16(2), 2009.

[86] DV Roupassov, AA Nikipelov, MM Nudnova, and A Yu Starikovskii. Flow separation control by plasma actuator with nanosecond pulsed-periodic discharge. *AIAA journal*, 47(1):168–185, 2009.

[87] J Little, K Takashima, M Nishihara, I Adamovich, and M Samimy. Separation control with nanosecond-pulse-driven dielectric barrier discharge plasma actuators. *AIAA journal*, 50(2):350–365, 2012.

[88] DV Roupassov, AA Nikipelov, MM Nudnova, and A Yu Starikovskii. Flow separation control by plasma actuator with nanosecond pulse periodic discharge. In *Gas Discharges and Their Applications, 2008. GD 2008. 17th International Conference on*, pages 609–612. IEEE, 2008.

[89] H Menghu, L Jun, N Zhongguo, L Hua, Z Guangyin, and H Weizhuo. Aerodynamic performance enhancement of a flying wing using nanosecond pulsed dbd plasma actuator. *Chinese journal of Aeronautics*, 28(2), 2015.

[90] N Benard, N Zouzou, A Claverie, J Sotton, and E Moreau. Optical visualization and electrical characterization of fast-rising pulsed dielectric barrier discharge for airflow control applications. *Journal of Applied Physics*, 111(3):033303, 2012.

[91] M Samimy, I Adamovich, B Webb, J Kastner, J Hileman, S Keshav, and P Palm. Development and characterization of plasma actuators for high-speed jet control. *Experiments in Fluids*, 37(4):577–588, 2004.

[92] M Samimy, J-H Kim, J Kastner, I Adamovich, and Y Utkin. Active control of high-speed and high-reynolds-number jets using plasma actuators. *Journal of Fluid Mechanics*, 578:305–330, 2007.

[93] H Yan, D Gaitonde, and J Shang. Investigation of localized arc filament plasma actuator in supersonic boundary layer. In *45th AIAA Aerospace Sciences Meeting and Exhibit*, page 1234, 2007.

[94] N Benard, P Braud, J Jolibois, and E Moreau. Airflow reattachment along a naca 0015 airfoil by surfaces dielectric barrier discharge actuator: Time-resolved particle image velocimetry investigation. In *4th Flow Control Conference*, page 4202, 2008.

[95] R Sosa, G Artana, E Moreau, and G Touchard. Stall control at high angle of attack with plasma sheet actuators. *Experiments in fluids*, 42(1):143–167, 2007.

[96] R Sosa, E Moreau, G Touchard, and G Artana. Stall control at high angle of attack with periodically excited ehd actuators. In *35th AIAA Plasmadynamics and Lasers Conference*, page 2738, 2004.

[97] YE Akansu, F Karakaya, and A Sanlisoy. Active control of flow around naca 0015 airfoil by using dbd plasma actuator. In *EPJ Web of Conferences*, page 698, 2013.

[98] L P Melton, J Hannon, C S Yao, and J Harris. Active flow control at low reynolds numbers on a naca 0015 airfoil. In *26th AIAA Applied Aerodynamics Conference*, page 6407, 2008.

[99] F Messanelli and A Nistoro. Ottimizzazione geometrica di attuatori al plasma. Master's thesis, DAST Politecnico di Milano, 2014.

[100] M Baselli and S Peronaci. Aerodynamics of an airfoil with plasma actuators of different kinds and geometries. Master's thesis, DAST Politecnico di Milano, 2015.

[101] J Kriegseis, A Duchmann, C Tropea, and S Grundmann. On the classification of dielectric barrier discharge plasma actuators: a comprehensive performance evaluation study. *Journal of Applied Physics*, 114(5):053301, 2013.

[102] M Belan. Manuale circuito pilota per dbd, 2014.

[103] W H Rae and A Pope. *Low-speed wind tunnel testing*. John Wiley, 1984.

[104] H J Allen and W G Vincenti. *Wall interference in a two-dimensional-flow wind tunnel, with consideration of the effect of compressibility*. 1944.

[105] EC Maskell. A theory of the blockage effects on bluff bodies and stalled wings in a closed wind tunnel, rae aero, 1963.

[106] S Prothin, H Djeridi, and J Y Billard. Coherent and turbulent process analysis of the effects of a longitudinal vortex on boundary layer detachment on a naca0015 foil. *Journal of Fluids and Structures*, 47:2–20, 2014.

[107] A C Daud Filho, H Cerón-Muñoz, and F Catalano. Experimental study of the influence of vortex generators on airfoils for wind turbines. In *VI Congreso Internacional de Ingeniería Mecánica y IV de Ingeniería Mecatrónica IV Congreso Internacional de Materiales, Energía y Medio Ambiente*, 2013.

[108] E Moreau, L Léger, and G Touchard. Effect of a dc surface-corona discharge on a flat plate boundary layer for air flow velocity up to 25m/s. *Journal of electrostatics*, 64(3):215–225, 2006.

[109] R Mestiri, M M Oueslati, A Wajdi Dahmouni, R Hadaji, S B Nasrallah, and F Aloui. Dynamic behavior of printed-circuits plasma actuator based on dc electrical discharge: Application in aerodynamics. *IEEE Transactions on Plasma Science*, 42(7):1854–1860, 2014.

[110] Y S Kim and J Shin. Flow actuation by dc surface discharge plasma actuator in different discharge modes. *International Journal of Aeronautical and Space Sciences*, 16(3):339–346, 2015.

[111] J Shin and L L Raja. Cathode-sheath driven low-speed aerodynamic flow actuation using direct-current surface glow discharges. *Journal of Electrostatics*, 68(5):453–457, 2010.

Appendix A

Other wind tunnel test results

In this section we report lift and drag curves of the best waveform for each actuator as far as $\Delta C_{L_{mean}}$.

DBD

Tests at 10 m/s

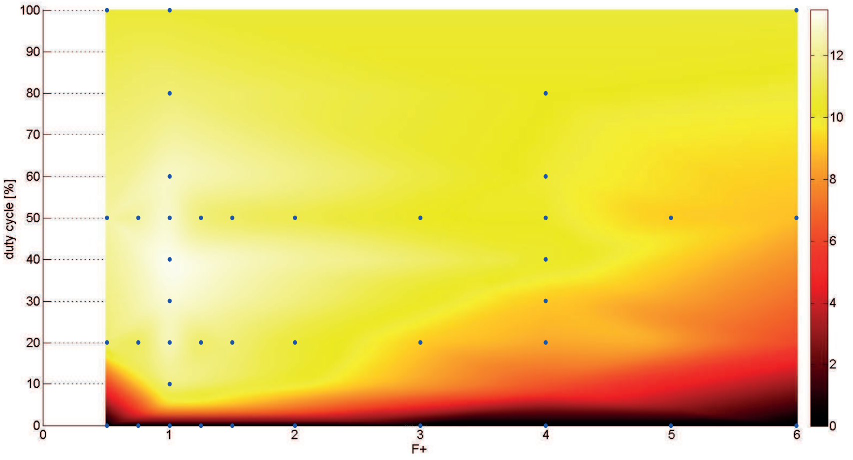

Figure A.1: $\Delta C_{L_{mean}}$ in the parameter space at $10m/s$ of actuator D3.

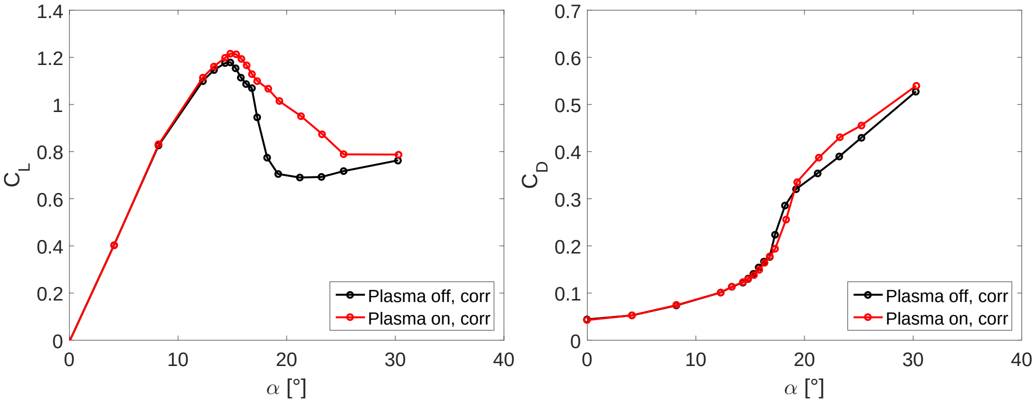

(a) **(b)**

Figure A.2: $C_L - \alpha$ (a) and $C_D - \alpha$ (b) curves at $10m/s$ of actuator D3, $f^+ = 1$, $DutyCycle = 40\%$.

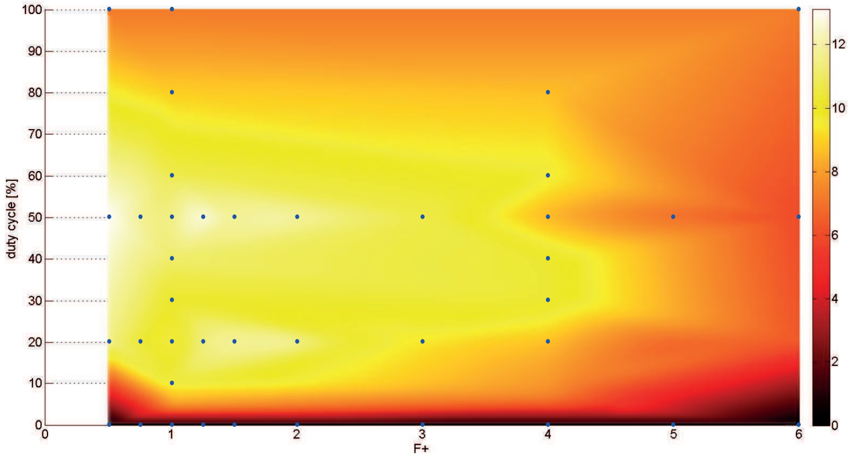

Figure A.3: $\Delta C_{L_{mean}}$ in the parameter space at $10m/s$ of actuator D5.

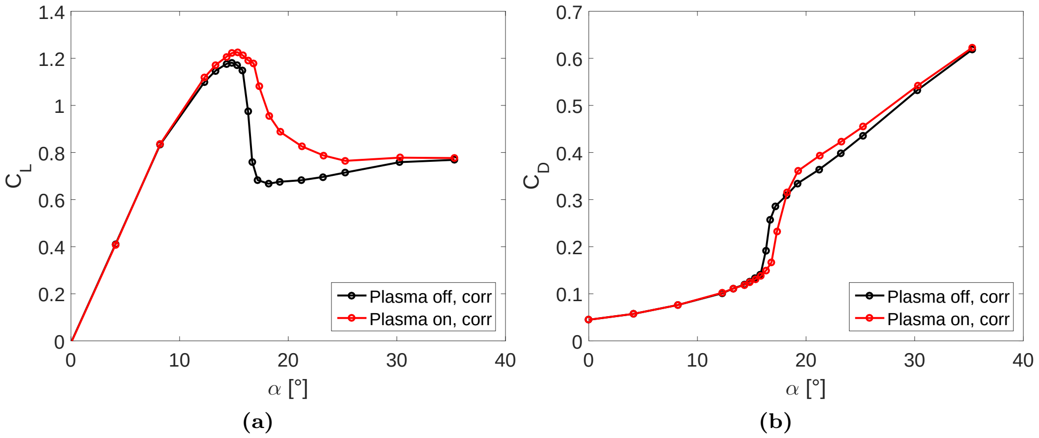

(a) **(b)**

Figure A.4: $C_L - \alpha$ (a) and $C_D - \alpha$ (b) curves at $10m/s$ of actuator D5, $f^+ = 1.25$, $DutyCycle = 50\%$.

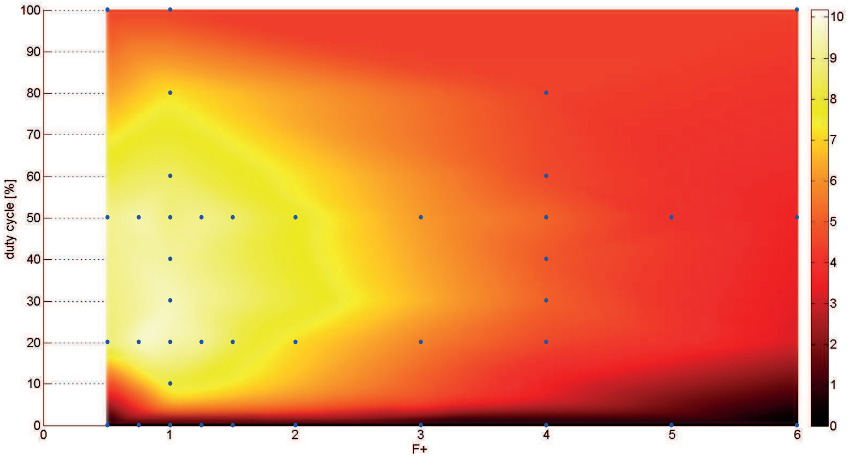

Figure A.5: $\Delta C_{L_{mean}}$ in the parameter space at $10m/s$ of actuator D7.

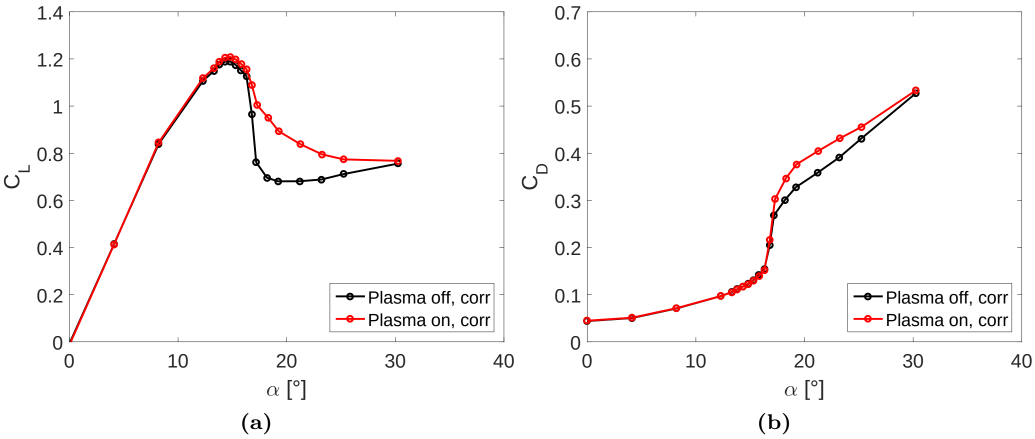

(a) **(b)**

Figure A.6: $C_L - \alpha$ (a) and $C_D - \alpha$ (b) curves at $10m/s$ of actuator D7, $f^+ = 0.75$, $DutyCycle = 20\%$.

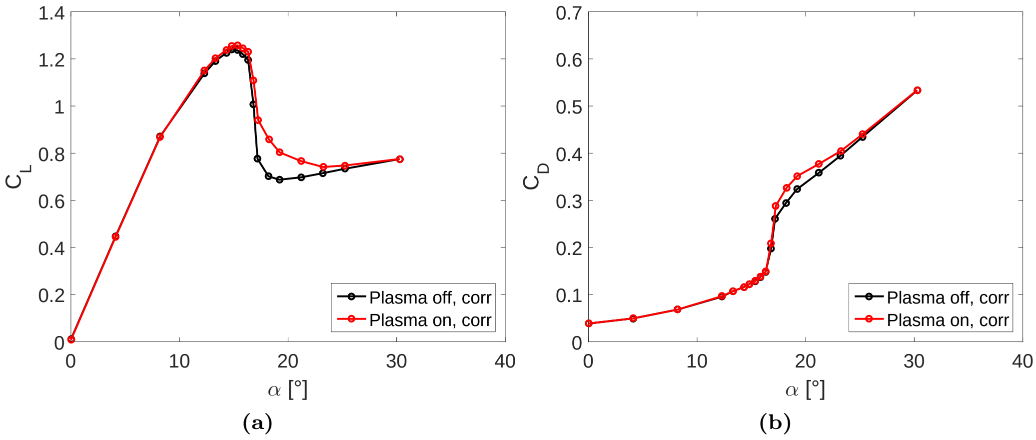

Figure A.7: $C_L - \alpha$ (a) and $C_D - \alpha$ (b) curves at $10 m/s$ of actuator D14, $f^+ = 1$, $DutyCycle = 30\%$.

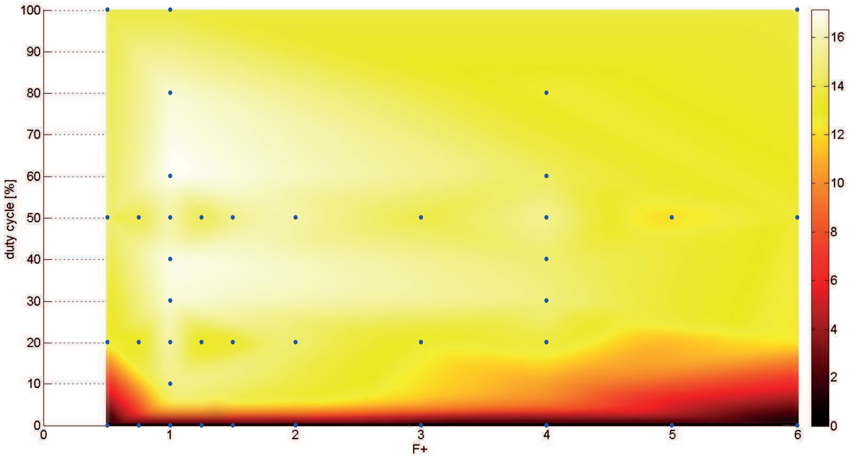

Figure A.8: $\Delta C_{L_{mean}}$ in the parameter space at $10m/s$ of actuator D15.

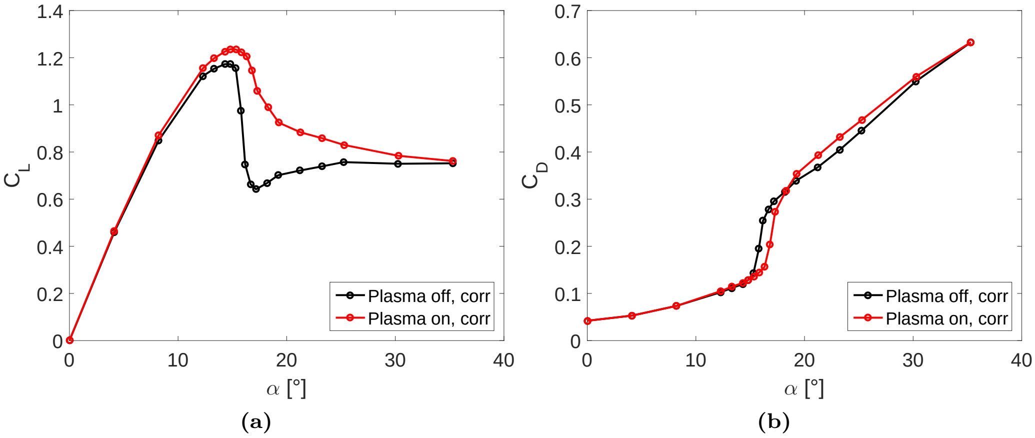

(a) **(b)**

Figure A.9: $C_L - \alpha$ (a) and $C_D - \alpha$ (b) curves at $10m/s$ of actuator D15, $f^+ = 1$, $DutyCycle = 60\%$.

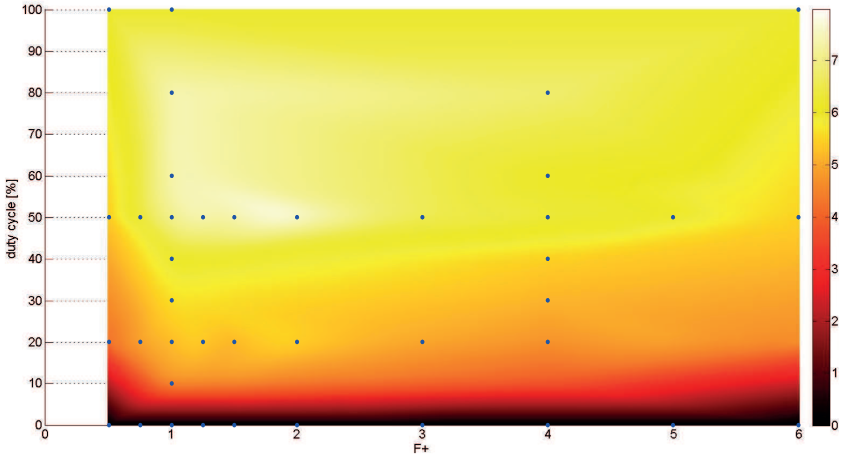

Figure A.10: $\Delta C_{L_{mean}}$ in the parameter space at $10m/s$ of actuator D16.

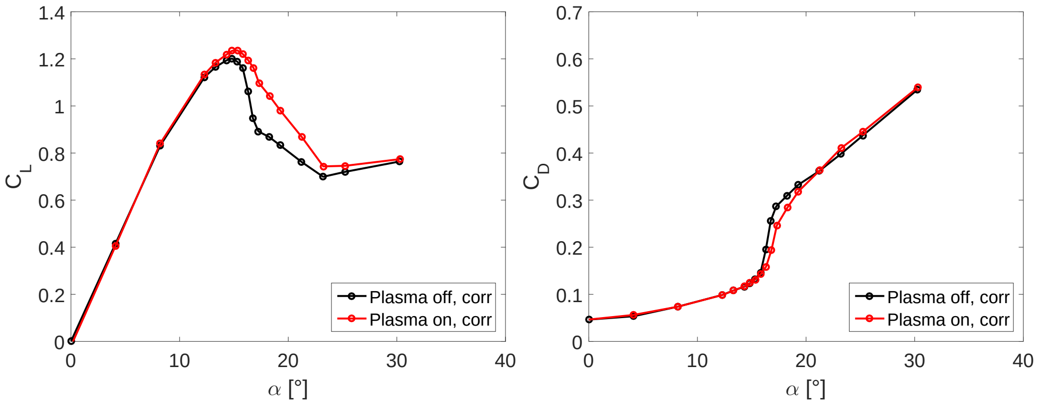

(a) **(b)**

Figure A.11: $C_L - \alpha$ (a) and $C_D - \alpha$ (b) curves at $10m/s$ of actuator D16, $f^+ = 2$, $DutyCycle = 50\%$.

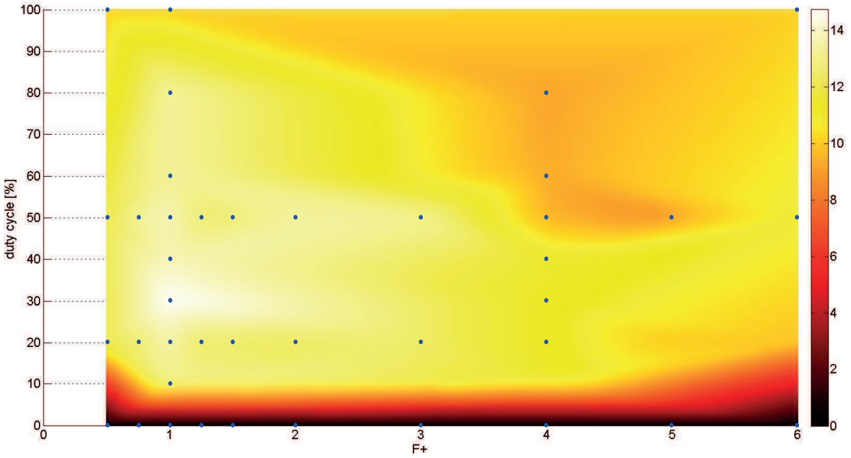

Figure A.12: $\Delta C_{L_{mean}}$ in the parameter space at $10m/s$ of actuator D17.

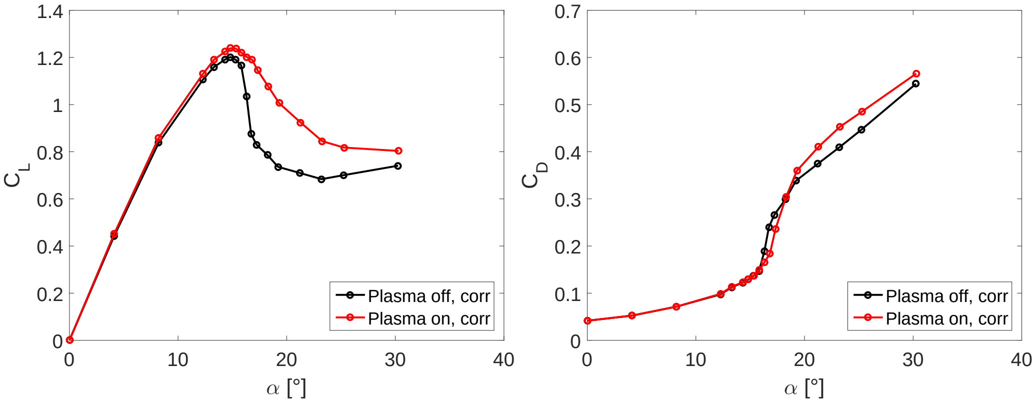

(a) **(b)**

Figure A.13: $C_L - \alpha$ (a) and $C_D - \alpha$ (b) curves at $10m/s$ of actuator D17, $f^+ = 1$, $DutyCycle = 30\%$.

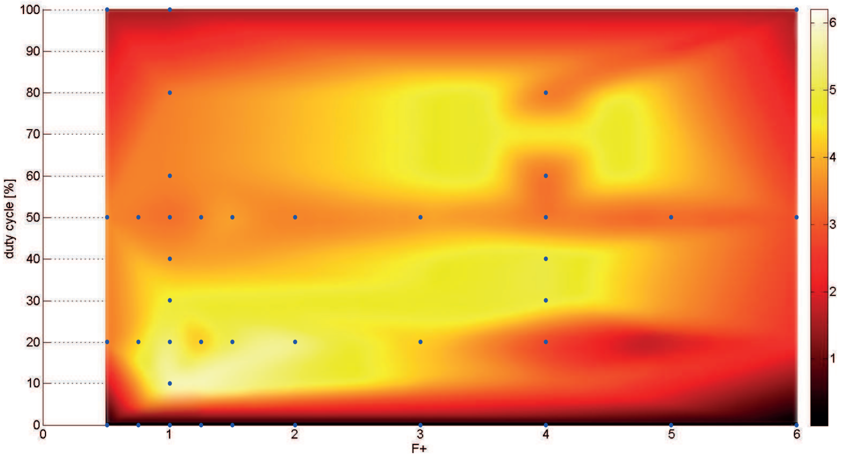

Figure A.14: $\Delta C_{L_{mean}}$ in the parameter space at $20m/s$ of actuator D1.

Tests at 20 m/s

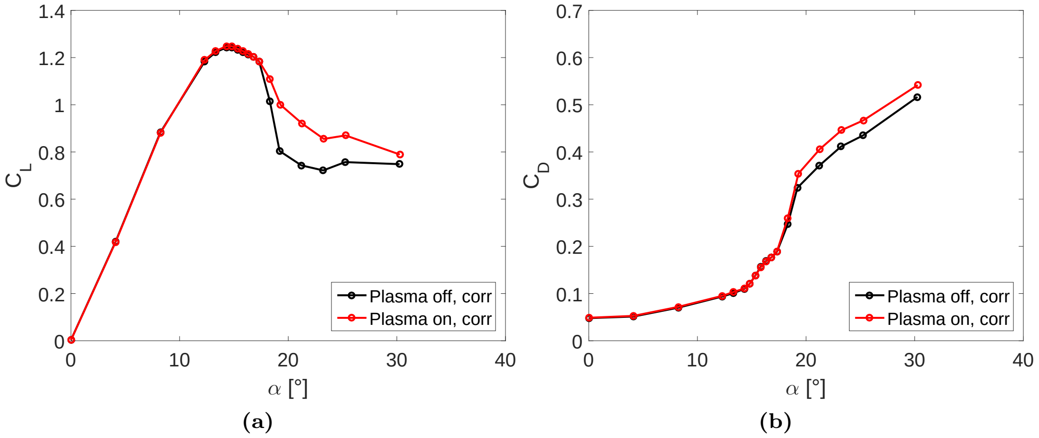

Figure A.15: $C_L - \alpha$ (a) and $C_D - \alpha$ (b) curves at $20m/s$ of actuator D1, $f^+ = 1$, $DutyCycle = 7.5\%$.

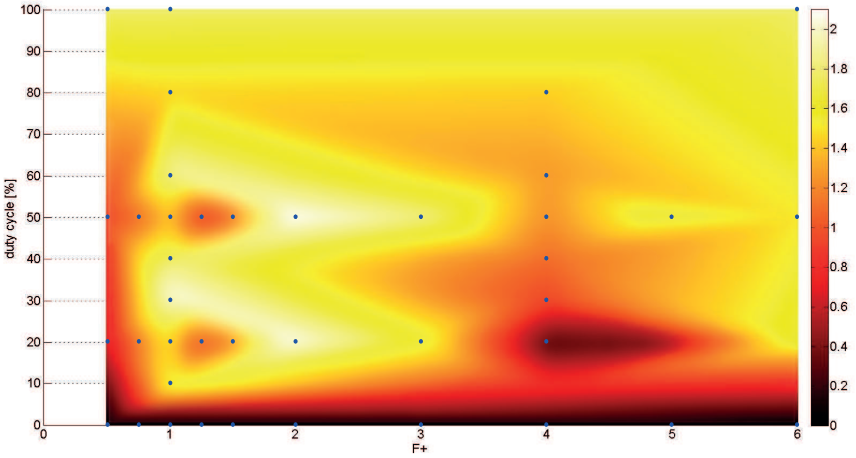

Figure A.16: $\Delta C_{L_{mean}}$ in the parameter space at $20m/s$ of actuator D3.

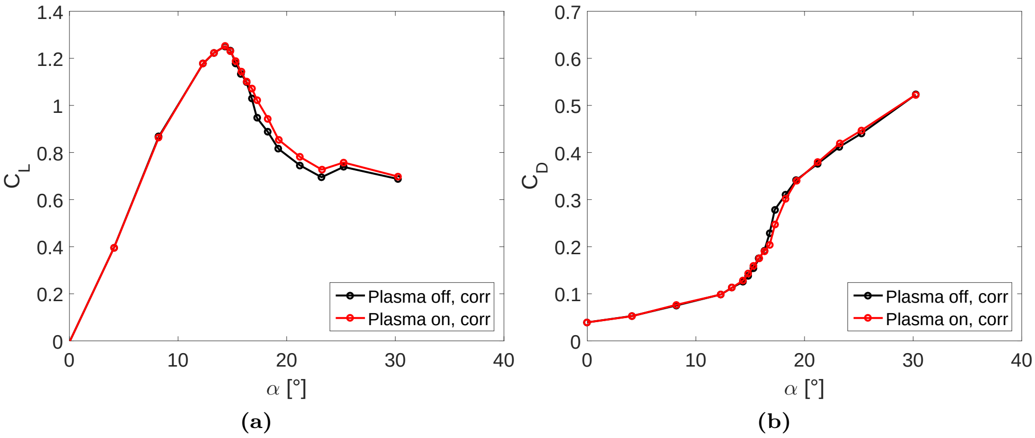

(a) **(b)**

Figure A.17: $C_L - \alpha$ (a) and $C_D - \alpha$ (b) curves at $20m/s$ of actuator D3, $f^+ = 2$, $DutyCycle = 20\%$.

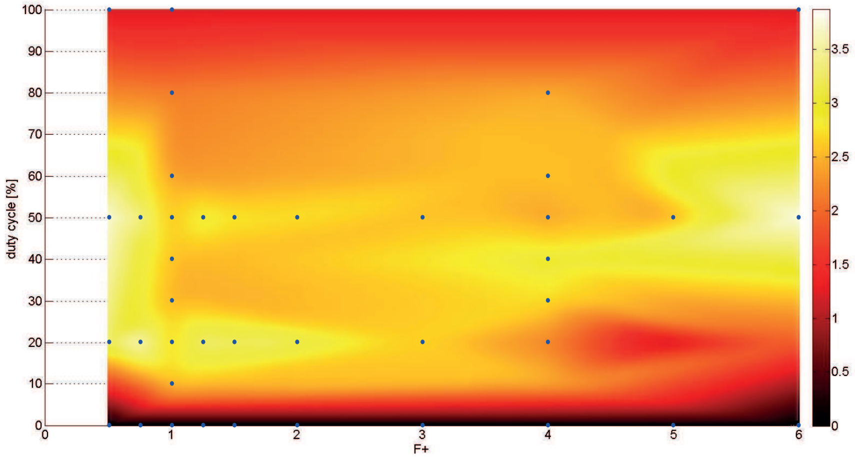

Figure A.18: $\Delta C_{L_{mean}}$ in the parameter space at $20m/s$ of actuator D5.

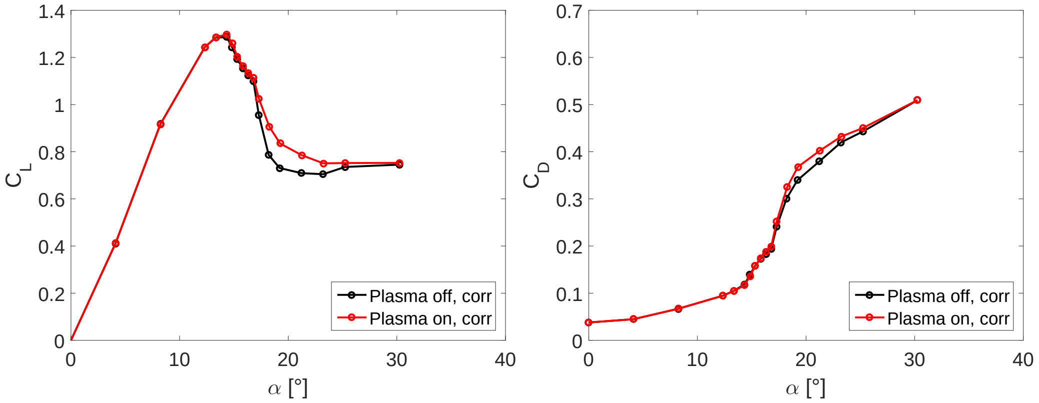

(a) **(b)**

Figure A.19: $C_L - \alpha$ (a) and $C_D - \alpha$ (b) curves at $20m/s$ of actuator D5, $f^+ = 0.75$, $DutyCycle = 20\%$.

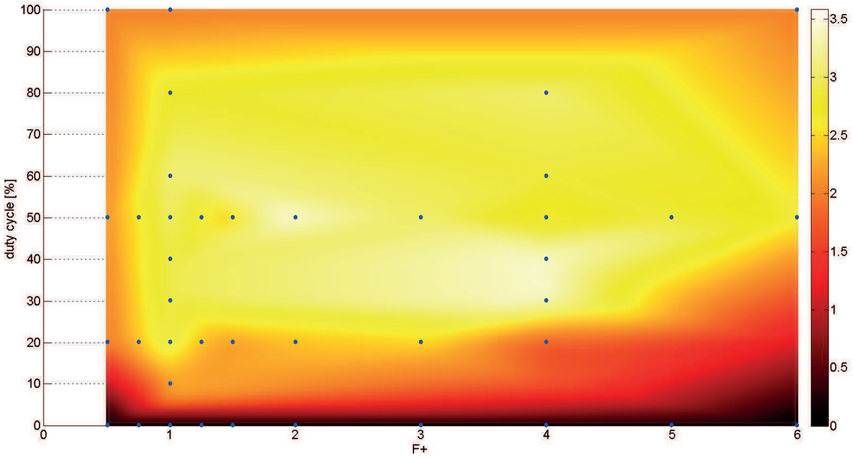

Figure A.20: $\Delta C_{L_{mean}}$ in the parameter space at $20m/s$ of actuator D7.

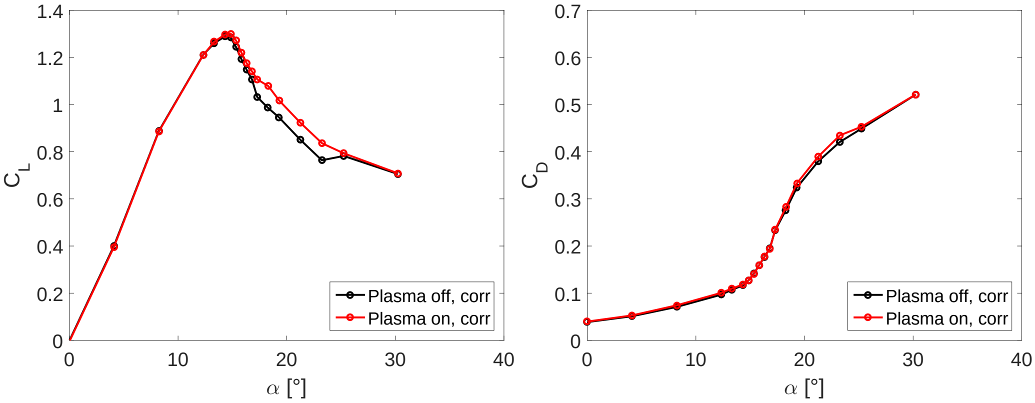

(a) **(b)**

Figure A.21: $C_L - \alpha$ (a) and $C_D - \alpha$ (b) curves at $20m/s$ of actuator D7, $f^+ = 2$, $DutyCycle = 50\%$.

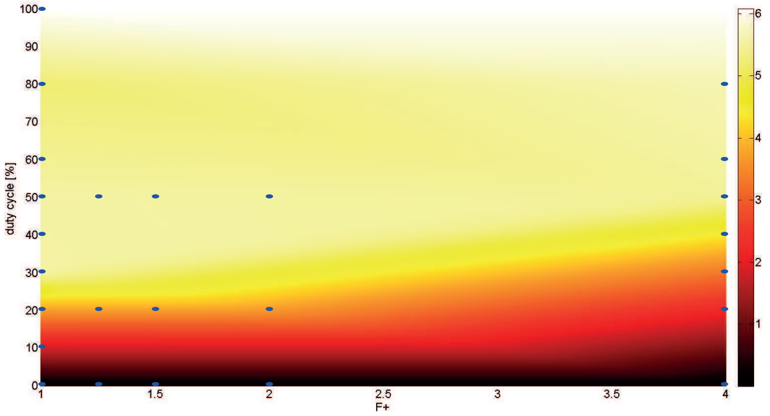

Figure A.22: $\Delta C_{L_{mean}}$ in the parameter space at $20 m/s$ of actuator D14.

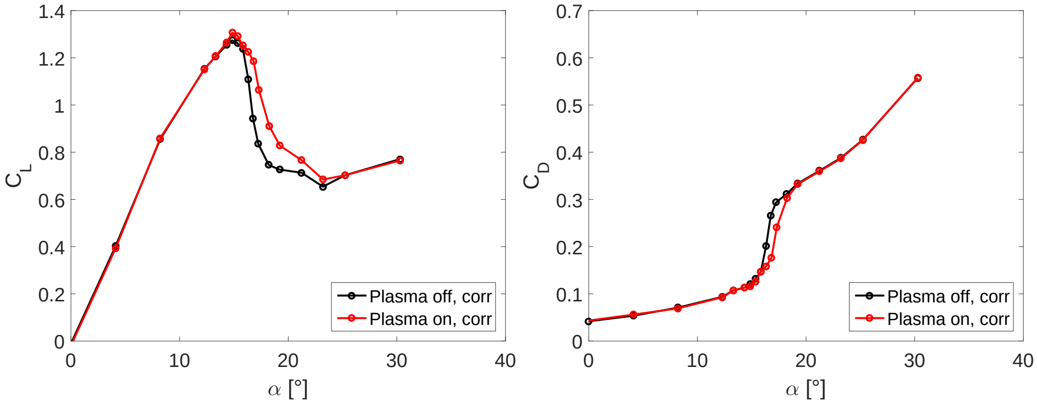

(a) **(b)**

Figure A.23: $C_L - \alpha$ (a) and $C_D - \alpha$ (b) curves at $20 m/s$ of actuator D14, $f^+ = 1$, $DutyCycle = 100\%$.

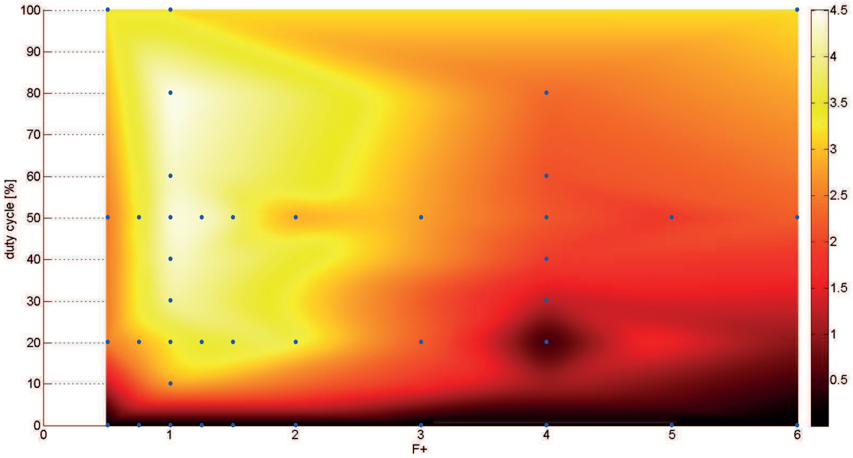

Figure A.24: $\Delta C_{L_{mean}}$ in the parameter space at $20m/s$ of actuator D16.

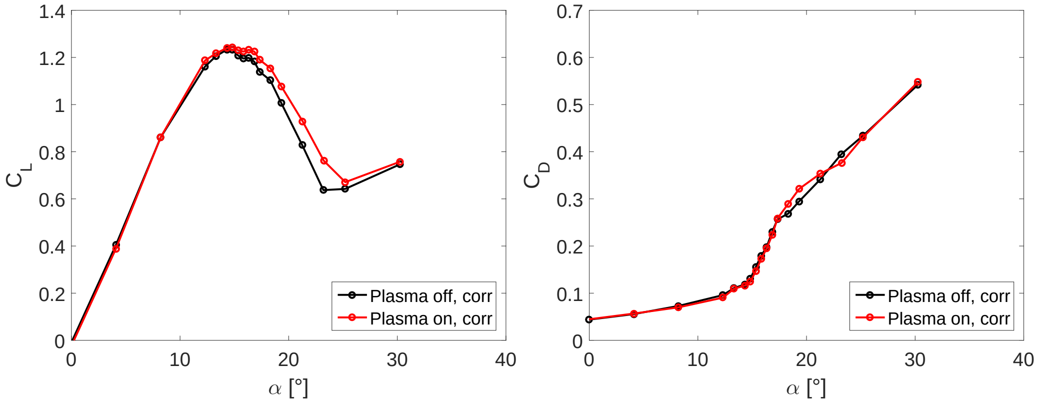

(a) **(b)**

Figure A.25: $C_L - \alpha$ (a) and $C_D - \alpha$ (b) curves at $20m/s$ of actuator D16, $f^+ = 1$, $DutyCycle = 80\%$.

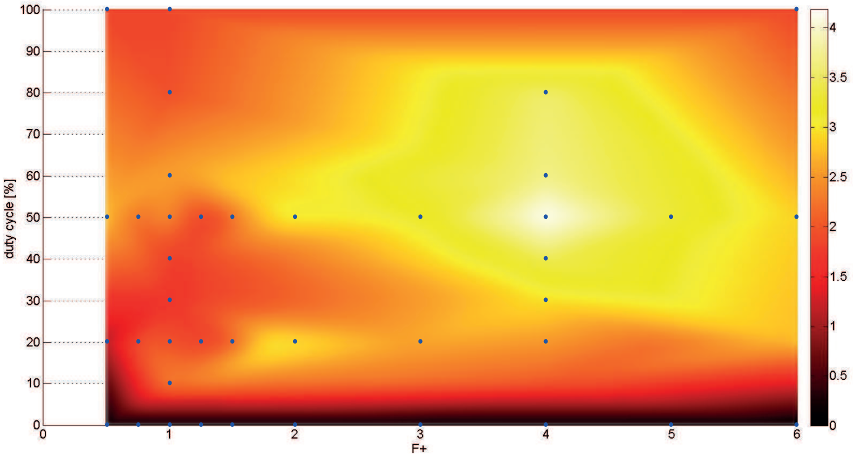

Figure A.26: $\Delta C_{L_{mean}}$ in the parameter space at $20m/s$ of actuator D17.

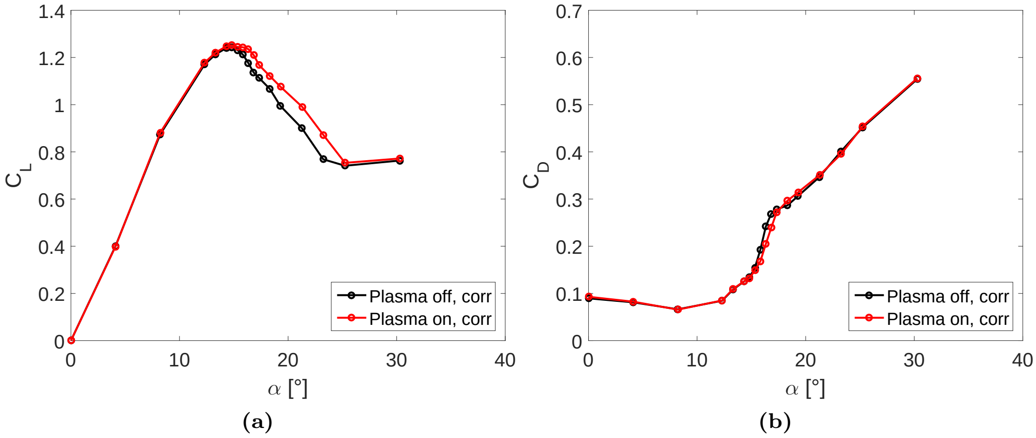

(a) **(b)**

Figure A.27: $C_L - \alpha$ (a) and $C_D - \alpha$ (b) curves at $20m/s$ of actuator D17, $f^+ = 4$, $DutyCycle = 50\%$.

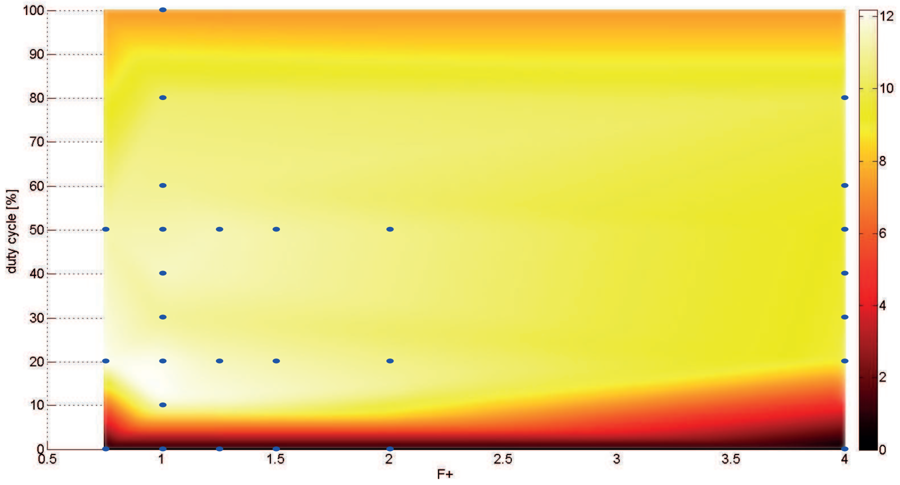

Figure A.28: $\Delta C_{L_{mean}}$ in the parameter space at $10m/s$ of actuator C1.

Corona

Tests at 10 m/s

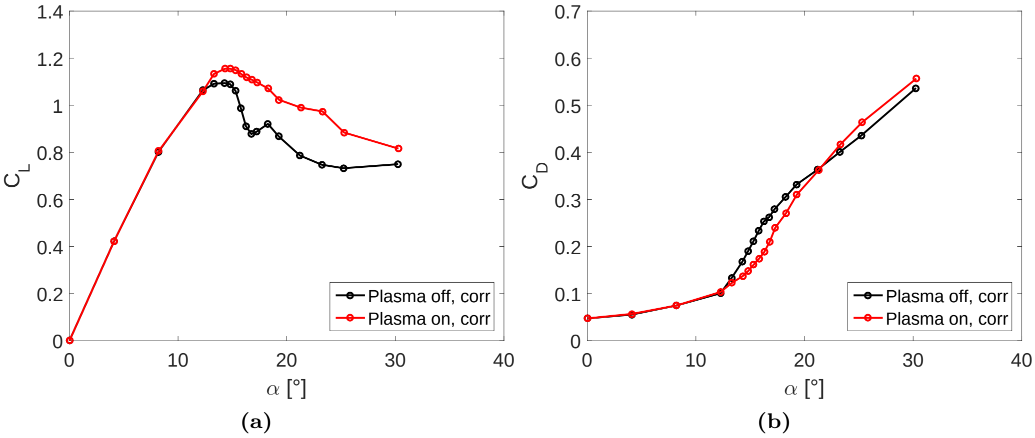

(a) **(b)**

Figure A.29: $C_L - \alpha$ (a) and $C_D - \alpha$ (b) curves at $10m/s$ of actuator C1, $f^+ = 1$, $DutyCycle = 10\%$.

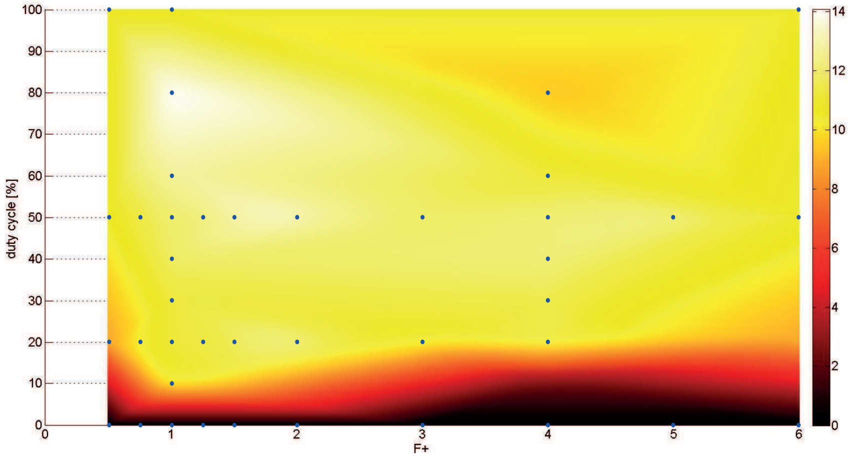

Figure A.30: $\Delta C_{L_{mean}}$ in the parameter space at $10m/s$ of actuator C13.

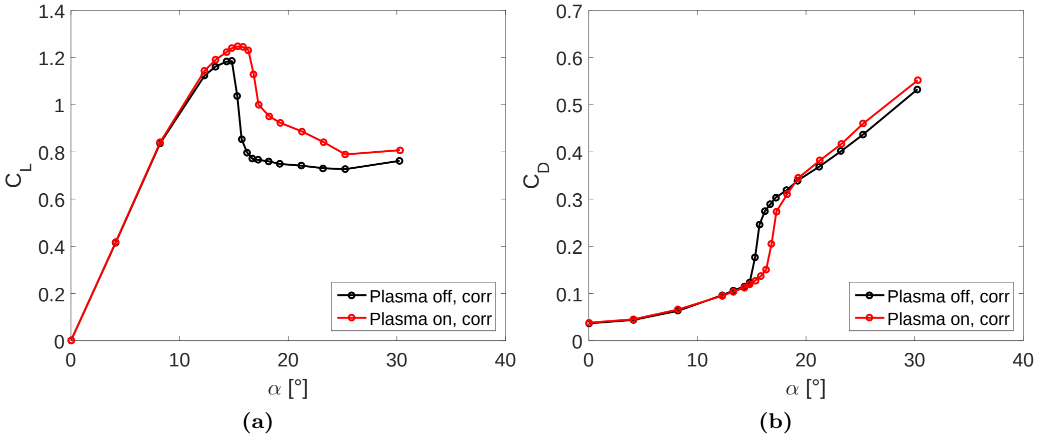

(a) **(b)**

Figure A.31: $C_L - \alpha$ (a) and $C_D - \alpha$ (b) curves at $10m/s$ of actuator C13, $f^+ = 1$, $DutyCycle = 80\%$.

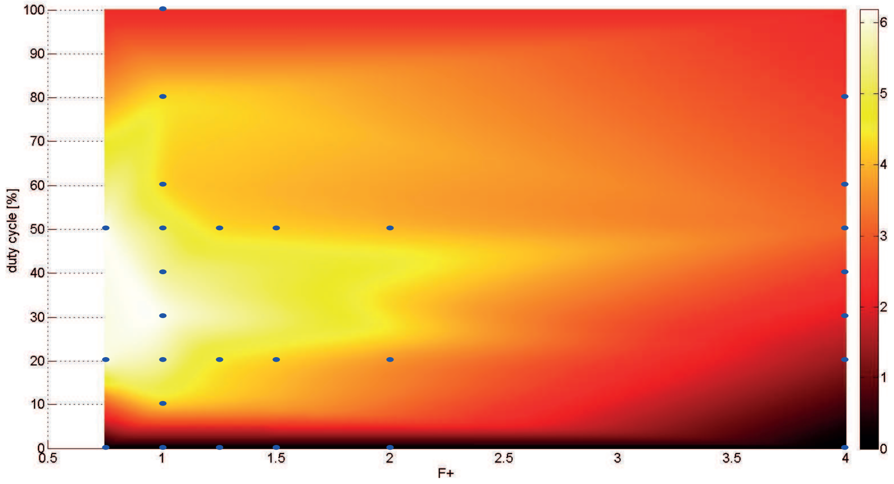

Figure A.32: $\Delta C_{L_{mean}}$ in the parameter space at $20m/s$ of actuator C1.

Tests at 20 m/s

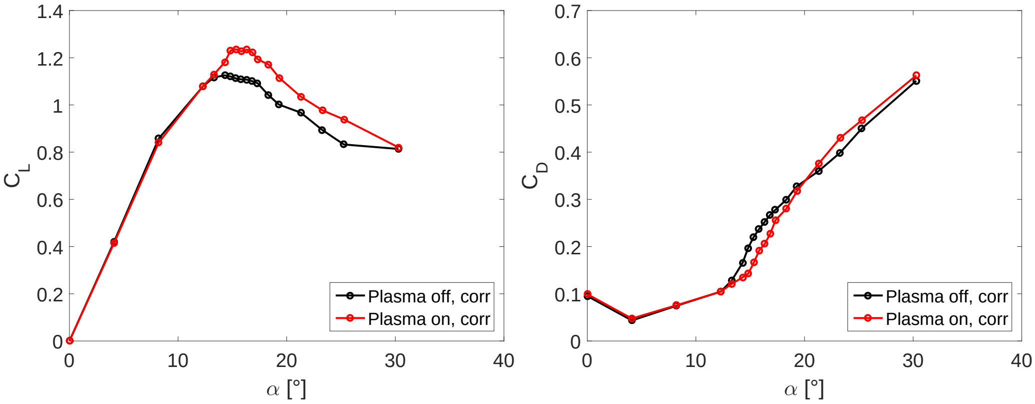

(a) **(b)**

Figure A.33: $C_L - \alpha$ (a) and $C_D - \alpha$ (b) curves at $20m/s$ of actuator C1, $f^+ = 1$, $DutyCycle = 30\%$.

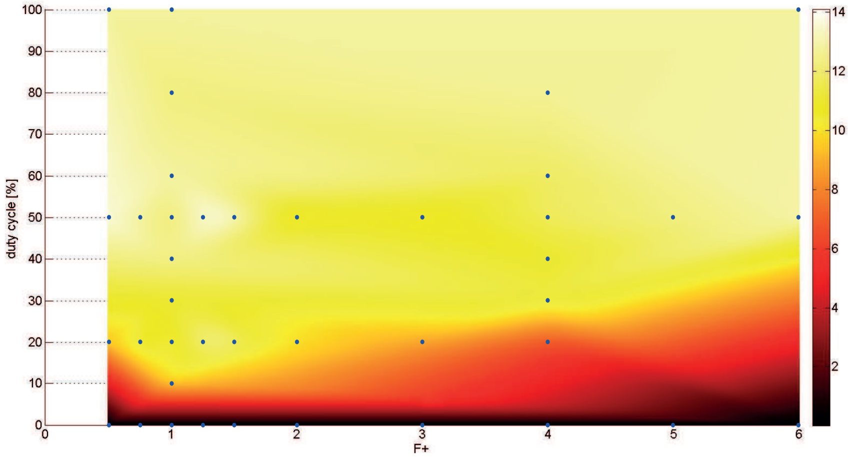

Figure A.34: $\Delta C_{L_{mean}}$ in the parameter space at $20m/s$ of actuator C13.

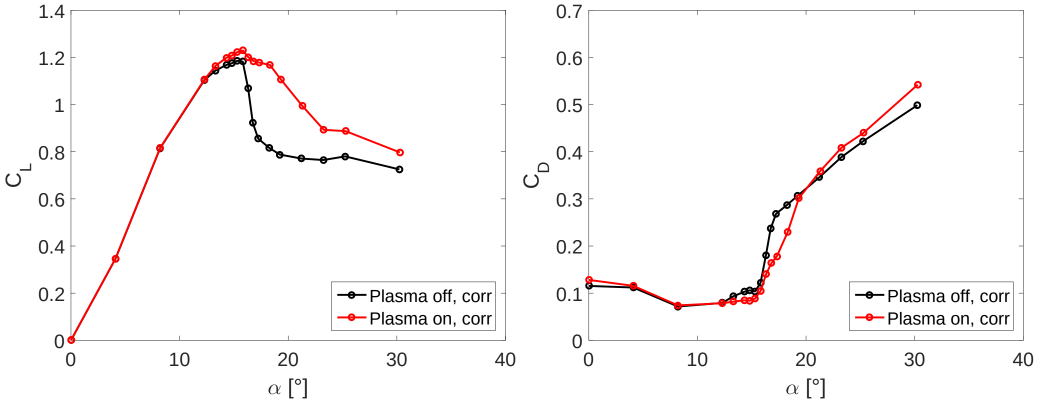

(a) **(b)**

Figure A.35: $C_L - \alpha$ (a) and $C_D - \alpha$ (b) curves at $20m/s$ of actuator C13, $f^+ = 1.5$, $DutyCycle = 50\%$.

Appendix B

Mounting and dismounting operations

In the present appendix, the procedures for removing the actuators from the airfoil and the airfoil from the test section will be shown.

B.1 Actuator removal

- Turn off the high voltage generator.
- Insert the mechanical blocks for the load cells.
- Rotate the airfoil at 90° (pitched up).
- Open the roof of the test section.
- Remove the high voltage (red) cable from the actuator.
- Unscrew the eight nylon screws of the plexiglas support.
- Carefully remove the actuator and the ground cable under the encapsulated electrode.

B.2 Airfoil removal

- If the actuator is installed, remove it following the procedure in B.1.
- Rotate the airfoil at 0° of angle of attack.
- Disconnect the high voltage plug in the airfoil socket.
- Place the Styrofoam blocks under the airfoil to sustain it after the stings are removed.
- Unscrew the eight brass nuts (four for each side) that hold the gussets on the balance.
- Unscrew the four hex socket grub screws on the airfoil (two for each side).
- On the left side of the airfoil (rotary system side), unscrew the hex socket screw in the airfoil bushing.

- On the left side of the airfoil, unscrew the hex screw and the two hex socket screws in the external bushing.
- Remove the stings by carefully pulling them out. Pliers may be helpful.
- The airfoil can now be removed from the test section, being careful about the trailing edge.

Appendix C

Machining operations

During the test campaign it has been necessary to make or repair some components of our setup. There were three main problems.

First, in order to avoid an undesired rotation of the airfoil during 20m/s tests, we built a mechanical brake acting on the rotary system. In fact, the maximum torque of the OWIS system is not sufficient to withstand the aerodynamic loads at 20m/s, especially at high angles of attack.

The second problem involved the link between airfoil and rotary system. Initially the two parts were coupled with a nylon sting. The grub screws which connected the sting to the airfoil and the OWIS system deformed the sting causing a slight rotation of the airfoil, increasing the angle of attack and tampering with the measurements at 20m/s.

The last mechanical issue concerned the fan shaft. While replacing the pulley-side bearing of the fan shaft we observed that the seat of the bearing was heavily weared out. After a brief discussion with Professor Belan about replacing the whole shaft, we decided to repair it. It follows a thorough explanation of the above operations.

C.1 Mechanical brake

The mechanical brake must prevent the rotary system from moving under excessive aerodynamic loads. The system has a knob connected to the motor shaft that can be used to move the rotor by hand. This knob has been very useful since it is where the brake applies its action. The brake is an L-shaped aluminium block with a hole the same size of the knob and a screw that clamps it in position.

The procedure to perform a 20m/s test is the following:

- With the brake in position, the balance offsets are acquired.
- Making sure that the brake is removed, the airfoil is rotated at the desired angle of attack.
- The brake is inserted and tightened by hand.
- The wind tunnel can be turned on and the measurements can be taken.
- After the data has been acquired, the wind tunnel is turned off and the brake is removed for another acquisition routine.

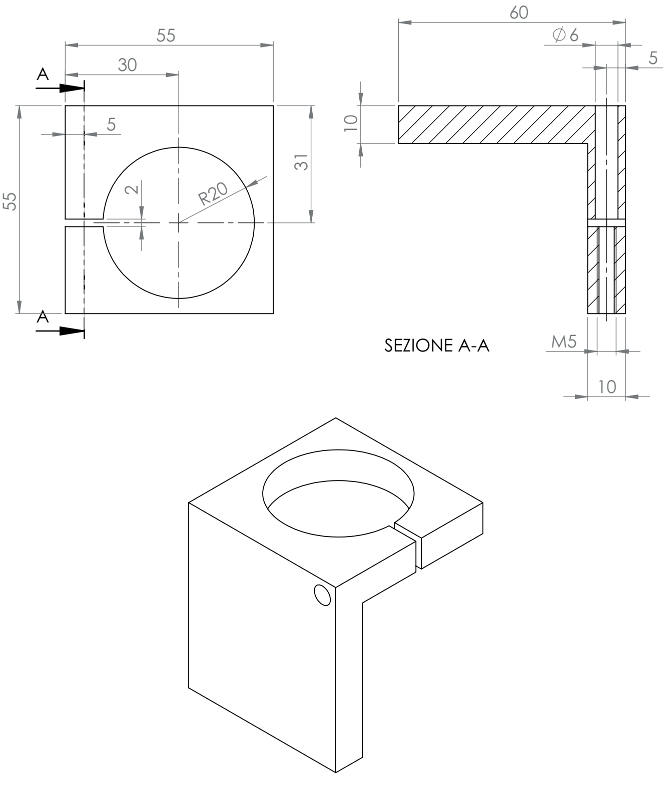

Figure C.1: CAD of the mechanical brake

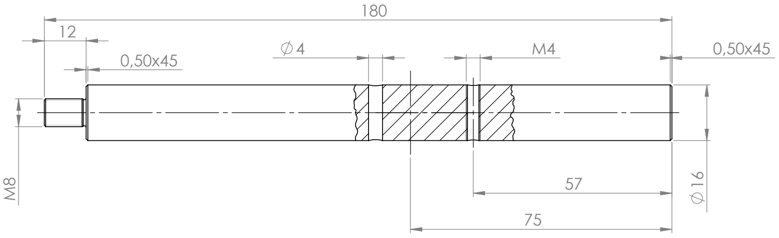

Figure C.2: Drawing of the new steel sting.

C.2 Sting

The nylon sting was replaced by a steel one, to improve torsional stiffness. The coupling between airfoil and sting, originally made by a grub screw, has been redesigned.

The old sting was held in place only by the friction of the grub screw. It was tightened on a nylon bushing on the side of the airfoil. Now a screw passes through the nylon bushing and is tightened directly into the steel sting, locking it with respect to the bushing. A CAD drawing of the sting is shown in Fig. C.2.

C.3 Shaft

The shaft was severely damaged near the bearing seat. There were several deep carvings, up to 1.5mm deep, which caused the bearing to vibrate due to shaft eccentricity. Consequently, the wind tunnel was very noisy during operation. To solve the problem we decided to machine the shaft near the pulley-side bearing seat, reducing the diameter from 30mm to 25mm. In this way all the carvings were removed. To fit the new bearing, a stainless steel bushing was machined and coupled to the shaft. The coupling between shaft and bushing is with interference and was ensured by using an epoxy resin. Fig. C.3 shows a drawing of the shaft assembly with a detail view of the repaired section.

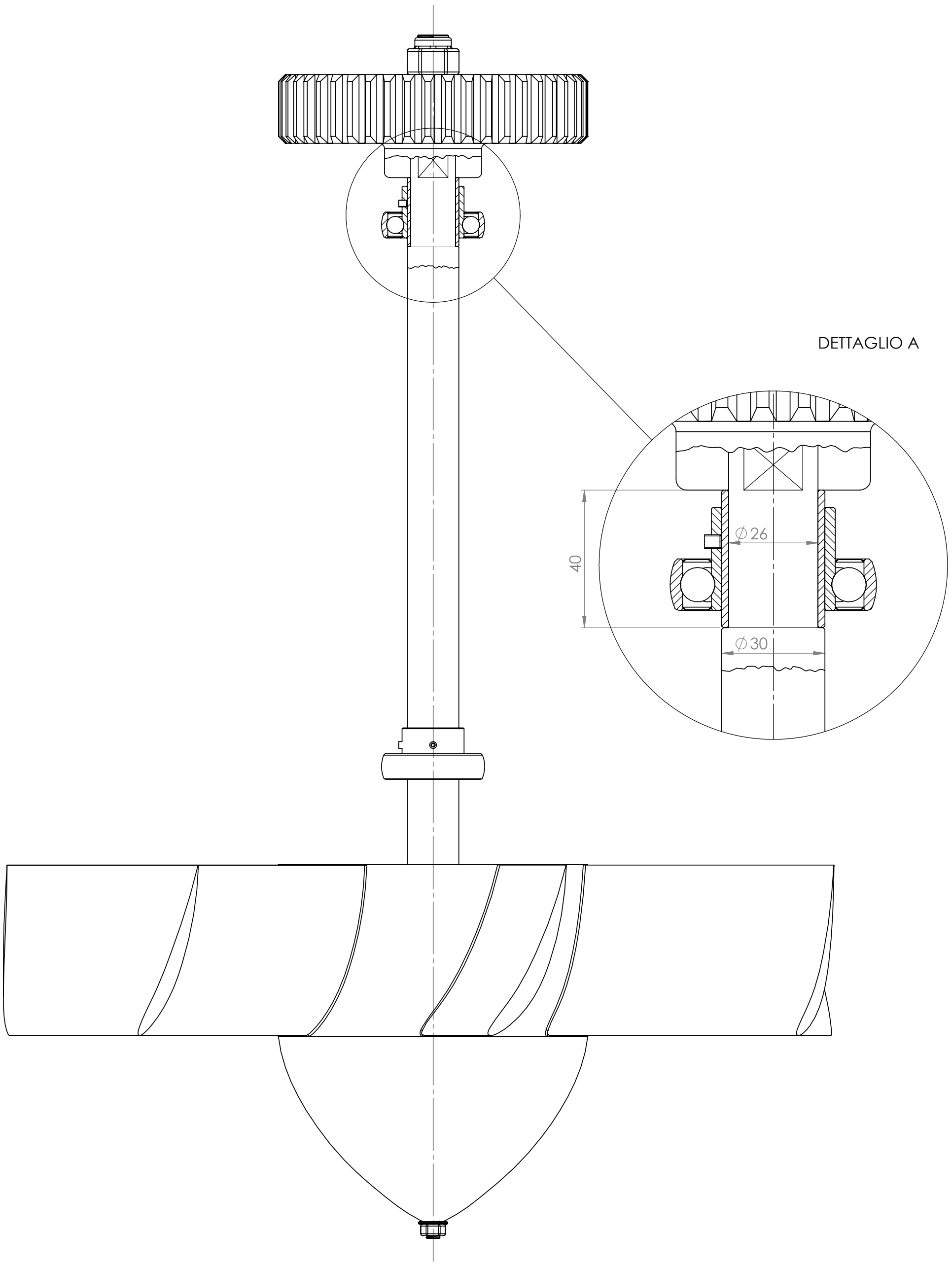

Figure C.3: Assembly of the wind tunnel fan group. Detail view of the bushing fitted on the shaft after the machining operation.